MANIPULATION AND ISOLATION OF BIOMOLECULES USING DIELECTROPHORETIC AND HYDRODYNAMIC METHODS

A Dissertation
Submitted to the Graduate Faculty
of the
North Dakota State University
of Agriculture and Applied Science

By

Myungkeun Oh

In Partial Fulfillment of the Requirements
for the Degree of
DOCTOR OF PHILOSOPHY

Major Program:
Materials and Nanotechnology

June 2021

Fargo, North Dakota

North Dakota State University
Graduate School

Title

MANIPULATION AND ISOLATION OF BIOMOLECULES USING DIELECTROPHORETIC AND HYDRODYNAMIC METHODS

By

Myungkeun Oh

The Supervisory Committee certifies that this ***disquisition*** complies with North Dakota State University's regulations and meets the accepted standards for the degree of

DOCTOR OF PHILOSOPHY

SUPERVISORY COMMITTEE:

Dr. Yongki Choi
Chair

Dr. Dharmakeerthi Nawarathna

Dr. Erik Hobbie

Dr. Sanku Mallik

Approved:

6/30/2021
Date

Dr. Erik Hobbie
Department Chair

ABSTRACT

Novel particle manipulation techniques are developed to separate, isolate, and control a wide range biomolecules from DNA to cells in complex solution such as whole blood. First, we show that integrating an insulating tip with dielectrophoresis allows us to trap, carry, reposition, and relocate nanoscale objects, which can be used as molecular tweezers without fouling, electrolysis, and joule heating issues associated with conventional dielectrophoretic methods. In addition, we find that two theoretical force calculations (Clausius-Mossotti model and counter ion fluctuation model) result in a factor of 2-40 difference, but the magnitude of both is 4 orders stronger than the thermal force, which is strong enough to manipulate objects in the medium. Second, we perform sedimentation and size-based particle separation methods in a microfluidic device configuration. Using polydimethylsiloxane and its high gas solubility, we demonstrate a sedimentation-based, blood cell separation method. To further isolate small biomarkers such as exosomes utilizing a deterministic lateral displacement principle, we fabricate nanoscale pillar structures on a silicon wafer using multiple nanolithography processes and explore possibilities for size-dependent particle separation on the device.

ACKNOWLEDGMENTS

I would like to thank to my advisor Dr. Yongki Choi for his kindly guidance and providing me an opportunity to work in his research group. I would not have been able to complete this research without his excellent support. I would also like to thank my supervisory committee, Dr. Erik Hobbie, Dr. Dharmakeerthi Nawarathna, and Dr. Sanku Mallik for their consultancy and encouragement.

I would like to express my gratitude to former and current colleagues in Dr. Choi's group, Dr. Sung Oh Woo, Lina Alhalhooly, James Froberg, Sakurako Tani, Baily Boehler, and Kyle Nietfeld. My special thanks go to Paul Omernik from NDSU physics for helping with the 3D printer, Greg Strommen from NDSU Center for Nanoscale Science and Engineering for helping with microfabrication process, Dr. Jordie Haring and Megan Ruch from the COBRE Animal Core Facility for procuring mouse blood, and Ben Bernard from the NDSU School of Design, Architecture and Art for helping with the laser cutting system.

Lastly, my deepest thanks go to my family in South Korea for their love and support. This dissertation would not be possible without them.

TABLE OF CONTENTS

LIST OF TABLES

LIST OF FIGURES

CHAPTER 1. INTRODUCTION

Recent advances of nano-bio-technology integrating nanoscale manipulation methods and molecular biology provide opportunities to overcome many problems in biological and biomedical research and applications. For example, reliable and accurate detection of rarely existing biomarkers in blood requires an extremely high, nearly single-molecule sensitivity and high clinical specificity, both of which have been a grand challenge to achieve for the early diagnosis and treatments of disease including cancer. By working with the dielectrophoresis and hydrodynamics principles, nanoscale structure and device configuration could allow to selectively manipulate target biomolecules and push the limit of detection down to single molecules. Therefore, the development of such particle manipulation technology could provide a new paradigm for the accurate detection and reliable screening of early-stage cancer and other diseases.

This thesis demonstrates the techniques of controlling and manipulating biomolecules including DNA and cells. Chapter 2 describes the dielectrophoretic (DEP) methods to trap and re-position sub-micron scale particles and DNA. First, we examine the basic concept of insulate-based DEP (iDEP) and its integration with an insulating tip to generate localized iDEP at the tip. Next, we demonstrate iDEP-based molecular tweezers for manipulating particles and DNA with nanoscale spatial resolution. Finally, we describe the direct measurements of iDEP strength and polarity using the Clausius-Mossotti factor and counter ion fluctuation models, leading towards the optimization and calibration of iDEP integrated nano-devices for the effective control and manipulation of target biomolecules. Additionally, we perform finite element simulation to further calculate and estimate the distribution of the electric field and the field gradient at the tip.

The chapter 3 describes how fluid dynamics can be used to separate particles in polydimethylsiloxane (PDMS)-based microfluidic devices. It has been demonstrated that the high gas solubility of PDMS could be used as a power-free, pumping method to drive fluid in PDMS-based microfluidic devices. However, no analytical model that describes the degassing process of air molecules through PDMS and the correlation between the flow rate and other device geometrical parameters has yet been developed. In this chapter, we discuss a simple diffusion model for a PDMS pumping device and validate the model with experimental data sets acquired from various devices. More importantly, we provide the quantitative relationship between fluid kinetic parameters and the device's geometrical parameters using the model and experiments. Thus, one can easily predict and manipulate the flow dynamics by adjusting two geometrical parameters of the device, which is not possible with previous empirical approaches. We also demonstrate potential applications of our approach: self-powered, sedimentation-based, on-chip plasma separation and a power-free pumping method for non-PDMS microfluidic devices using a removable vacuum battery. Our results enable other researchers to design and fabricate reproducible, reliable and power-free PDMS and non-PDMS microfluidic devices, which could help further the development of droplet-based microfluidic testing applications.

The chapter 4 demonstrates particle separation techniques utilizing a deterministic lateral displacement (DLD) principle and provides a practical guidance for the fabrication of such a DLD device using nanolithography processes. Initially, we discuss the basic fluid dynamics in the microfluidic channel and size-dependent particle flow in the channel (consisting of repeated obstacles). Next, we focus on the nano and micro fabrication processes of silicon-based devices, discussing all necessary materials and techniques for reproducible and reliable fabrication of high-quality nano structures on silicon wafers. Then, we show our preliminary particle

separation results obtained from the initial DLD prototype devices, demonstrating their promise as a tool for isolating exosomes from plasma and whole blood. This chapter concludes with a brief discussion of future work to accomplish complete exosome separation from a drop of whole blood by combining an on-chip, self-powered diffusion method and the DLD fabrication, structure, and design.

CHAPTER 2. A TRAP AND PLACE BIOMOLECULES USING DIELECTROPHORESIS (DEP)[1]

Introduction

Dielectrophoresis

Manipulation and isolation of target biomolecules in a complex medium have gained special attention due to their central role in disease screening and diagnostics [1]–[3]. Among many biomolecule manipulation methods, among them, force-based dielectrophoresis (DEP) has been widely used to trap, separate, and manipulate a variety of nanoscale objects including proteins and cells suspended in the medium, based on either their size or polarizability [4]–[7].

If a neutral particle is present in a uniform electric field, the particle does not move since the forces acting on the particle surface are the same (Figure 1A). However, if the neutral particle present in a non-uniform electric field, the particle would move either high dense of electric field (pDEP) or less dense of electric field (nDEP) (Figure 1B) [8], [9].

[1] The material in this chapter was co-authored by Myungkeun Oh, Vidura Jayasooriya, Sung Oh Woo, Dharmakeerthi Nawarathna, and Yongki Choi. The content in this chapter was reproduced with permission from ACS Appl. Nano Mater. 2020, 3,1, 797 - 805 Copyright 2020 American Chemical Society. Myungkeun Oh and Vidura Jayasooriya worked together and had primary responsibility to perform experiment. Myungkeun Oh and Vidura Jayasooriya collected and analyzed experimental data.

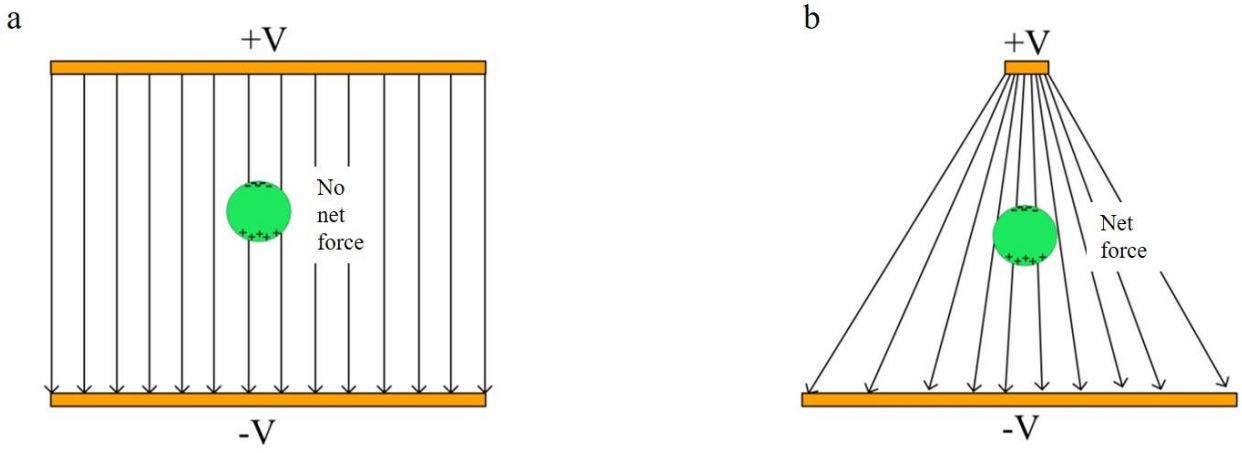

Figure 1. (a) Neutral particle present in uniform electric field. (b) Neutral particle present in non-uniform electric field. Dielectrophoresis (DEP).

Generally, traditional DEP techniques utilize the geometry of metal electrodes to create non-uniform electric fields (Figure 2). The electrokinetic-driven, selective trapping and separating of target objects from the medium to the electrodes have been demonstrated previously using DNA [10], [11], cancer cells [1], [5], and bacteria [12], [13] along with microfluidic configurations.

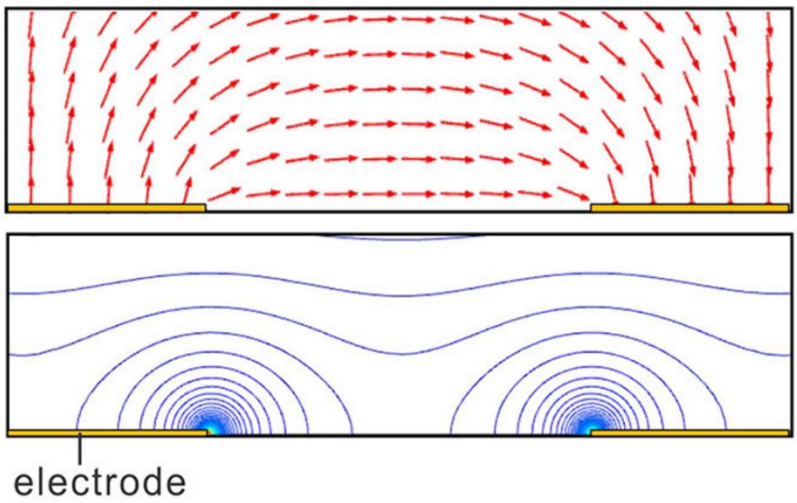

Figure 2. Electric field lines (red arrow) and contour plot of the field created by the metal electrodes.

Insulator-Base Dielectrophoresis

On the other hand, insulator-based DEP (iDEP) or electrodeless DEP techniques have been developed to trap target objects with insulating obstacles rather than metal electrodes [7], [14], [15], eliminating potential fouling, electrolysis, and joule heating issues caused by the applied high electric field at the metal electrodes of the traditional DEP method. In these devices, a constriction or channel in an insulating material deforms the electric field in a conducting solution, creating a high electric field gradient with a local maximum (Figure 3). Thus, the insulating obstacles can trap target objects including DNA and cells [7], [16]. Moreover, iDEP provides a non-uniform electric field over the entire depth of the channel, increasing the effective trapping area without the issues [7], [15]. The advantage of iDEP is that it can be easily fabricated and integrated with microfluidic systems in order to improve detection efficiency and enhance biomolecule mixing, separation, and concentration, which is not possible with other manipulation techniques such as optical and magnetic trapping [11], [17].

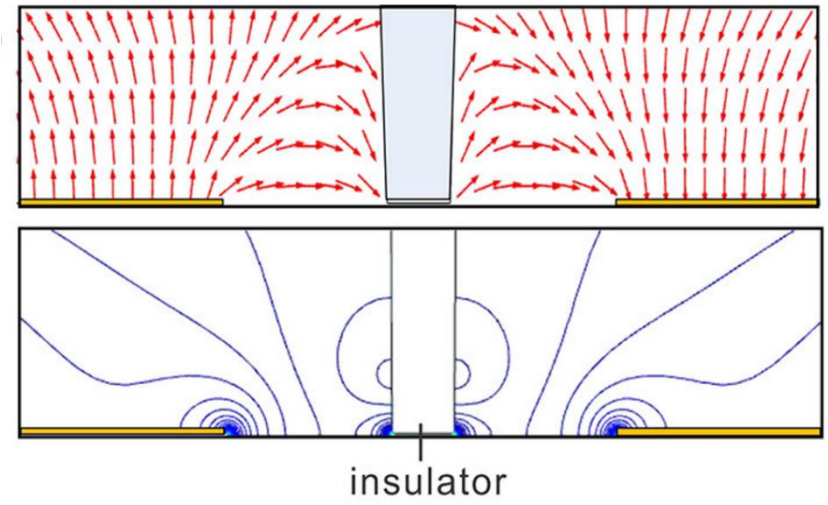

Figure 3. Deformation of the field by the insulating obstacle in the center generates the additional iDEP trap.

Although several DNA manipulation techniques have been improved and used to measure DNA unzipping [18], hybridization [4], and digestion of DNA by λ-exonuclease [19], no effective methods have been developed for spatial control of DNA. For instance, fixed-position-based approaches such as atomic force microscope (AFM), micropipette, and optical tweezers, and fixed-force-based approach such as a magnetic trap allow limited control of DNA, since DNA ends are fixed at the beads, AFM and micropipette cantilevers, and glass surfaces [20], [21]. Furthermore, those techniques suffer from the high force noise and drift associated with high bandwidth of the cantilevers and bead size [21], [22]. Thus, three-dimensional control of DNA using conventional manipulation techniques including DEP and iDEP methods is not feasible.

For the spatial manipulation capabilities such as picking up, repositioning, and releasing, several nanoscale metallic tip-based DEP methods have been introduced. For example, conductive AFM probe tips [23]–[26] and nanoscale pipette tips coated with metal [10], [27], [28] have been used to create the non-uniform electric field and field gradient at the end of the tip, demonstrating as an alternative technique for manipulating biomolecules and biopolymers. However, the metallic tip-based DEP methods in which a working principle is the same as the traditional DEP suffer from the drawbacks associated with unavoidable and electrochemical reactions at the metal DEP electrodes [14].

To overcome this limitation, we demonstrate insulator-based, electrodeless, mobile DEP tweezers that provide spatial control and manipulation of biomolecules without the issues of fouling and electrolysis. In this work, we used non-metal, unbiased tips that squeeze the electric field in the medium and create a strong, localized field and its gradients at the end of the tip. Thus, the tip acts like iDEP tweezers capable of three-dimensional trapping, placing, and

releasing biomolecules such as DNA. Furthermore, this technique eliminates the complex fabrication of DEP devices such as coaxial or triaxial nanoscale tips, and the requirements of specialized operating instruments like AFM.

DEP Calculation

Spherical Particle

The complex CM factor is given by $K(\omega) = \frac{\varepsilon_p^* - \varepsilon_m^*}{3[A(\varepsilon_p^* - \varepsilon_m^*) + \varepsilon_m^*]}$, where $\varepsilon_p{}^*$ and $\varepsilon_m{}^*$ are the complex dielectric constant of the particle and medium associated with conductivity σ (i.e., $\varepsilon^* = \varepsilon - i\sigma/\omega$), and A is the depolarization factor ($0 \le A \le 1$), respectively. For the spherical particle case (A = 1/3), the real part of the CM factor is expressed as $\mathrm{Re}[K(\omega)] = \frac{\omega^2(\varepsilon_p - \varepsilon_m)(\varepsilon_p + 2\varepsilon_m) + (\sigma_p - \sigma_m)(\sigma_p + 2\sigma_m)}{\omega^2(\varepsilon_p + 2\varepsilon_m)^2 + (\sigma_p + 2\sigma_m)^2}$. The CM factor can be a positive or negative value depending on the AC field frequency, determining the DEP direction and strength as shown in Figure 4. DEP can be calculated by $F_{DEP} = \pi R^3 \varepsilon_m \mathrm{Re}[K(\omega)] \nabla E^2$, where R (= 250 nm) is the radius of the particle and of ∇E^2 (= 1.30×10^{20} V^2/m^3) is the strength of the field gradient. Thus, the strength of F_{DEP} at f = 20 KHz and f = 2 MHz is estimated to be 2.2 nN and -1.6 nN, respectively.

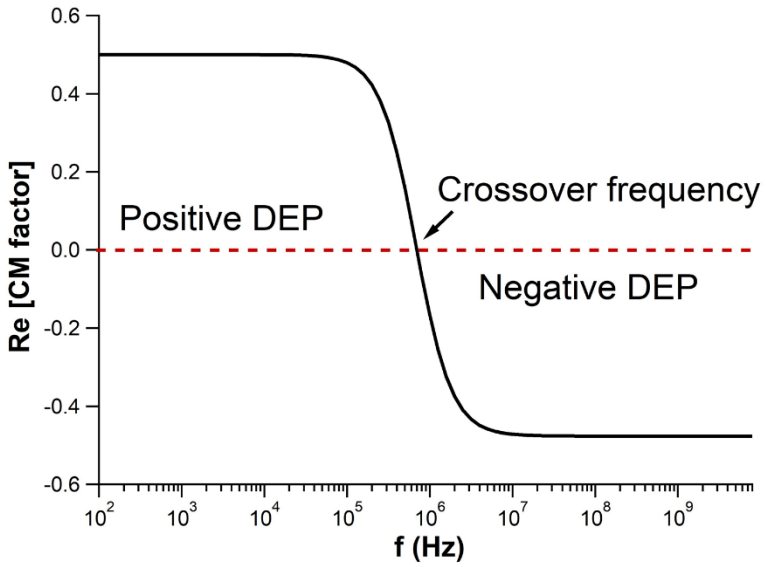

Figure 4. Real part of the CM factor of the spherical particle. In calculating this plot, the following parameters were used: $\varepsilon_p = 2.5\varepsilon_o$, $\varepsilon_m = 78\varepsilon_o$, $\sigma_p = 4 \times 10^{-3}$ S/m, $\sigma_m = 1 \times 10^{-3}$ S/m.

Ellipsoidal Particle

For the prolate spheroids (a = b < c), the real part of CM factor is expressed as $Re[K(\omega)] = \frac{3\omega^2(\varepsilon_p-\varepsilon_m)(A\varepsilon_p-A\varepsilon_m+\varepsilon_m)+3(\sigma_p-\sigma_m)(A\sigma_p-A\sigma_m+\sigma_m)}{9\omega^2(A\varepsilon_p-A\varepsilon_m+\varepsilon_m)^2+9(A\sigma_p-A\sigma_m+\sigma_m)^2}$, where A (parallel to the electric field) has an analytical solution of $A = \frac{1-e^2}{2e^3}\left[\log\left(\frac{1+e}{1-e}\right) - 2e\right]$ with the eccentricity of the spheroid $e = \sqrt{1-b^2/c^2}$. By assuming the minor axis a = b = 2 nm and major axis c = 22,000 nm[29], [30], the depolarizing factor A of DNA can be calculated to be 2.13×10^{-4}. Determined CM factor is shown in Figure 5. DEP of the prolate spheroids is given by $F_{DEP} = 2\pi abc\varepsilon_m Re[K(\omega)]\nabla E^2$, where of ∇E^2 is 2.54×10^{20} V^2/m^3. Thus, the strength of F_{DEP} is calculated to be 41.5 nN (f = 50 kHz), 18.3 nN (f = 200 kHz), and -16.5 pN (f = 10 MHz).

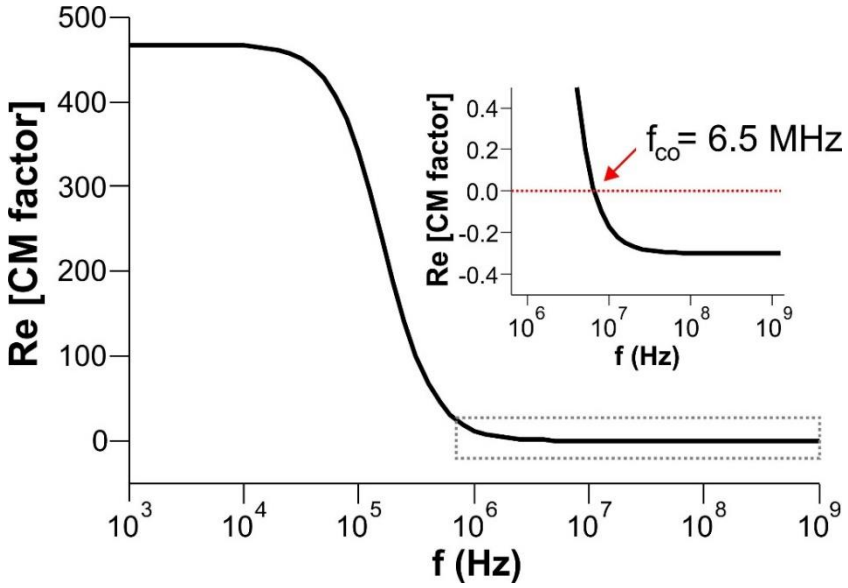

Figure 5. Asymmetric, frequency dependent real part of the CM factor assuming DNA as an ellipsoidal particle. The inset shows the negative values of the CM factor at f > f_{co}, which lead to negative DEP. In calculating this plot, the following parameters were used: a = b = 2 nm, c = 22 μm, $\varepsilon_p = 8\varepsilon_o$, $\varepsilon_m = 78\varepsilon_o$, σ_p = 1 S/m, $\sigma_m = 5\times10^{-4}$ S/m.

Counter Ion Fluctuation (CIF) Model for Ellipsoidal Particle

In this model, the counterions can move freely along the macromolecular "subunit lengths" under the influence of an external electric field [10], [31]. Total polarizability is given by $\alpha_{CIF} = \frac{z^2 q^2 {L_s}^2 n_{cc} A_{st}}{12 k_B T} \frac{l_{DNA}}{L_S}$, where z, q, L_s, n_{cc}, A_{st}, l_{DNA}, k_B, and T are the valence of counterion, the electric charge, the subunit length of DNA, the number of condensed counterions, the stability factor of the ionic phase including mutual repulsion between fixed charges on the backbone and the effect of Debye screening, the contour length of DNA, the Boltzmann constant, and the temperature, respectively. A_{st} is given by $A_{st} = \frac{1}{1-2(z\xi-1)\ln(K_s b)}$, where ξ, K_s, and b are charged density parameter $\xi = \frac{q^2}{4\pi\varepsilon_m k_B T b}$, reciprocal of the Debye screening length $K_s = \sqrt{\frac{N_{AV} q^2}{\varepsilon_m K_B T}\left(C_i z^2 + \frac{C_p}{\xi}\right)}$, and the average distance between charged sites for the DNA double helix (b = 0.173 nm). Also, $C_i = \frac{\sigma_m}{q\mu N_{AV}}$ and $C_p = \frac{2C_{DNA}}{MW_{bp}10^{-3}}$ are the

concentration of ions surrounding DNA and concentration of the phosphate group. Using $q = 1.6 \times 10^{-19}$ C, T = 298 K, $\varepsilon_m = 78\varepsilon_0$, $N_{AV} = 6.02 \times 10^{23}$ (Avogadro number), z = 1, $\sigma_m = 5 \times 10^{-4}$ S/m, $\mu = 8 \times 10^{-8}$ $m^2V^{-1}s^{-1}$ (ion mobility), C_{DNA} = 0.12 μg/μl (DNA concentration), MW_{bp} = 649 Da/bp (molecular weight per base pair), A_{st} is estimated to be $A_{st} = 0.029$. The subunit length L_s is given by $L_s = \sqrt{\frac{9\Delta\varepsilon}{\pi\varepsilon_m(z\xi-1)A_{st}N_{AV}C_pb}}$, where Δε is the dielectric increment. With Δε = 1 ~ 10 experimentally determined with various DNA [32], [33], L_s is estimated to be 1.02×10^{-7} ~ 3.23×10^{-7} m. Using the number of condensed counter ions $n_{cc} = \frac{\emptyset_c L_s}{z \cdot b}$ and a fraction of condensed counter ions $\emptyset_c = 1 - \frac{1}{z\xi}$, αCIF is estimated to be 1.51×10^{-29} ~ 1.51×10^{-28} Fm^2. For the 48,500 bp DNA, the total polarizability divided by the DNA base pairs α_{CIF}/bp lies between 3.12×10^{-34} ~ 3.12×10^{-33} Fm^2/bp. Finally, the strength of $F_{DEP} = ¼\alpha_{CIF}\nabla E^2$ is estimated to be 0.962 ~ 9.62 nN.

Thermal Fluctuation of DNA Using the Worm-Like Chain Model

The thermal force is given by $F_{th} = k_BT/2R_H$, where k_B, T, and R_H are Boltzmann constant, temperature, and a hydrodynamic radius of DNA. In the worm-like chain model[34], the radius of gyration R_g of DNA is given by $R_g = \sqrt{\frac{1}{3}PL}$, where P (= 50 nm) is persistence length of DNA and L (= 22,000 nm) is the contour length of YOYO-1 labeled DNA. R_g is estimated to be 606 nm. Using the relationship of $R_H = R_g/1.54$, the R_H is estimated to be 393 nm. Finally, F_{th} is calculated to be 5.23 fN. By equating F_{th} with F_{DEP}, the strength of the field gradient $\nabla E^2 = 4F_{th}/\alpha$ is calculated to be 3.20×10^{13} ~ 8.08×10^{16} V^2/m^3 with the lower and upper limit of estimated α values from both the CM factor and CIF models.

Estimation of Various Forces Acting on a Particle in a Fluid Environment

We have calculated the magnitudes of various forces including electric thermo flow force, resistive drag, gravity, and buoyancy acting on a moving object in a fluid and compared to iDEP. We have used the DNA (R = 600 nm) and velocity of 1 mm/s, which are comparable to our experimental conditions.

First, we estimated gravitational force acting on DNA, $F_g = mg = 5 \times 10^{-19}$ N, which is negligible compared to iDEP estimated by the CM factor model (18 nN and 41.5 nN).

Second, buoyant force can be calculated by $F_B = \rho g V$, where ρ is the density of the buffer (water), and $V = 4\pi r^3/3$ is the volume of DNA in the spherical model in buffer. F_B in this assumption is 2.8×10^{-15} N, which is not comparable to iDEP.

Third, we estimated drag force by $F_{drag} = 0.5 C_d \rho A v^2 + 6\pi\eta r v$, where C_d is drag coefficient ranging from 0.1 to 1, A is the cross section of an object moving in liquid, v is the velocity of an object, and η is viscosity [35], [36]. The former term is responsible for the particle moving rapidly with the high Reynolds number, and the latter term of $6\pi\eta r v$ corresponds to the particle moving slowly with the low Reynolds number. The total possible drag force was estimated to be 1.02×10^{-11} N, which is less than 1% of iDEP.

Finally, we estimated the electric thermo flow force induced by applying AC voltage between two parallel electrodes. The time average force acting on a unit volume is described by, $< f >= -M(\omega, T)\left(\frac{\varepsilon\sigma {V_{rms}}^4}{2k\pi^3 r^3 T}\right)\left(1 - \frac{2\theta}{\pi}\right)$, where M is a dimensionless factor depending on applied frequency with its value $|M| < 7$ at the frequency less than 1 MHz [37]. Here, ε is permittivity, σ is conductivity, k is thermal conductivity, and T is temperature. θ and r are cylindrical coordinates, respectively, and the origin is located at the middle of two parallel electrodes. We calculated the maximum force by using the maximum of $M(\omega,T) \sim 6.5$ and $\theta = 0$. At r = 10 μm,

the maximum value of electro thermal fluid force is estimated as $< f >_{max} \sim 6.5 \left(\frac{\varepsilon \sigma {V_{rms}}^4}{2k\pi^3 r^3 T}\right) = 9.65 \times 10^{-17}\ N/\mu m^3$, which is not comparable to iDEP.

Taken together, our iDEP tweezers enable us to spatially manipulate objects in a fluid, and therefore, our DNA manipulation experiments with iDEP are justified.

Experimental Section

Device Fabrication and Measurement Setup

The interdigitated electrode arrays are prepared by the standard optical lithography technique on a SiO_2 substrate as described previously [38]. The width of electrodes, gaps between the electrodes, and the height of the electrodes were 16 μm, 25 ~ 40 μm, and 140 nm, respectively. The insulator tips were made from glass rods (Harvard Apparatus, 1.0 mm diameter, 75 mm length) and fabricated by a two-end pulling method using a micropipette puller (MicroData Instrument), placed between two gold electrodes, and manipulated through an xyz manipulator (Miller Design & Equipment) while trapping, moving, and releasing biomolecules. The external AC voltage between the electrodes was applied by a commercial function/arbitrary waveform generator (Agilent 33220A). These devices were mounted on a low-power fluorescent microscope (OMFL600), and all experiments were performed in either a PBS or TE buffer without evaporation while measuring. All images and videos were recorded through a CCD camera and analyzed using the ImageJ software.

DNA Labeling and Preparation

The iDEP tweezer capability was tested with the polystyrene particles and DNA. The fluorescently labeled polystyrene particles with a diameter of 500 nm were purchased from Phosphorex (λ_{Ex} = 460 nm, λ_{Em} = 500 nm). A 5 μl of the particle solution diluted into 0.001× PBS buffer was deposited on the devices before DEP measurements. The double-stranded λ-

DNA fragments (48,502 base pairs and mix of 3,550 – 21,226 base pairs, New England Biolab) were purchased and labeled with YOYO-1 (λ_{Ex} = 491 nm, λ_{Em} = 509 nm, Thermo Fisher Scientific) at a ratio of five base pairs per YOYO-1 molecule in a 0.01× TE buffer prior to use. Similar to the polystyrene particle measurements, a 5 µl of the labeled DNA solution was deposited on the devices before the manipulation experiments.

COMSOL Simulation

The distribution of the electric fields and the electric field gradients across the electrodes and the tips were calculated using commercial finite element software, COMSOL Multiphysics 5.3a (COMSOL, Inc.). To set-up COMSOL simulations, the interdigitated electrodes, and the insulator tip along with the buffer layer were drawn to scale using AutoCAD software (Autodesk) and imported into COMSOL software. The AC/DC electric current module and frequency domain studies were used to calculate electric fields and the electric field gradients. A buffer solution (σ_m= 10^{-3} S/m and ε_m = 78ε_o for 0.001 × PBS buffer, σ_m= 5 × 10^{-4} S/m and ε_m = 78ε_o for 0.01× TE buffer) was filled over the electrodes as used in the experiments. The sinusoidal potential of 7 V peak to peak at 50 ~ 200 kHz was applied to the electrodes. Finally, the device geometry was meshed with customized mesh. The electrodes and the tip were meshed by extremely fine, free triangular meshes with a maximum element size of 300 nm and a minimum element size of 1 nm. We used a swept mesh on the buffer volume with the maximum element size of 1 nm, the minimum element size of 0.01 nm, the curvature factor of 0.6, and the resolution of narrow regions of 9, in order to increase the number of elements in the mesh, thereby providing better accuracy.

Results

Modeling of the Electric fields and the Field Disturbance

Our iDEP tweezers exploit the interdigitated electrode array which has proven to be quite useful for dielectrophoretic separation in previous studies [37]–[39]. The device consists of planar gold electrode arrays defined by the standard optical lithography technique on a SiO_2 substrate, similar to our previous work [38], [40] (Figure 6) and an insulator tip controlled by an xyz manipulator between a pair of interdigitated electrodes.

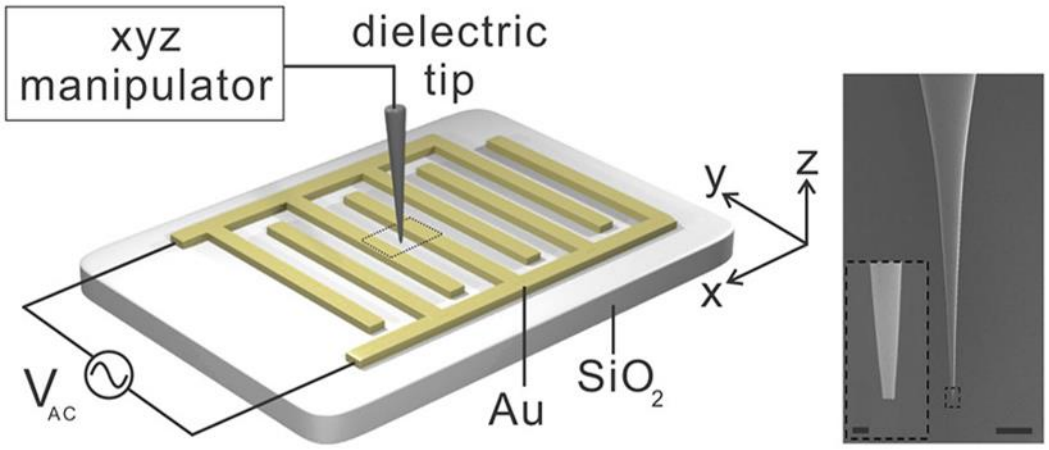

Figure 6. Schematic diagram of the device and zoomed-in SEM images of the insulating tip controlled by the xyz manipulator. The scale bars are 500 and 2 μm.

The strength of the electric field intensity gradient ∇E^2 in the proximity of the tip was examined using the COMSOL Multiphysics. Figures 1d and 1e depict the spatial distributions of ∇E^2 over and across the electrodes when an external AC voltage V_{ac} (7 V_{pp}, f = 50 kHz) is applied between two electrodes. Without the tip, the strong ∇E^2 were formed only at the sharp electrode edges due to the inhomogeneity of the electric field created by the external AC voltage, which agrees with our previous experimental observations [38], [41]. In the presence of the tip between the two electrodes, an additional strong ∇E^2 around the tip end was created (Figure 7 and Figure 8). The insulator tip deformed the electric field in the conducting solution and

generated inhomogeneous field gradients with a local maximum surrounding it, suggesting strong DEP at the tip end ($F_{DEP} \propto \nabla E^2$).

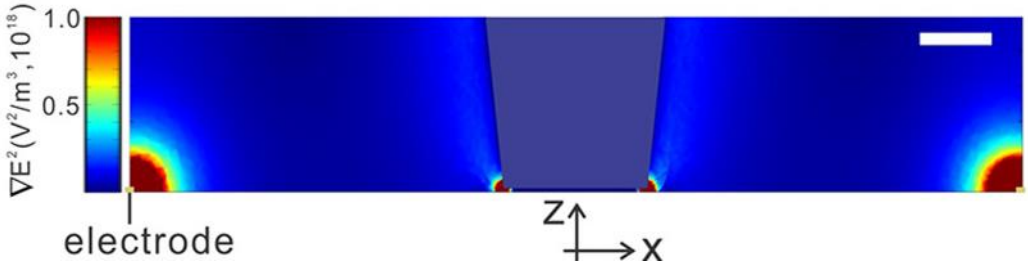

Figure 7. The distribution and the strength of the electric field gradient around the tip calculated by the finite element COMSOL simulation, predicting the strong field gradient at the electrode edge and the tip and. The scale bar is 5 μm.

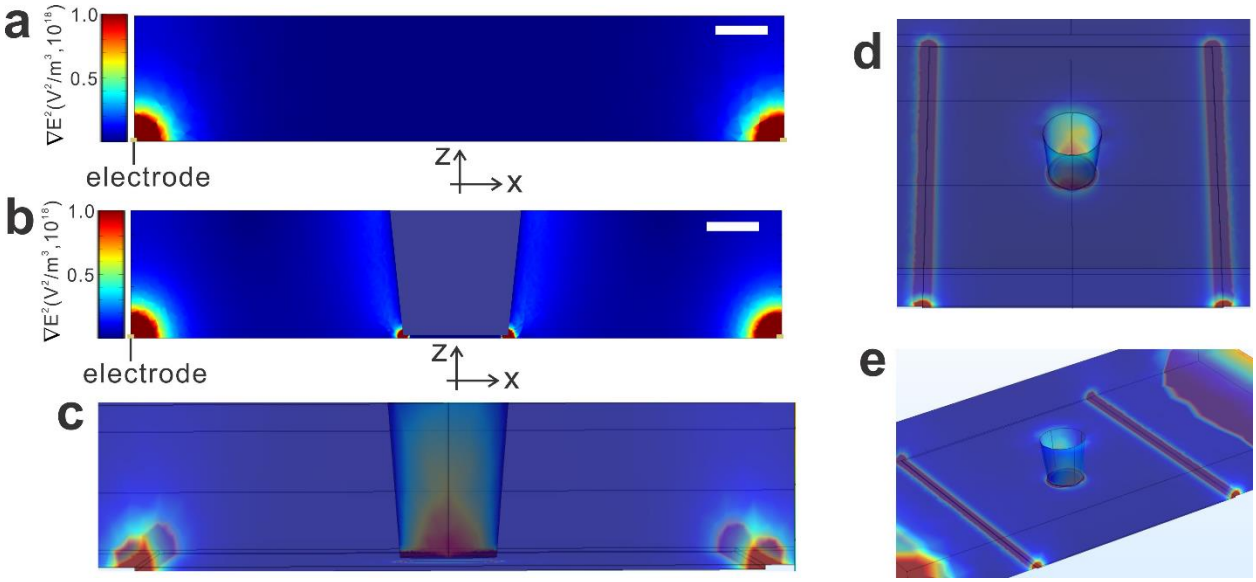

Figure 8. The distribution of ∇E^2 calculated by COMSOL simulation. (a) Localized ∇E^2 at the both electrode under AC voltage V_{ac} (7 V_{pp}, f = 50 kHz). The scale bar is 5 μm. (b) Distribution of the additional localized ∇E^2 at the tip. (c) Cross sectional view of ∇E^2 distribution. (e) Top and (e) side view of ∇E^2 distribution.

The distribution of ∇E^2 along the x-axis demonstrates that ∇E^2 increases near the tip and maximizes at the tip edge (Figure 9). Compared to the flat surface of the tip end, the edge line of the tip end is highly disordered, which produces additional non-uniform electric field distribution. The ∇E^2 peak sharply drops to the relatively flat ∇E^2 along the x-axis,

demonstrating that the effective iDEP site is physically smaller than the tip. The effective trapping volume at the tip depends on the tip diameter because the distribution and centration of ∇E^2 around the tip varies with the tip dimension (Figure 10 and Figure 11). Therefore, the unbiased insulator tip producing an additional localized iDEP trap is able to serve as a spatially mobile and remotely tunable biomolecule tweezers, in order to trap, relocate, and release the nanoscale objects.

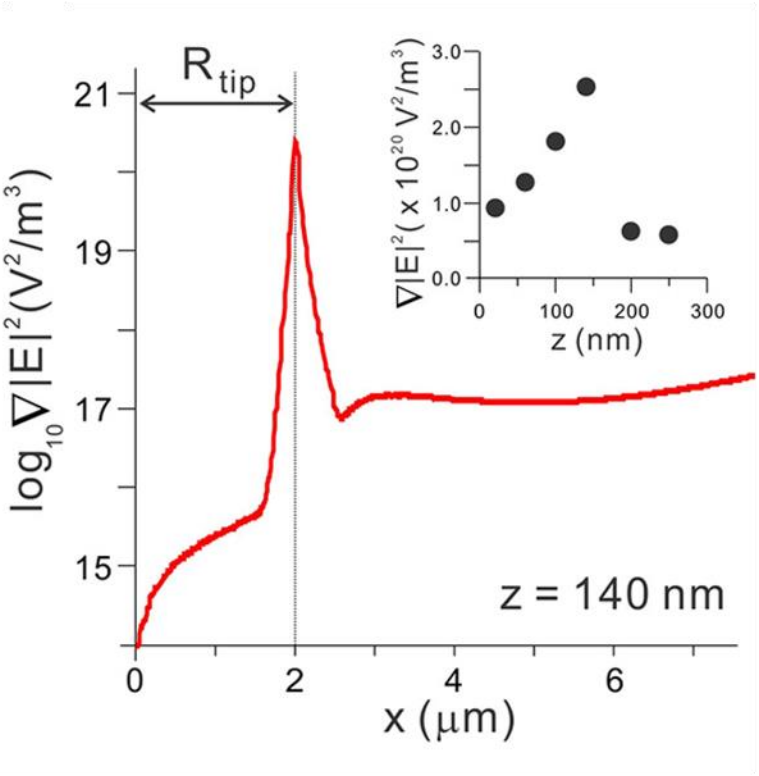

Figure 9. The line profile of the electric field gradient along the x-axis at the tip height z of 140 nm, showing a very sharp peak of the field gradient at the rim of the tip. The inset presents the peak values of the field gradient's strength as function of z.

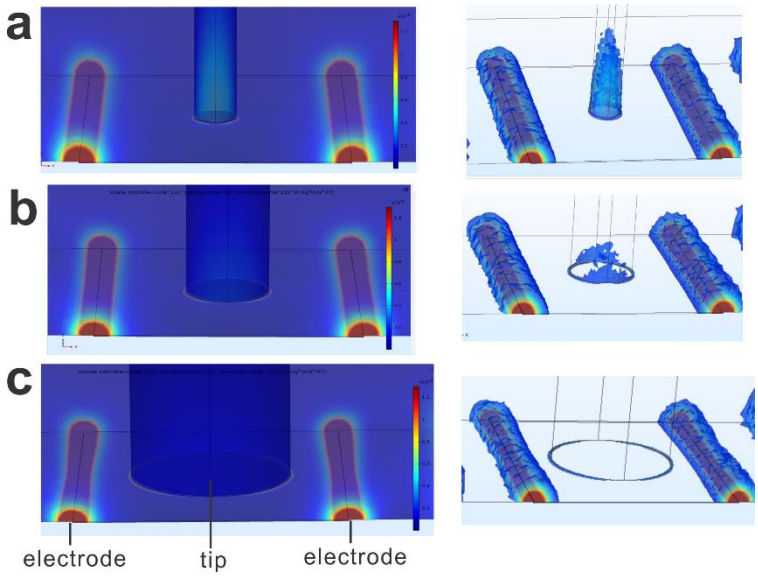

Figure 10. The distribution of ∇E^2 around the tip with its diameter of (a) 4 μm (b) 5 μm, and (c) 15 μm. For the small tip, the concentrated field at the tip is proportional to the area of the tip (πr^2). In contrast, the field partially interacts with the large tip. Thus, about a quarter of rim contacts with each electrode, and the effective trapping volume is proportional to the circumference of the tip (πr). Our experiments show that the tip diameter of 4 ~ 8 μm offers the most effective trapping of the particles and DNA in our devices.

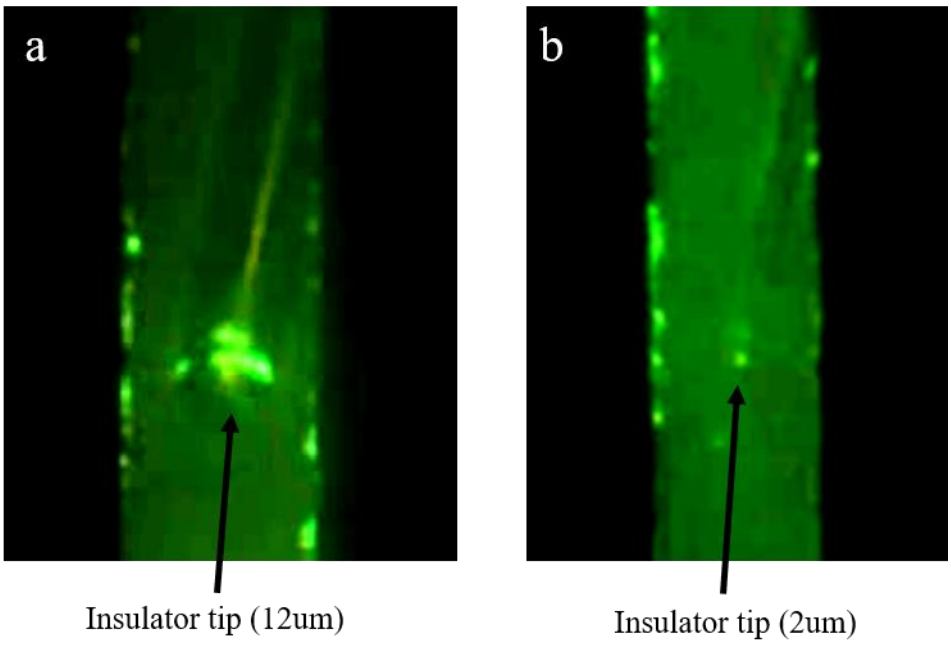

Figure 11. Difference trapped volume of polystyrene beads between (a) 12μm of insulator tip and (b) 2μm of insulator tip.

Fluorescence Imaging of the Sub-micron Particles with the iDEP Tweezers

To demonstrate the feasibility of the iDEP tweezers in relation to transport and mobility, we initially examined the polystyrene particles (Figure 12 and Figure 13). First, the capability of traditional DEP acting on the particles was measured in the absence of the tip (Figure 12a-12c). In the absence of both AC voltage and the tip, the particles were freely diffusive in the buffer (Figure 12a). When the low frequency AC voltage (5 V_{pp}, f = 20 kHz) was applied, the particles were attracted to the electrode edge due to the positive DEP (pDEP, Figure 12b). In contrast, the high frequency AC voltage (5 V_{pp}, f = 2 MHz) repelled the particles, so the particles were accumulated in the center between the two electrodes, where the electric field gradient is minimum (nDEP, Figure 12c). These frequency-dependent, bipolar DEP results were in excellent agreement with the classical Maxwell-Wagner (MW) theory[8], [9], where the Clausis-Mossotti (CM) factor and the cross over frequency f_{co} of 0.7 MHz allow for the estimation of the frequency dependent F_{DEP} polarity (Figure 4).

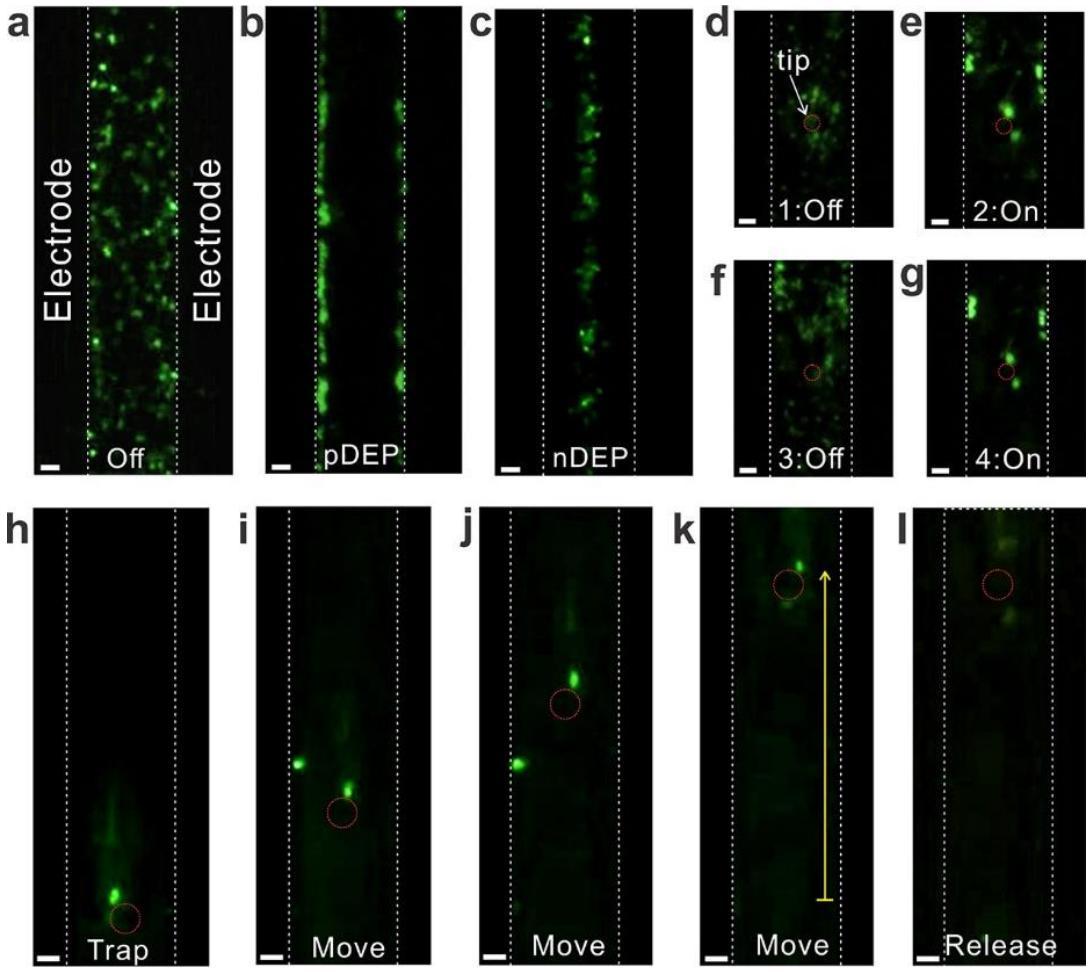

Figure 12. The iDEP manipulation of fluorescently labeled polystyrene nanoparticles. (a)-(c) DEP acting on the nanoparticles without the tip: (a) No AC field between the electrodes; (b) Low-frequency AC voltage (5 V, 20 kHz) attracts the nanoparticles to the electrodes (pDEP); and (c) High-frequency AC voltage (5 V, 2 MHz), in contrast, repels the nanoparticles to the center of the electrodes (nDEP). (d)-(g) In the presence of the tip, the nanoparticles were trapped around the tip when the AC voltage was applied (5 V, 20 kHz), and the trapped nanoparticles were instantly released from the tip after turning the AC voltage off. (h)-(l) The iDEP tweezers trap the nanoparticles, hold them while repositioning, and release them by turning off the AC voltage (5 V, 20 kHz). The yellow arrow is 80 μm. All scale bars are 5 μm.

Next, the particle trapping at the tip placed in the center of two electrodes was investigated. Figures 12d – 12g demonstrate a series of measurements regarding the trapping of the particles at the tip by turning on and off the AC voltage between the electrodes. By turning on the pDEP trap bias, the particles were attracted to the high electric field near the tip and trapped at the tip end (Figure 12e). The trapped particles were immediately released and

diffused away from the tip after turning off the pDEP trap bias (Figure 12f). When the trap bias was reapplied, the particles were trapped again in similar fashion at the tip (Figure 12g). Such trapping and releasing of particles were reproducible.

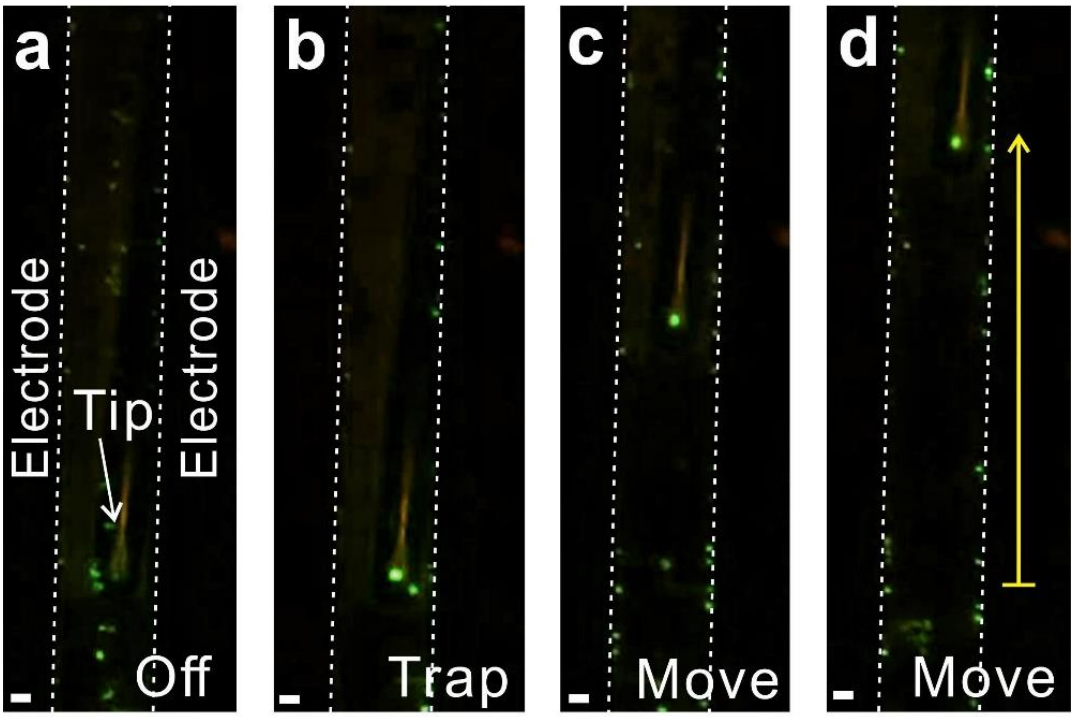

Figure 13. Additional example of nanoparticle manipulation. (a) No AC bias. (b) – (d) Trapping and repositioning of the particles at the tip with the pDEP bias (5 V, 20 kHz). The yellow arrow is 112 µm. The scalar bar is 5 µm.

After trapping particles, the tip was spatially manipulated. Figures 12h – 12k are a sequence of images that show the motion of the tip and particles along the y-axis (yellow arrow). During the tip manipulation, the position and shape of the trapped particles were almost identical without further interferences from the electrodes. Following the repositioning of the tip and particles, the trap bias at the electrodes was turned off (Figure 12l). The particles were immediately released from the trap and freely diffused away from the tip. Thus, the iDEP at the tip is strong enough to trap and hold the particles while repositioning, in order to use the tip as nanoscale mobile tweezers. Please note that the particles drawn into the pDEP trap at the

electrode were not shown in Figures 12h – 12k because some electrodes have smooth edges. Although the particles were still trapped on the electrodes, the particles on the Au electrodes could not be seen by the objective placed under the devices.

Spatial Manipulation of DNA with the iDEP Tweezers

Following the examination of the particles with the iDEP tweezers, we further investigated the capability of the iDEP tweezers in manipulating DNA (Figure 14 and Figure 15). Compared to the particles, prediction of DEP strength and f_{co}, determining polarity of DEP for DNA is very complicated[10], [31]. Several models including the CM factor [6], [25], quantitative measurement of the DNA polarizability α [42]–[45], and the counterion fluctuation (CIF) [10], [31], [33] have been proposed to estimate DEP strength and polarity acting on DNA. Although f_{co} is not exactly defined in those models, the polarity of DEP could be reversed at reasonably separated upper and lower frequency limit.

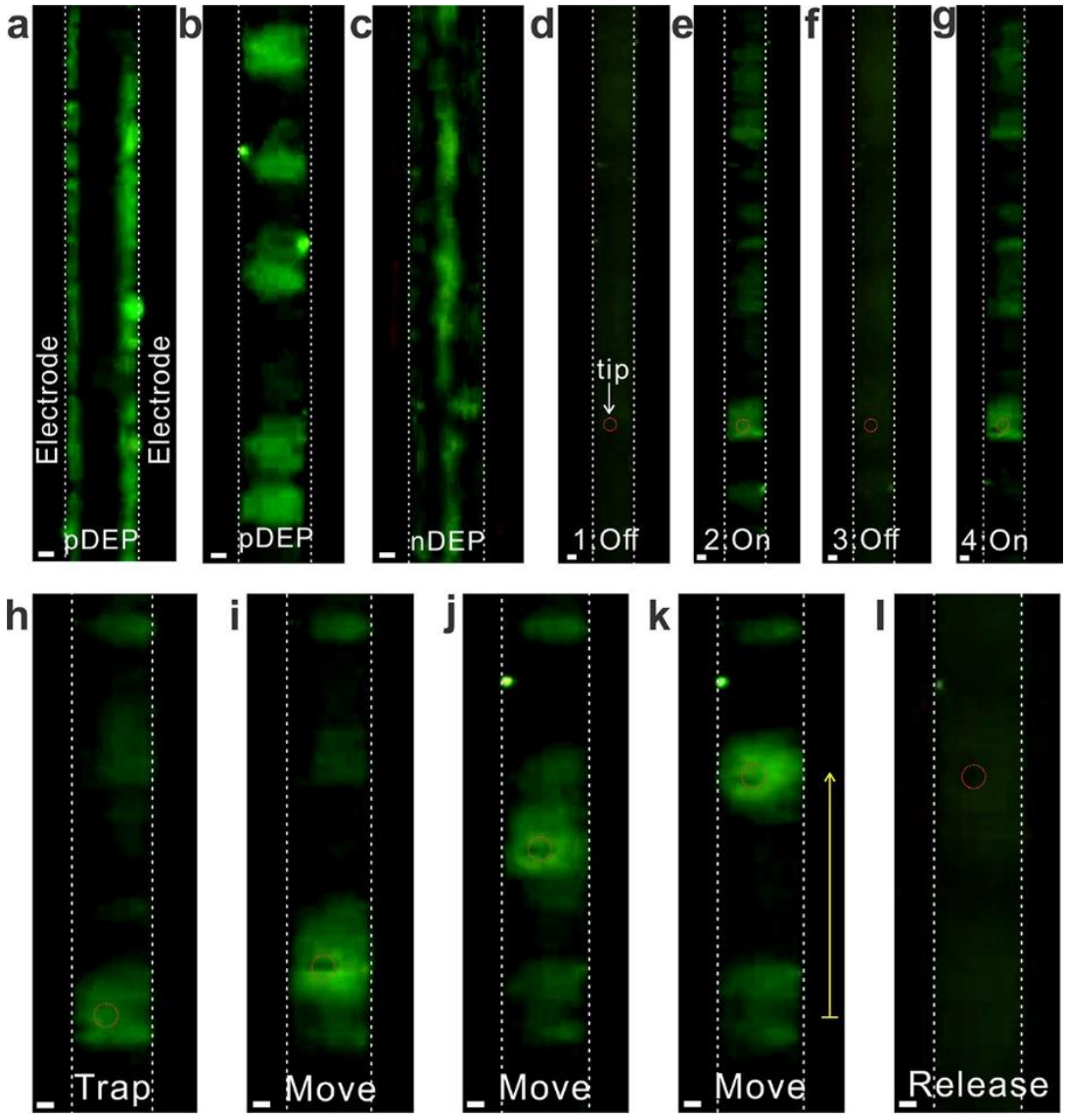

Figure 14. Spatial manipulation of DNA using the iDEP tweezers. (a)-(c) DEP acting on DNA without the tip: (a) Low-frequency AC voltage (7 V, 50 kHz) strongly attracts DNA to the electrodes (strong pDEP); (b) By increasing the frequency of AC voltage (7 V, 200 kHz), DNA were trapped in the middle of two electrodes, forming the DNA clouds (weak pDEP); and (c) High-frequency AC voltage (7 V, 10 MHz) repels DNA to the center of the electrodes (nDEP). (d)-(g) In the presence of the tip, the iDEP tweezers picked up DNA around the tip under the weak pDEP condition (7 V, 200 kHz), and trapped DNA were immediately released from the tip after turning the AC voltage off. (h)-(l) The iDEP tweezers trap DNA, hold them while repositioning, and release them by turning of the applied AC voltage (7 V, 200 kHz). The yellow arrow is 70 μm. All scale bars are 5 μm.

Similar to the particle manipulation, we first examined bipolar DEP acting on DNA (Figures 14a – 14c). When a low frequency AC voltage was applied (7 V_{pp}, f = 50 kHz), DNA

was attracted to the edge of electrodes (Figure 14a). After increasing the frequency of the applied AC voltage (7 V_{pp}, f = 200 kHz), DNA moved off from the electrode and trapped between two electrodes, forming stretched-DNA clouds (Figure 14b). Such DNA cloud observation at the interelectrode gaps by the weak pDEP trap agrees with previous observation with the DNA plasmid [31], [43]. At a sufficiently high frequency (7 V_{pp}, f = 10 MHz), the DNA was repelled from the electrodes and aligned at the center of the two electrodes (Figure 14c). Therefore, the low and high frequency AC voltages yield both pDEP and nDEP on DNA, suggesting bipolar CM factors.

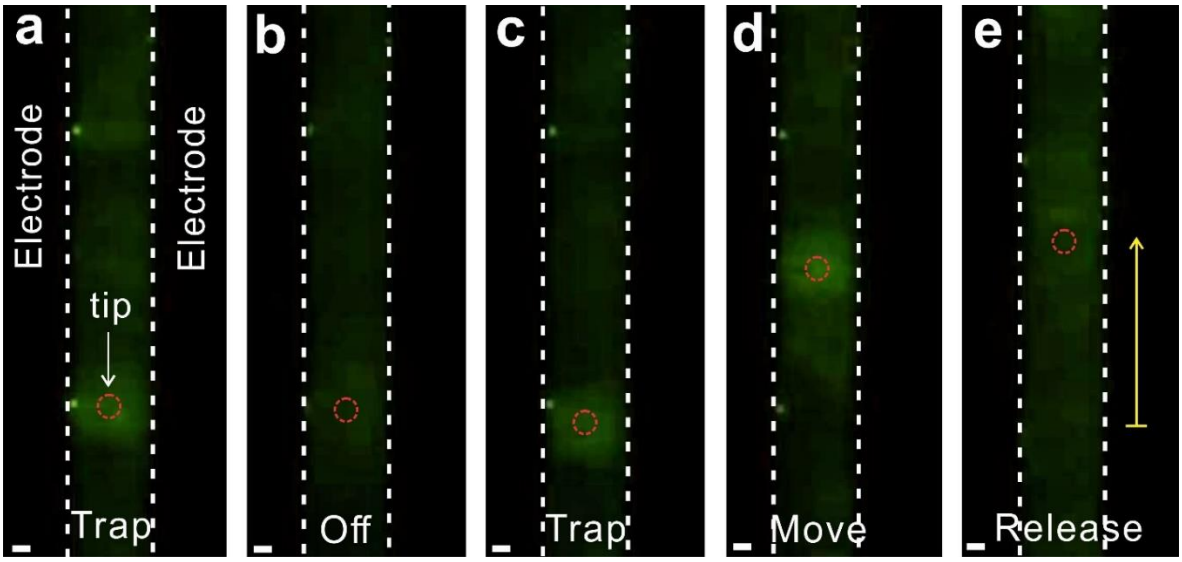

Figure 15. Additional example of homogeneous (48,502 base pairs) DNA manipulation under the pDEP bias (7 Vpp, f = 200 kHz). (a) Tapping, (b) releasing, (c) re-trapping, (d) repositioning, and (e) releasing of DNA at the tip (the red circle). The yellow arrow is 56 μm. The scalar bar is 5 μm.

By placing the tip between a pair of interdigitated electrodes, the utility of the iDEP tweezers in trapping DNA was subsequently examined (Figures 14d – 14g). When the bias of pDEP trap (7 V_{pp}, f = 200 kHz) was turned on, DNA was attracted to the tip, forming a broad, cloud-like structure surrounding the tip. Compared to the particles which are solid spheres, DNA is a long polymer chain, so the structure of DNA varies under different environments (e.g., pH,

ionic strength, force acting on DNA). Thus, such broadening could be attributed to the stretched structure of DNA [45], [46]. When the pDEP trap vanished by turning off the applied AC bias, the DNA clouds completely disappeared around the tip, indicating that the iDEP tweezers can instantly trap and release DNA without any permanent attachment at the tip or damage due to the direct contact of the metal electrodes applied at a high AC voltage.

Finally, the trapped DNA was manipulated by moving the tip along the y-axis (Figure 14h - 14k). The DNA clouds initially formed around the tip, and followed the direction of the moving tip. Throughout the manipulation, the volume and shape of the clouds were almost identical. These results suggest that our iDEP tweezers can tightly hold DNA, and that the trapping strength is consistent in the devices. Such capabilities are prerequisite for the precise measurements of protein properties and activities while controlling and manipulating proteins [22]. Following the repositioning the DNA clouds, the AC bias of the pDEP trap was turned off. DNA were completely released from the tip as shown in Figure 14l. Such trapping and manipulating of DNA with iDEP tweezers were reproducible with both homogeneous DNA (48,502 base pairs) and nonhomogeneous mixed DNA containing 6 fragments from 3,550 – 21,226 base pairs (Figure 16).

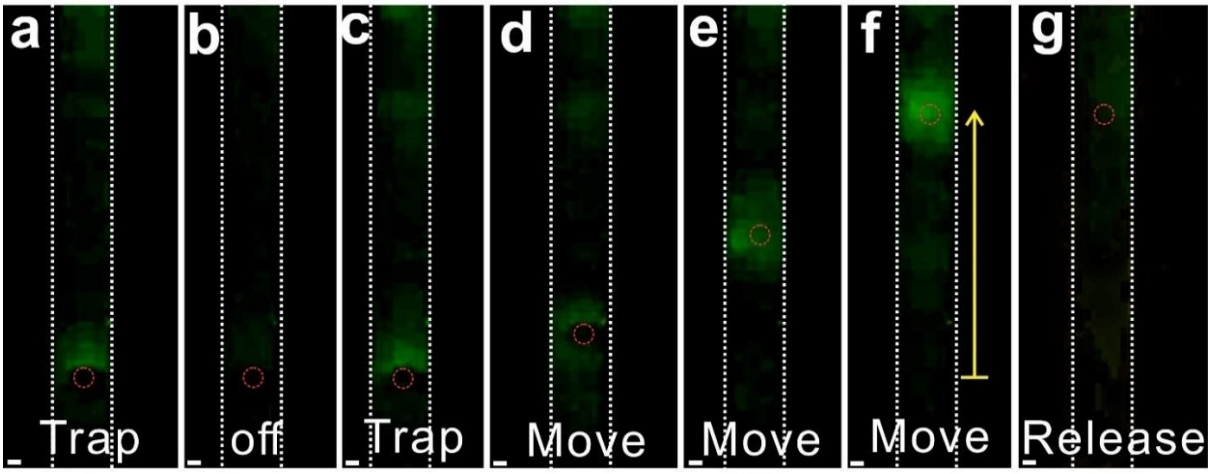

Figure 16. Spatial manipulation of nonhomogeneous mixed DNA containing 6 fragments from 3,550 – 21,226 base pairs under the pDEP bias (7 V_{pp}, f = 200 kHz). (a) Tapping and (b) releasing of DNA at the tip (the red circle). (c)-(f) The motion of the tip with trapped DNA along the y-axis. The yellow arrow is 100 μm. (g) Instant release of DNA at the tip by turning off the trap bias. The scalar bar is 5 μm.

Discussion

Taken together, results from fluorescence imaging of the sub-micron particles and DNA demonstrate the effective control and manipulation of objects using the iDEP tweezers. In principle, our iDEP tweezers enable us to manipulate nanoscale particles (R > 11 nm) by comparing them to the competing thermal force ($F_{th} = k_BT/2R$) [6], [47]. Here, we briefly discuss the physical mechanisms of the iDEP of DNA to guide design rules for creating effective iDEP tweezers for general use of other biomolecule control and manipulation measurements.

Depending on the dielectric responses of the objects and the surrounding medium, the external fields induce an instantaneous force $F_{DEP} = ¼\alpha\nabla|E|^2$ acting on the objects with the effective polarizability α of the object, which is associated with the frequency-dependent CM factor [8], [9]. For the spherical particles, spatially asymmetric force due to the inhomogeneous field gradient in the medium drives the movement of the polarized particles either by attracting or repelling them from the medium to regions of strong electric fields, such as the electrode edge

or the tip end. Such frequency-dependent CM factors, polarizability, and DEP are in excellent agreement with many experimental observations and computational simulations, ours included [1], [38].

Unlike the dielectric particles, precise identification of α values for DNA and the influence of DEP on DNA are not understood [48], since DNA is not a spherical particle but rather a long biopolymer where the negative charges of DNA are fixed at the backbone. Taking into account the DNA shape, the real part of α values of DNA could be estimated using either the traditional CM factor approach [6], [25], the recent CIF model [10], [31], [33], or experimental measurements [42]–[45]. By assuming the stretched DNA as ellipsoid, the axis-dependent α of the CM factor model is given by $\alpha = 6v\varepsilon_m Re[K]$, where $K = \frac{\varepsilon_p^* - \varepsilon_m^*}{3[L_n(\varepsilon_p^* - \varepsilon_m^*) + \varepsilon_m^*]}$, L_n, v, $\varepsilon_m{}^*$, and $\varepsilon_p{}^*$ are the complex CM factor, depolarizing factor, volume of the particle, and complex permittivity of the medium and particle, respectively [49]. The polarizability values found from the CM factor model were 6.53×10^{-28} Fm^2 at f = 50 kHz, 2.87×10^{-28} Fm^2 at f = 200 kHz, and -2.59×10^{-31} Fm^2 at f = 10 MHz, which yielded the DEP strength of 41.5 nN at f = 50 kHz, 18.3 nN at f = 200 kHz, and nDEP -16.5 pN at f = 10 MHz under constant AC voltage (7 V_{pp}).

Alternatively, the CIF model, in which the redistribution of counterions surrounding DNA under the AC fields is responsible for the movements of DNA, enables an estimate of the total polarizability given by $\alpha = \frac{z^2 q^2 {L_s}^2 n_{cc} A_{st}}{12 k_B T} \frac{l_{DNA}}{L_s}$, where z, q, L_s, n_{cc}, A_{st}, l_{DNA}, k_B, and T are the valence of counter ion, the electric charge, the subunit length, the number of condensed counter ions, the stability factor of the ionic phase, the contour length of DNA, the Boltzmann constant, and the temperature, respectively [10], [31]. The total polarizability of the CIF model varies from 1.52×10^{-29} to 1.52×10^{-28} Fm^2 depending on the dielectric increment $\Delta\varepsilon$ values (see Experimental Section for details) [32], [33]. For the 48,502bp DNA, the polarizability per base

pair yields values from 3.12×10^{-34} to 3.12×10^{-33} Fm^2/bp, which agree with those determined by the experiment measurements and are within the range quoted in the literature [42], [50]. Thus, the CIF model predicts the DEP strength of 0.962 ~ 9.62 nN. Unfortunately, the CIF model does not allow the reasonable estimation of both pDEP and nDEP since the α values were remarkably insensitive to the frequency range, with only a 3-fold difference for a frequency that differs by 10^3-fold [32], [43].

Although previous DEP measurements with DNA have demonstrated the pDEP trap around the electrode or obstacles, no experiments have discussed nDEP, or the strength of nDEP that was simply assumed to be identical to pDEP with the reversed sign (i.e., nDEP = -|pDEP|) [51]. However, the observations of both pDEP and nDEP rely on the experimental limitations associated with either the DEP operating parameters (e. g., AC voltage, frequency, buffer, DNA fragment and concentration) or the design of the DEP device.

In addition to the polarity of DEP from those models, there is disagreement about the magnitude of DEP between them. First, the strength of pDEP, compared to the nDEP values obtained by the CM factor calculation, is substantially increased by almost three orders of magnitudes. The overestimation of pDEP is originated by the ellipsoidal assumption of DNA in which the effective polarization is different along each axis. In particular, a prolate spheroid or highly elongated (needle-shaped) object tends to align itself with its longest axis parallel to the external fields regardless of positive or negative DEP [8], which resulted in highly asymmetric CM factor values at a low frequency regime (Figure 5). Such alignment behavior of the DNA could further lead to stretching them between two electrodes under the weak pDEP as shown in Figure 3b. Second, the pDEP values estimated from the two approaches differ by nearly a factor of 2 ~ 40. This difference is attributed to the assumption of DNA as a rigid rod in the CM factor

model, which enhances its polarizability in a longitudinal direction and increases subunit length L_s in the CIF model.

The CM factor calculation allows us to estimate f_{co} = 6.5 MHz and bipolar DEP (Figure 5), which conforms to our experimental observations of pDEP and nDEP behaviors. Despite such valuable information from the CM factor model, the charge redistribution under the AC fields is inapplicable to DNA because the negative charges are fixed to the DNA backbone. While the CIF model considers the counterion fluctuation and its contribution to the polarizability of DNA under the AC fields, the polarity and frequency-dependence of nDEP cannot be derived from the model. Thus, further studies are needed to address the polarization mechanism for DNA under the influence of the non-uniform AC fields.

In any case, the theoretical evaluation of the DEP must be stronger than the thermal force $F_{th} = k_B T/2R_H$, driving the Brownian motion of particles with a hydrodynamic radius R_H at room temperature T, due to its interference with the DEP manipulation [6]. Using the worm-like chain model[34], the radius of gyration ($R_g \approx 1.54R_H$) of DNA was estimated to be 606 nm, which resulted in F_{th} of 5.23 fN. These results also suggest a minimum strength of ∇E^2 of 8.08×10^{16} V^2/m^3 at the trapping site to overcome the thermal diffusion. Thus, the theoretical predictions of pDEP, nDEP, and $\nabla E^2$from both models are at least 4 orders of magnitude larger than F_{th} and the minimum requirement of ∇E^2 for trapping and spatial manipulation of DNA at the tip as demonstrated in Figure 14.

Finally, the effective volume and trapping pattern of DNA are examined. The effective trapping distance from the tip end to the end of the trapped particles and DNA was measured to be approximately 3 – 8 μm, depending on the direction of the measurements. Considering the R_H of 393 nm and the contour length of 22 μm, the trapping distance and pattern suggest that the

individual DNA is neither randomly coiled nor perfectly stretched. Instead, the DNA could be partially stretched under the AC fields, forming widely spread cloud structures around the tip end (Figure 14). Such cloud effects due to the partial stretching of DNA trapping was also observed when the pDEP conditions were changed (Figure 17). After increasing the frequency from 80 kHz to 200 kHz of the applied AC voltage (9 V_{pp}), DNA formed like clouds between two electrodes. In general, high frequency lowers the strength of DEP due to the decrease of the frequency-dependent CM factor in the CM factor model (Figure 5) and the total polarizability of the DNA in the CIF model [45], [50] and the experimental observations [32], [43]. Thus, the DNA cloud effects could be partially stretched DNA molecules due to the weak pDEP, which has been also previously observed [31], [43]. The experimental observation of the DNA trapping pattern manifests the strong dependence of DNA's α value on the frequency of the AC fields.

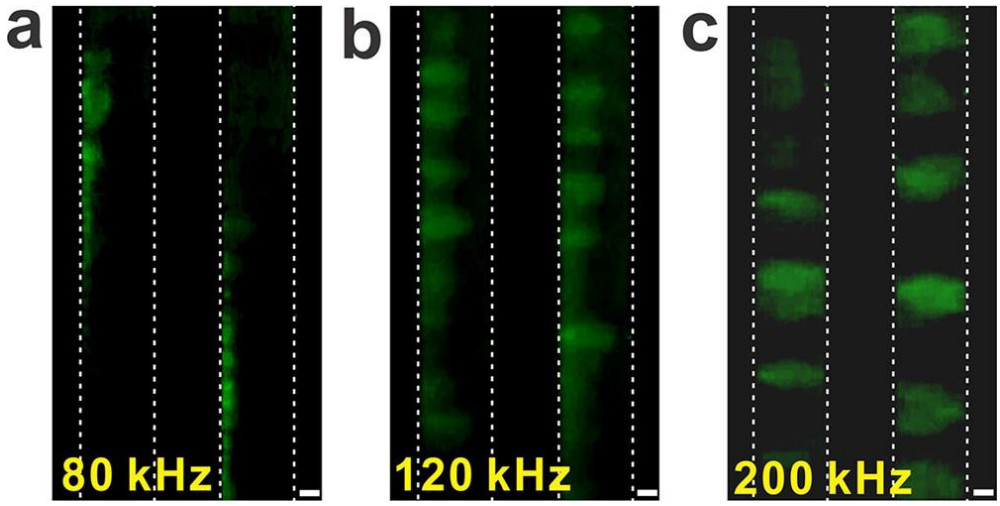

Figure 17. Frequency dependent DEP and the DNA trapping pattern. (a) The low-frequency AC voltage generates strong pDEP, attracting DNA to the electrode (9 V, 80 kHz). (b) After increasing the frequency of the AC voltage (9 V, 120 kHz), DNA experiences slightly reduced pDEP, which causes the trapped DNA to partially move off from the electrode. (c) After further increasing the frequency of the AC voltage (9 V, 200 kHz), the DNA were fully stretched between the electrodes, indicating a significant dependence of the DEP strength and the DNA polarizability on the frequency of the applied AC voltage. The scale bar is 10 μm

Conclusion

By linking an insulator tip and conventional dielectrophoretic method, we have demonstrated that our iDEP-based molecular tweezers can trap, carry, reposition, and release the sub-micron particles and DNA. The technique allows a simple and effective separation in a fluid environment without potential issues such as fouling, electrolysis, and joule heating associated with traditional metal-based DEP methods. We have compared two polarization models of DNA, and demonstrated that either model could not fully describe iDEP behaviors of DNA. However, the strength of iDEP tweezers estimated by both models was strong enough to overcome the competing forces acting on a particle or DNA in a fluid, including thermal force and viscos drag. These results enable other researchers to design and determine operating parameters to successfully perform iDEP-based manipulation experiments with a range of biomolecules and biopolymers.

CHAPTER 3. STUDY OF A MOLECULAR DIFFUSION MODEL FOR PLASMA SEPARATION IN MICROFLUIDICS[2]

Introduction

Lab-on-a-chip technologies have shown great promise in portable, point-of-care, and diagnostic platforms for various human diseases, including cancer [52]. Further integration of microfluidics and nanotechnology for medical and biochemical assaying have allowed high-throughput, multiplexed, and comprehensive detection of target biomarkers from complex biological samples, greatly simplifying the detection processes using minimal sample volume [53]–[55]. For example, microfluidic devices for liquid biopsies have shown tremendous potential for early-stage disease diagnosis and monitoring [56], [57]. However, the sensitivity and accuracy of microfluidic-based liquid biopsy relies on the pretreatment of clinical samples such as whole blood, which is a blend of blood cells, extracellular vesicles, and proteins. Thus, the effective separation of blood cells from whole blood and isolation of cell-free serum or plasma containing the target disease biomarkers such as circulating miRNA, circulating tumor DNA, and disease-derived exosomes are critical steps in many microfluidic-based liquid biopsy applications [56], [58]–[60].

Various on-chip, plasma separation approaches have been demonstrated as alternatives to the conventional centrifugation method, which requires intensive time, cost, and labor processes. For example, active approaches utilizing external forces such as acoustic [61], electric [62], and magnetic force [63] have allowed the precise controlling and separating of

[2] The material in this chapter was co-authored by Sung Oh Woo, Myungkeun Oh, Kyle Nietfeld, Bailey Boehler, and Yongki Choi. The content in this chapter was reprinted from Biomicrofluidics 15, 034106 (2021) with the permission of AIP Publishing. Sung Oh Woo and Myungkeun Oh contributed equally and had primary responsibility to perform experiments. Sung Oh Woo and Myungkeun Oh collected and analyzed experimental data.

cells, but have also compromised throughput because of the slow sample flow rate in the microchannel [64]. In contrast, passive approaches including filtration [65], sedimentation [66], and cell deviation [67] exploit the geometries of microchannel structures and hydrodynamic phenomena such as pinched flow fractionation [68], deterministic lateral displacement [56], and hydrophoresis [67], rather than the external forces. Furthermore, the passive microfluidic platform has shown easy and reliable manipulation of cells in a high-throughput fashion.

Among the passive approaches, sedimentation-based plasma extraction methods are particularly advantageous in terms of reducing the common clogging issues in microfluidic devices [57], [69], [70], and providing a potential solution for droplet testing with a small volume of clinical sample and translational applications [71]. For example, a novel sedimentation strategy coupled with a droplet generation system has demonstrated an effective plasma separation with a finger-pricked blood droplet using a capillary pump [72].

However, further optimization and simple design that can eliminate the need of external pumps, power sources, connectors, special tubing, and control equipment are crucial for further development of portable, equipment-free diagnostic devices. An integration of pressure-driven, on-chip, fluid flow propulsion methods with sedimentation could be a solution to drive blood fluid and separate plasma without any external pumps, hydrophilic surface treatment, or complex operational procedures [56], [57], [70].

Here, we report a pressure-driven, tunable pumping method for self-powered poly(dimethylsiloxane) (PDMS) microfluidic devices. We demonstrate that two geometrical parameters of a vacuum pocket in the device determine dynamics of fluid flow in the microchannel, which are in excellent agreement with our analytical expression of the fluid trajectory developed by using a molecular diffusion model and the ideal gas law. Additional

feasibility tests of the on-chip, sedimentation-based plasma separation in self-powered devices fabricated by PDMS and non-PDMS showed plasma separation does not require complicated structures nor an external power source. Finally, the vacuum pocket can be fabricated as a removable vacuum battery and easily integrated with non-PDMS microfluidic devices to drive fluid flow.

Blood Composition

Blood is mainly composed of red blood cells (~ 45%), white blood cells, platelets, plasma and/or serum. Plasma is mainly composed of water (95%) and a very small number of proteins, hormones, cell-free DNA, extracellular vesicles, clotting factors, and other elements. Plasma and serum are very similar, except the plasma contains clotting factors and fibrinogen, and the serum does not. A clot activator, composed of a silica particle, coats the inside of a serum separating tube (SST), which aggregates clotting factors during centrifugation. Once separated, the serum forms the top layer in the tube.

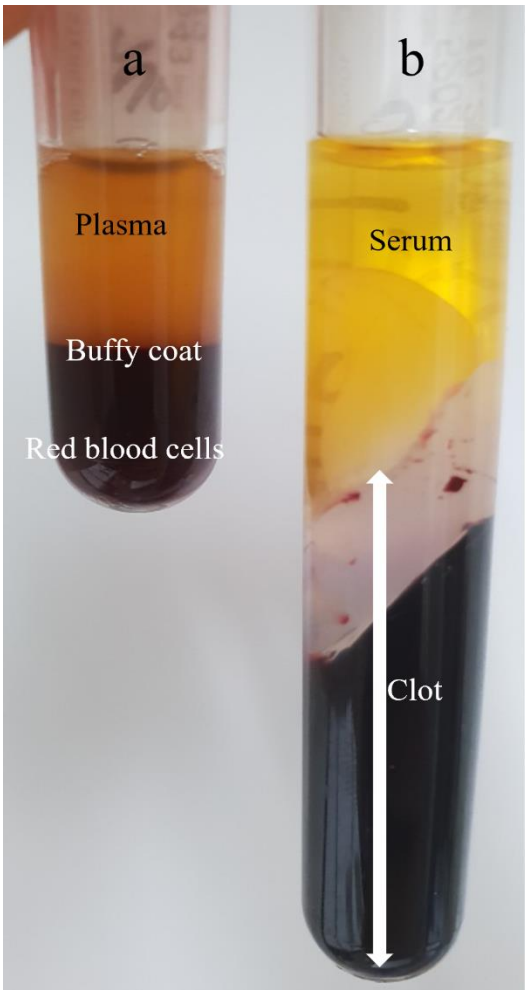

Figure 18. Difference between plasma and serum after blood sedimentation in different tube types. (a) Blood in the EDTA tube after three hours without centrifugation. (b) Blood in the SST tube with centrifugation.

Erythrocyte Sedimentation Rate (ESR)

The erythrocyte sedimentation rate (ESR), otherwise known as the sedimentation (SED) rate, or Westergren sedimentation rate is a measure of the rate of blood cell sedimentation, which helps doctors to diagnose or monitor a patient's inflammatory disease progress in conjunction with other blood tests in a clinic or hospital. The blood samples in Figure 19a and Figure 19b were allowed to settle for approximately three hours, and less than 10mm of blood cells had sedimented. However, in Figure 19c, almost 40mm of blood cells had sedimented after only one

hour. This high sedimentation is a sign of inflammation because aggregation is caused by inflammation, and aggregated red blood cells are denser than individual blood cells.

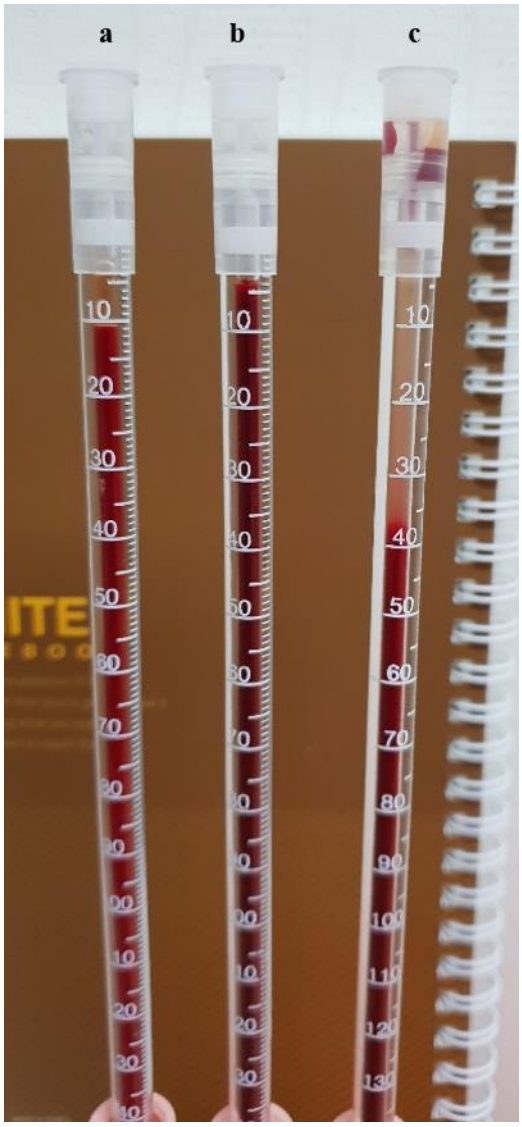

Figure 19. Different ESR of three blood samples. Blood in (a) and (b) was allowed to settle for three hours, but in (c) blood settled for only one hour.

Characteristic of Polydimethylsiloxane (PDMS)

PDMS is a silicon-based polymer. It is a sticky liquid that becomes solid by adding curing agents. Commonly, the curing occurs in an oven for rapid hardening, allowing it to be used for patterning materials from a mold as a soft lithography [73], [74] to prepare microfluidic

devices from many researchers (Figure 20). It has appealing characteristics, including transparency, biocompatibility, low toxicity, gas permeability and absorptivity.

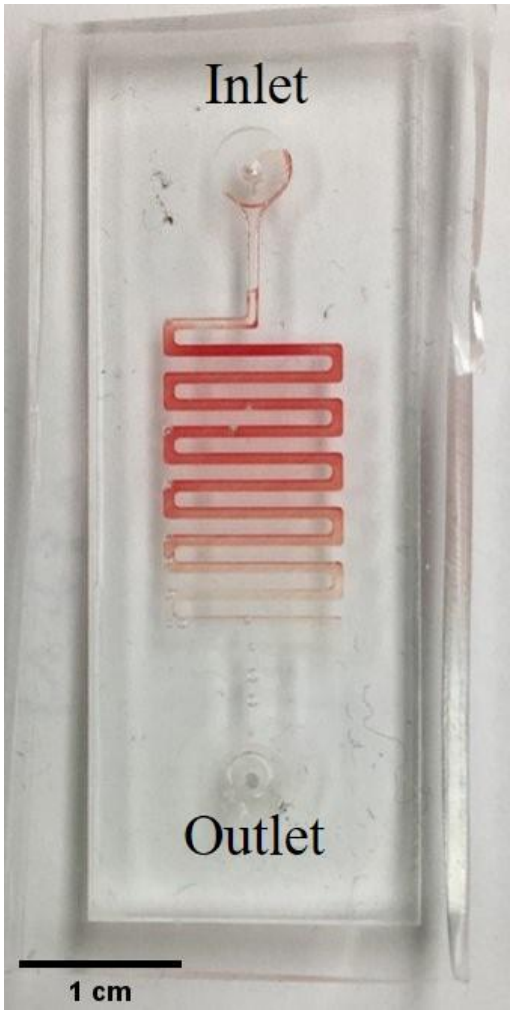

Figure 20. A microfluidic device fabricated using PDMS (20 mm × 50 mm ×3mm, channel width: 0.6 mm, channel height: 0.5 mm, channel length: 96 mm, inlet and outlet diameter: 4mm); 30µl of blood was injected into the inlet, and blood cells sedimented on the bottom of the channel while blood flowed so only clear plasma is collected on the outlet.

In this study, characteristics of gas absorptivity [75] and permeability [76], [77] will be applied for our microfluidic devices. While the microfluidic device fabricated using PDMS is present in the vacuum chamber, air molecules inside the PDMS exit, a degassing step (Figure 21a). Once the device is placed at atmospheric pressure, the degassed PDMS begins to absorb air molecules. If one inlet is filled with a solution, the solution does not flow since air molecules are

supplied from another open inlet (Figure 21b). If two inlets are filled, the two fluids begin to flow. As the number of air molecules in the microfluidic channel decrease, the pressure inside of the channel decreases (Figure 21c).

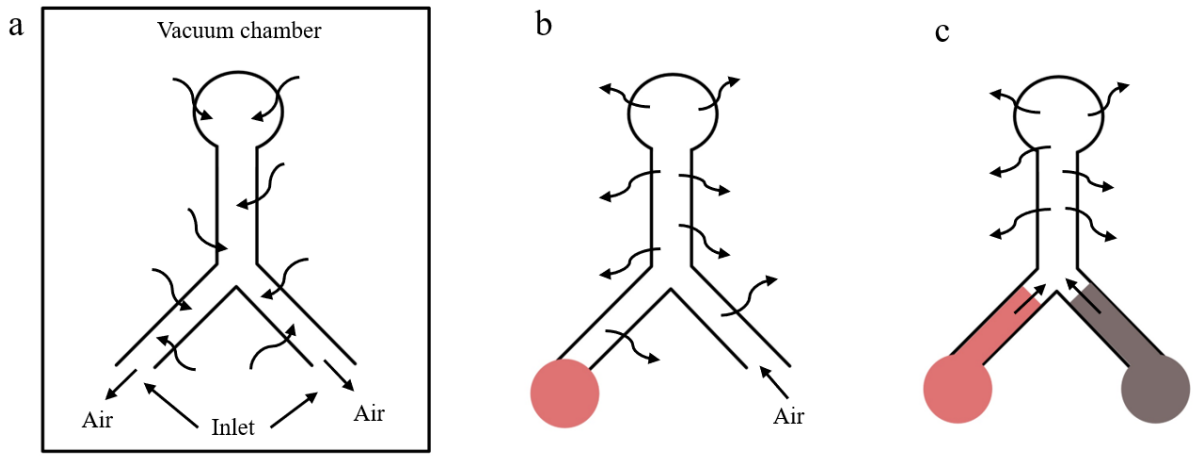

Figure 21. Gas absorption of the PDMS device. (a) The device in the vacuum chamber (degassing step). (b) The degassed device is at atmospheric pressure with one inlet filled. (c) The degassed device is at atmospheric pressure with two inlets filled.

Gas permeability, another PDMS characteristic, was exploited in our microfluidic device. There are two separated microchannels (Figure 22). If the pressure is applied from the right microchannel, the fluid in the left microchannel flows to the right. This movement occurs because air molecules in the left microchannel move to the right microchannel by passing through the PDMS membrane.

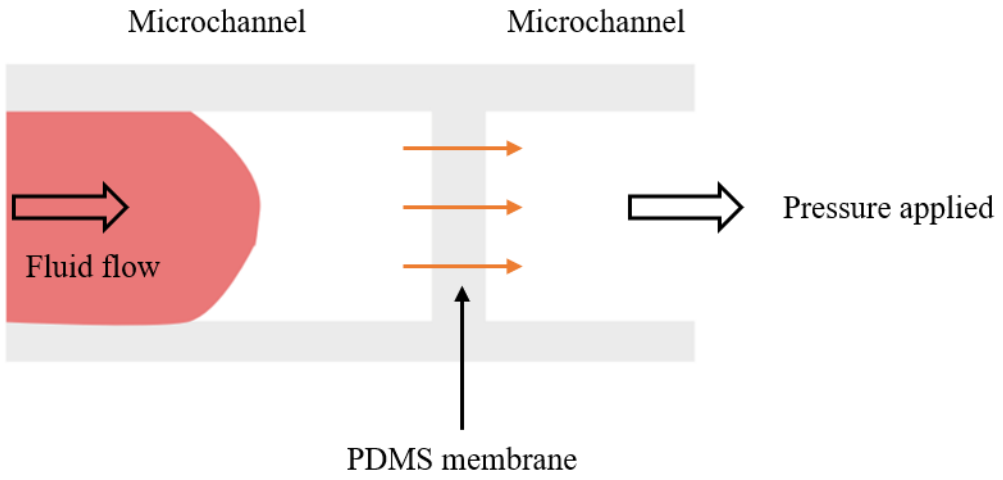

Figure 22. Air molecules passing through the PDMS membrane from the left to the right microchannel.

Materials and Experimental Method

Blood Sample and Infusion

Human whole blood samples (K2-EDTA anticoagulant, Zen-bio Inc.) were purchased and used in our microfluidic devices within 2 weeks of collection. For the plasma separation, whole blood was diluted 5× in Phosphate Buffered Saline (PBS) and a 10 µl drop of the diluted blood sample was placed on the inlet to introduce the blood sample into the microchannel by its negative internal pressure.

Images Analysis for the Flow Tracking and Cell Quantification

The fluid flow driven by the self-powered microfluidic devices was monitored and recorded using a CCD camera (8 MP CMOS sensor, SONY), and the fluid trajectory was analyzed by the Tracker software (Open-source physics). The concentration of blood cells in the whole blood sample and plasma obtained from our microfluidic devices was measured and analyzed by a hemocytometer, (Phase counting chamber, Hausser Scientific) and the ImageJ software (NIH), respectively. Plasma separation efficiency and cell quantification were performed after further dilution (600×) of both blood and plasma in PBS.

Hemolysis Measurements

Hemolysis in the samples was analyzed by absorbance spectrum analysis[78] (NanoDrop 2000 UV-Vis spectrophotometer, Thermo Fisher Scientific) to determine the plasma quality. Three samples were prepared and compared as follows: lysed blood using sonication (90 min, Cole-Parmer Ultrasonic Processors CPX 130); plasma obtained from the centrifugation of whole blood (1300 × g for 10 min, Eppendorf Microcentrifuge 5415R); and plasma obtained from the self-powered PDMS microfluidic devices.

3D Printer Mold and Mold Treatment

Silicon microfabrication processed molds are commonly used to fabricate microfluidic devices, providing the advantage of high resolution. However, the silicon microfabrication process has some disadvantages: it is expensive, time-consuming, and laborious[79]. Advanced 3D printer technology can print products with micron-scale resolution (Form 3, Formlabs). We fabricated microfluidic devices with the 3D-printed mold (Figure 23a and Figure 23b). The mold was designed using AutoCAD (Figure 23c), and the product from the 3D printer can be seen in Figure 23d.

Primitive 3D-printed molds can be problematic when used as molds for PDMS. The surface of PDMS, where it is attached to the mold, is not fully cured during the curing process. This phenomenon is due to the photoinitiator in the resin we used. The following surface treatment steps were taken to correct this problem:

- Immerse the 3D printed mold in deionized water for 2 hours.
- Cure it in the oven at 85 - 95°C for 18 hours.
- Remove the yellowish oily film that appears on the surface of the mold by washing with dish detergent and deionized water.

- Dry the mold.

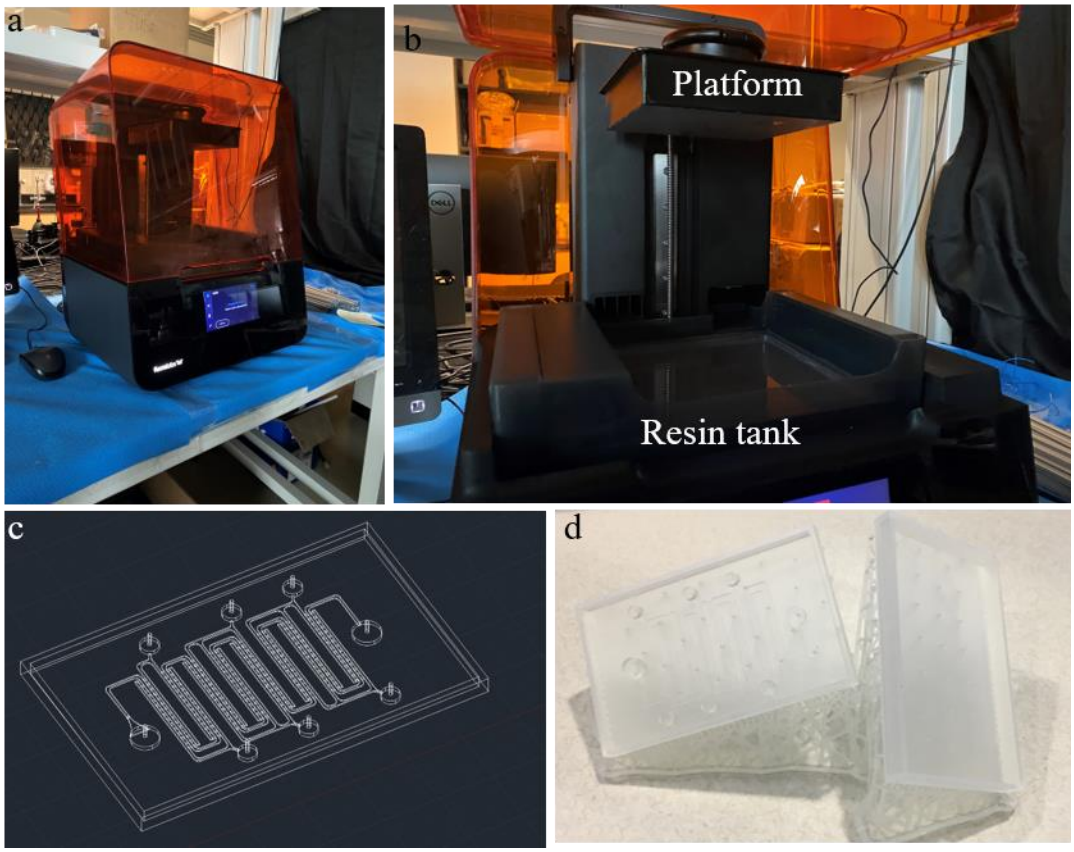

Figure 23. Process of 3D printed mold manufacturing. (a) Formlabs 3D printer. (b) The platform for 3D printed product and resin tank. (c) AutoCAD design; the dimensions of the device are 46mm × 76mm × 3.5mm, channel width: 0.6mm, channel height: 0.3mm, cliff height 0.05mm, channel length 254mm, inlet and outlet diameter: 6mm. (d) Product from the 3D printer.

Initial Device Fabrication

With the surface-treated mold, PDMS and curing agents are mixed at a 10:1 weight ratio. Many air bubbles can develop during mixing. The air bubbles in the PDMS mixture need to be removed because they can affect the PDMS gas permeability and absorption experiments, and the bubbles obscure observation inside the microchannel. A total mass of 13.5g of mixed PDMS and curing agents were poured into the mold and placed in a vacuum chamber to remove the air bubbles. While the PDMS mixture is in the vacuum chamber (100 kPa) for approximately thirty

minutes to 1 hour, air bubbles were removed from the mixture. After ensuring all air bubbles were removed, the mold was placed into the oven and cured at 75 - 80℃ for 1 hour.

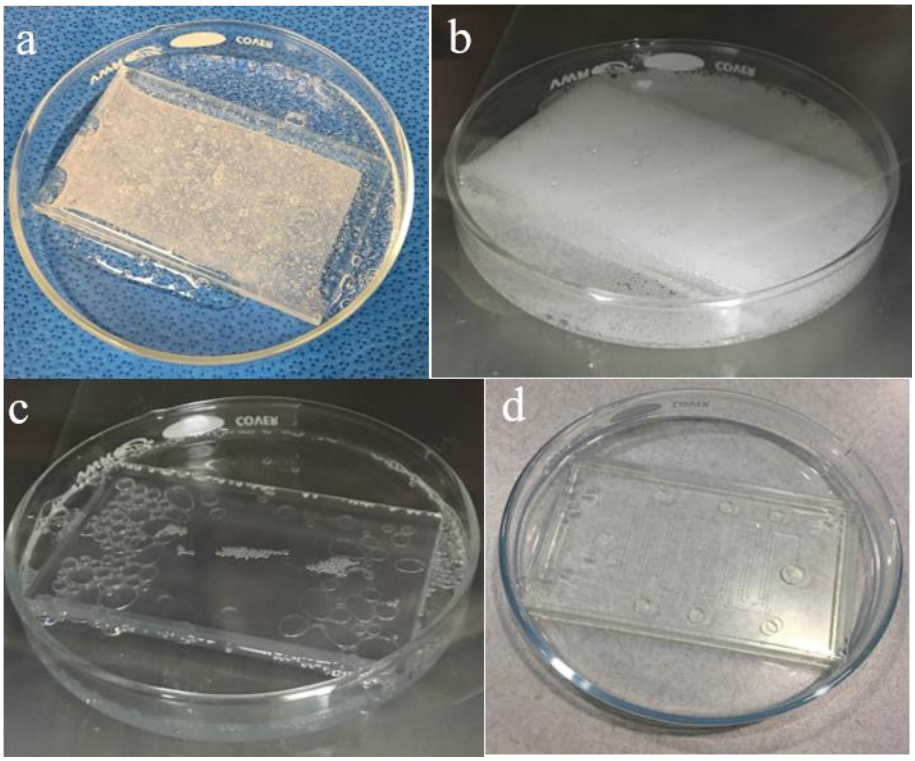

Figure 24. Process of removing air bubbles from PDMS. (a) 13.5g of mixed PDMS poured in 3D printed mold. (b) The mixed PDMS placed in the vacuum chamber (100kPa) and many air bubbles exited from PDMS. (c) Released the vacuum chamber by opening air valve and evacuated the chamber again (100kPa) to save bubble removal time. (d) Once all air bubbles removed, cured the PDMS in an oven at 75-80℃ for 1 hour.

Figure 25 (a) is a microscope image of a cured PDMS layer clearly patterned from a 3D printed mold. The device was designed to separate plasma using blood cells sedimentation with gravity; while the blood flows in the microchannel, only clear plasma can separately flow through the side channel (Figure 25 (b)).

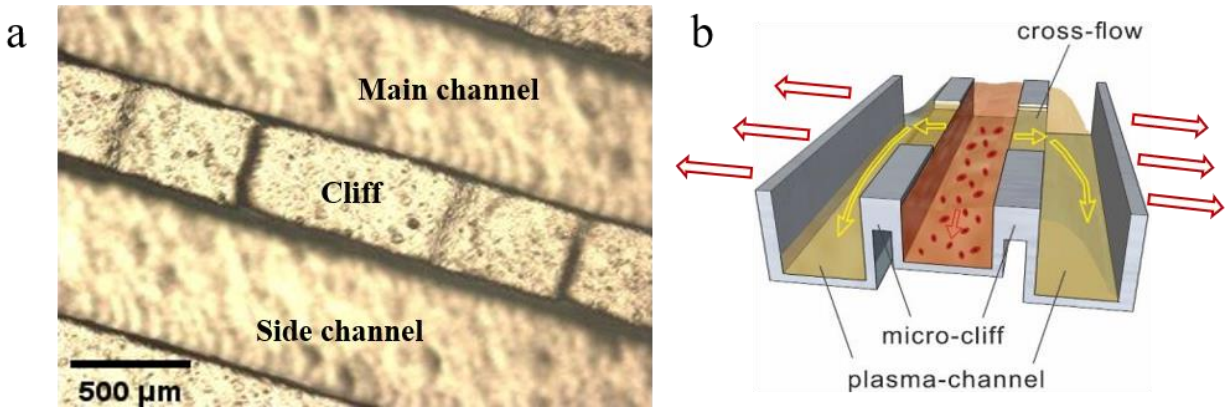

Figure 25. (a) Microscope image of cured PDMS surface. Main and side channel and cliffs for plasma separation were effectively patterned from the 3D printed mold. (b) Blood cells sedimented on the bottom of main channel while blood flows, only clear plasma over the cliff and separately flow the side channel.

3D printed mold for PDMS device

For the process of air bubble removal and curing PDMS (Figure 26), one empty Petri dish and 3D printed mold were prepared for the top and bottom PDMS layer, respectively. A 25:1 weight ratio of PDMS to curing agent was prepared for the top PDMS layer on an empty Petri dish and then heated in an oven for less than 1.25 hours to cure the partial PDMS layer. For the bottom PDMS layer, a 10:1 weight ratio of PDMS and the curing agent were mixed and then cured in a surface treated 3D printed mold. After both PDMS layers were partially and fully cured, they were carefully peeled off and assembled [80].

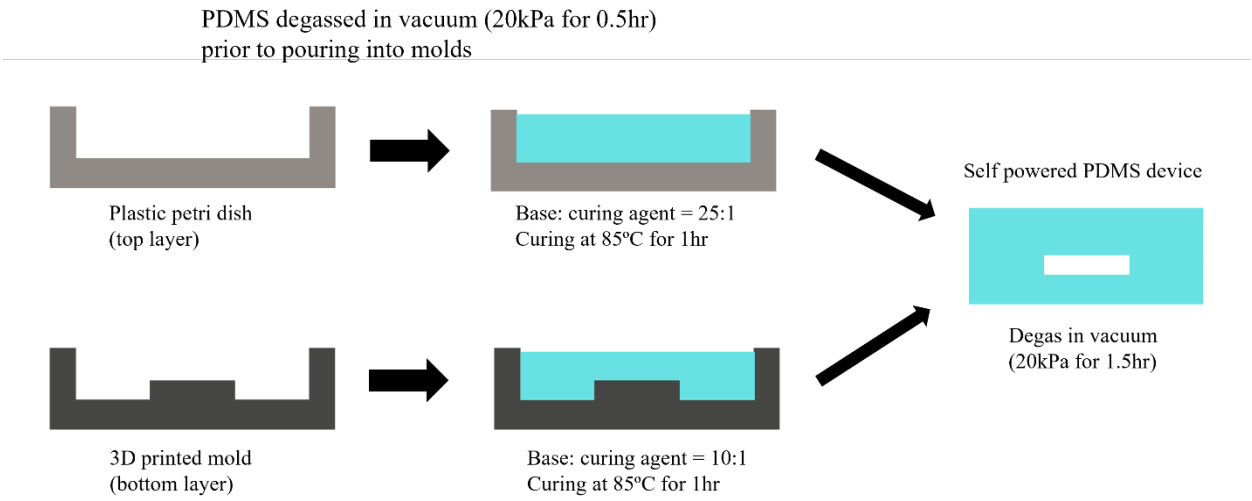

Figure 26. Device fabrication by using two different cured PDMS layers. The top layer should be partially cured, and the bottom layer should be fully cured.

Figure 27a shows excellent attachment between the two layers of the transparent PDMS device. However, if the top PDMS layer is fully cured, the top and bottom of the PDMS do not attach well, which results in issues with leaking fluid while the device is in operation. A hazy area can be seen between two PDMS layers, which are not well attached (Figure 27b and 27c). Figure 27d shows no leaking fluid issue from a well-connected PDMS device while fluid flows in microfluidic channels.

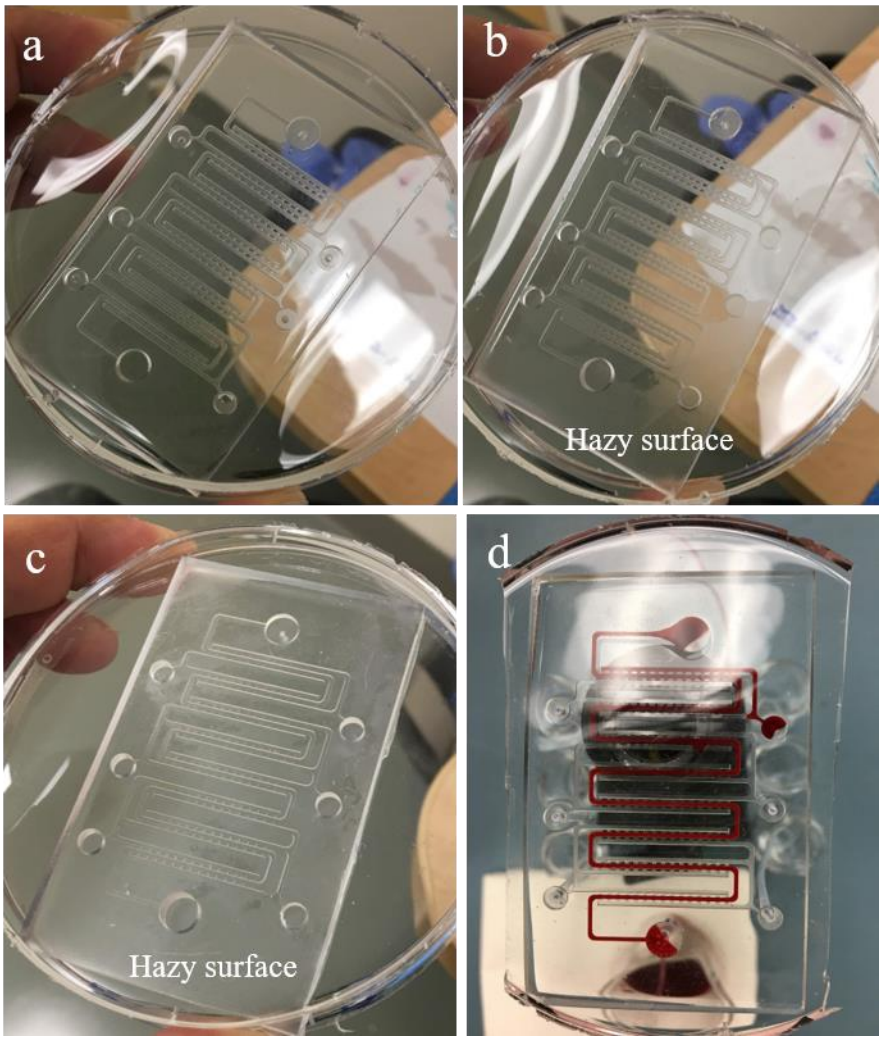

Figure 27. PDMS device. The dimensions of the device are 46mm × 76mm × 3.5mm, channel width: 0.6mm, channel height, 0.3mm, cliff height: 0.05mm, channel length: 254mm, inlet and outlet diameter: 6mm. (a) Good attachment between two PDMS layers (1.25 hours). Inadequate attachment (b and c) between two PDMS layers (1.5 and 2 hours). (d) No fluid leaking was observed between the two well-attached PDMS layers.

Operation of the microfluidic device

A simple linear device design was prepared to demonstrate plasma separation (Figure 28a). Blood cells are supposed to sediment while blood flows, so only plasma flows over the cliff and into the side channel in Figure 28b. We designed the depth of both the main and side channel to be 500µm, and the height of the cliff is 450µm, so plasma passes through the 50µm gap. We infused the blood using a syringe pump at 1µl/min, and no leaking between the top and bottom

of the PDMS was observed. However, we could not see plasma separation on the side channel in our initial device design. Only a small amount of blood flowed over the cliffs, and most blood flowed through the main channel. This movement occurred likely because of the surface tension of the blood; the inter-molecular attraction of liquid molecules inside the fluid in the main channel is greater than the interaction between the fluid and PDMS surface.

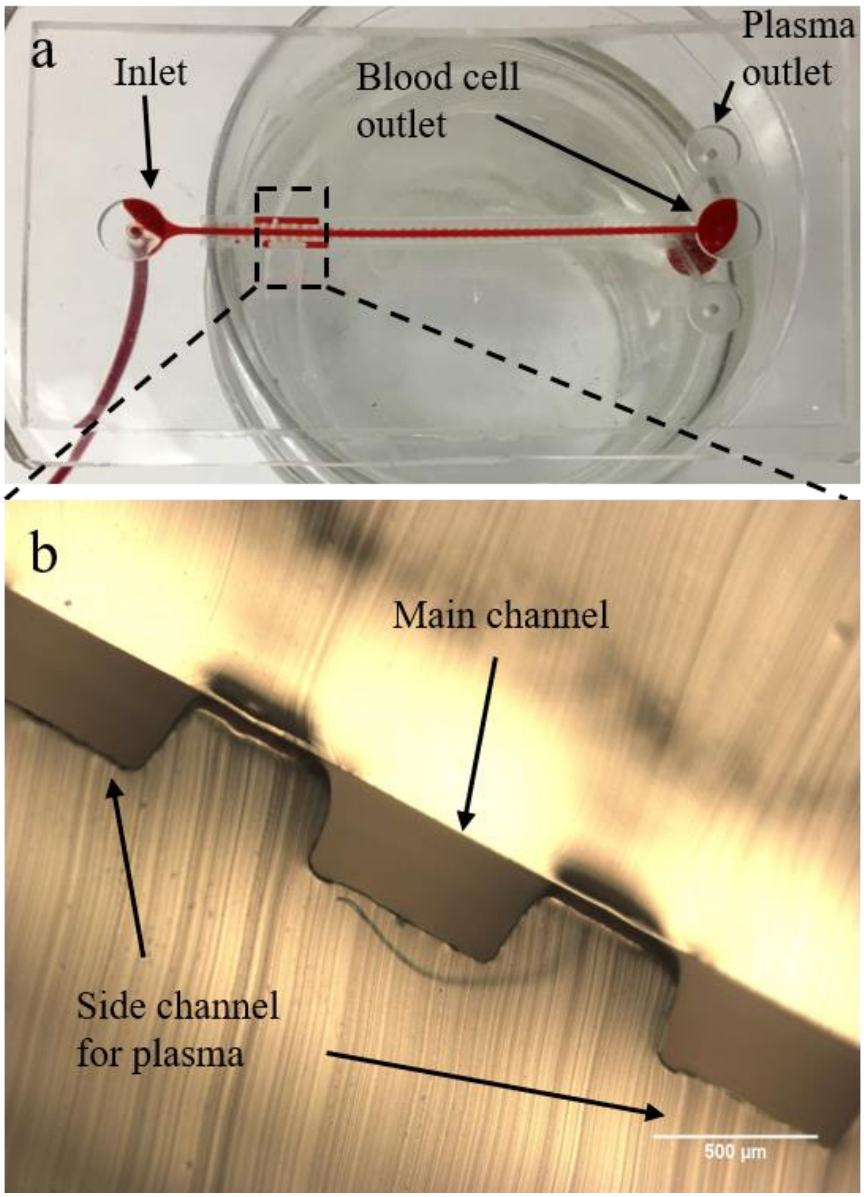

Figure 28. Demonstration of the initial linear design. (a) Linear device design. 1µl/min of blood was injected into the inlet by the syringe pump. No separated plasma can be seen on the side channel. The dimensions of the device are 16mm × 61mm × 3m, channel width: 0.6mm, channel height: 0.3mm, cliff height: 0.05mm, channel length: 50mm, inlet and outlet diameter: 2.5mm. (b) Microscope image of cross-section view of main and side channel of the device. The gap between the main and side channel is obvious.

Another design provided a different cliff depth, and the syringe pump was connected to the side channel to absorb air molecules at the same flow rate as blood infusion from the inlet, leading to low pressure inside the side channel. This design would allow plasma to flow on the

side channel over the cliffs. The gap increased by lowering the cliff height (100µm, 200µm, and 300µm; Figure 29). It was observed that fluid flowed more easily with a bigger gap (Figure 30).

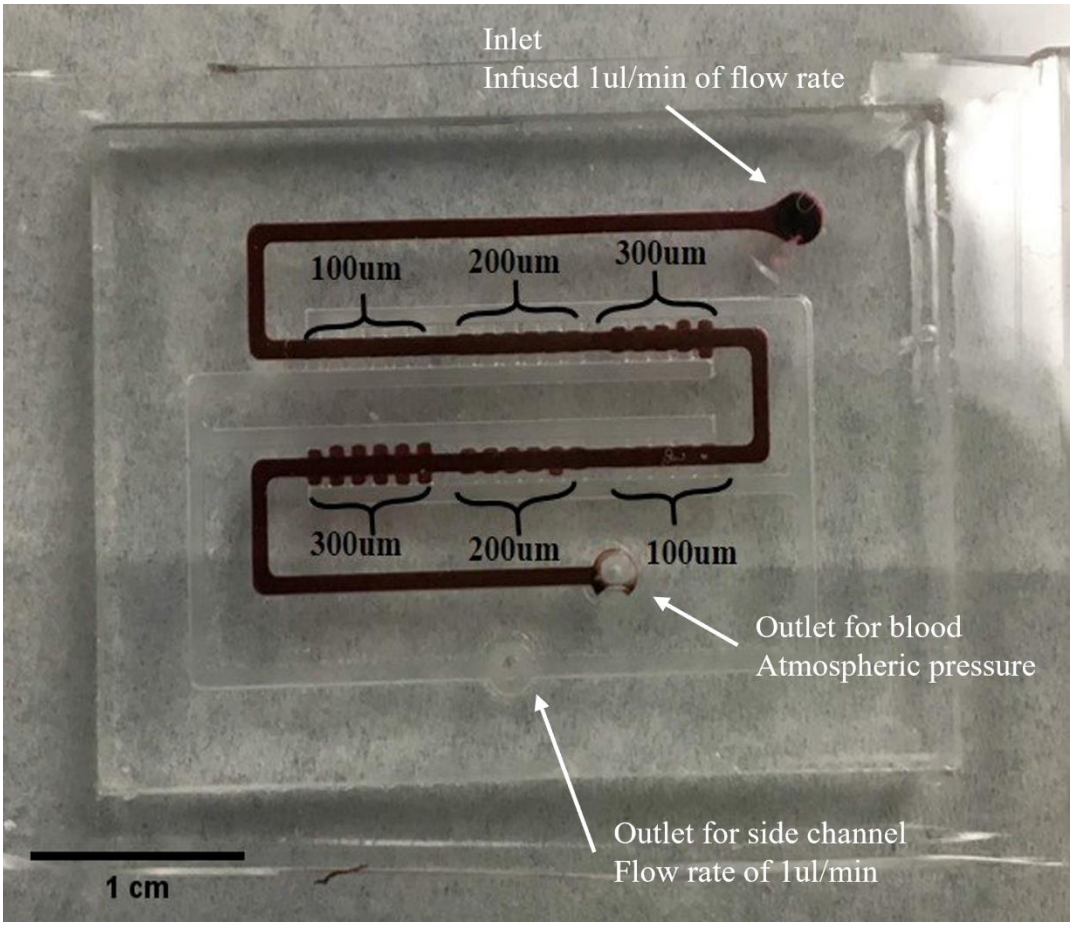

Figure 29. Blood flow over gaps of different heights. As the gap increased from 100µm to 300µm, more blood could flow over cliffs. The dimensions of the device are 26mm × 39mm × 3mm, channel width: 0.6mm, channel height: 0.5mm, cliff height: 0.1mm, 0.2mm, and 0.3mm, channel length: 47mm, inlet and outlet diameter: 2mm.

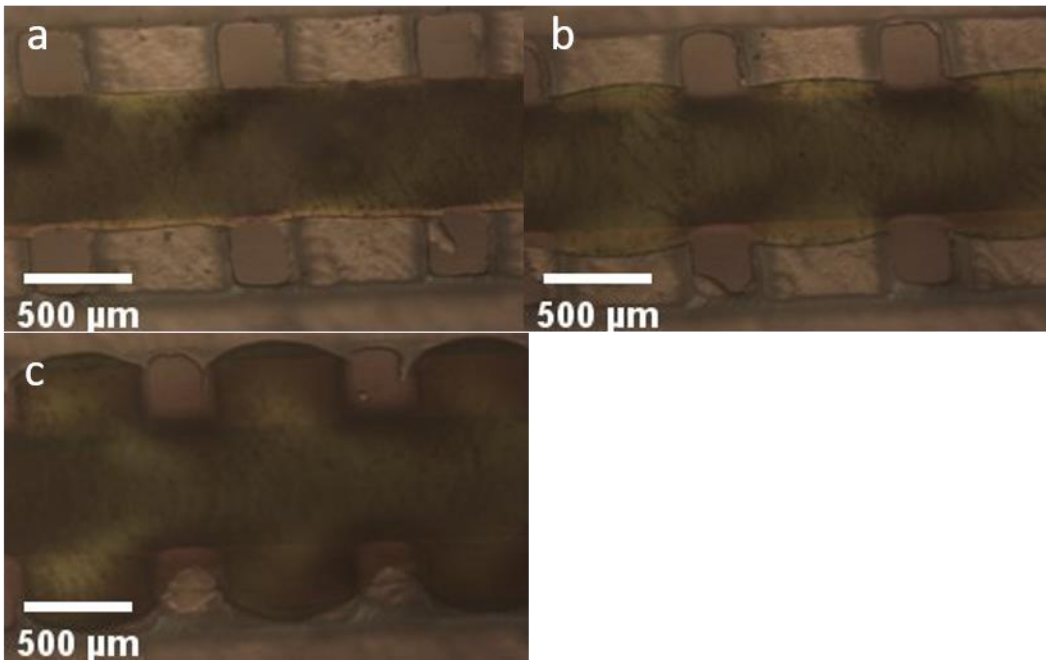

Figure 30. Microscope images of different gap heights. It is possible to see more blood on the cliffs as the gap increases. (a) 100µm, (b) 200µm, and (c) 300µm.

Hydrophobicity and hydrophilicity of PDMS

Pristine PDMS is a hydrophobic material [81]–[83]. PDMS is widely used as a material for droplet-based microfluidic devices, which is a process or manipulation of a small amount of fluid in a micro- or nano-size of channel [84]. PDMS with hydrophilicity helps to wet the device surface effectively. Many researchers have attempted to change the hydrophobicity of PDMS to hydrophilicity using oxygen plasma and ultraviolet/ozone treatment (UVO) [85], polymer coating with chemical vapor deposition [86], sol-gel chemistry [87], polyelectrolyte layer-by-layer deposition [88], and other methods. We changed the hydrophobicity of PDMS to hydrophilicity with UVO treatment (Model No 42A, Jelight Company Inc.) by exposing the PDMS surface to a UV lamp in the instrument for at least thirty minutes. The average intensity of UV light is 28 ~ 32 mW/cm^2. The difference can be seen between non-treated PDMS and the UVO-treated PDMS surface. Figure 31 shows a dropped water shape on the UVO-treated PDMS

(hydrophilic) and non-treated PDMS (hydrophobic). After the UVO treatment, the surface of PDMS changes to hydrophilicity, so the shape of the droplet water looks spread out. This is because the attractive interaction between water molecules is smaller than the interaction between water molecules and the PDMS surface. Without the UVO treatment, the droplet of water is dome-shaped since the attractive interaction between water molecules is stronger than the interaction between water molecules and the PDMS surface.

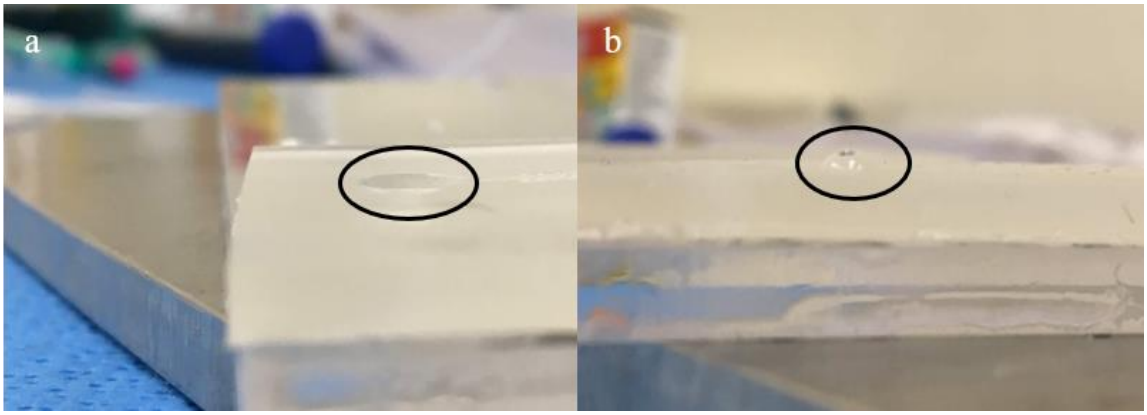

Figure 31. Different droplet water shape on (a) hydrophilic PDMS with UVO treatment and (b) hydrophobic PDMS without UVO treatment.

Moreover, cracks can be seen on the PDMS surface as UVO treatment time increases, which could be an issue of being used in microfluidic device (Figure 32). Microfluidic devices manage small (10^{-9} - 10^{-18} L) amounts of fluids in a small (10^{-6} – 100^{-6} meters) channel[84]. Cracks on the surface of device could be a severe issue, allowing water to leak while the device is in operation.

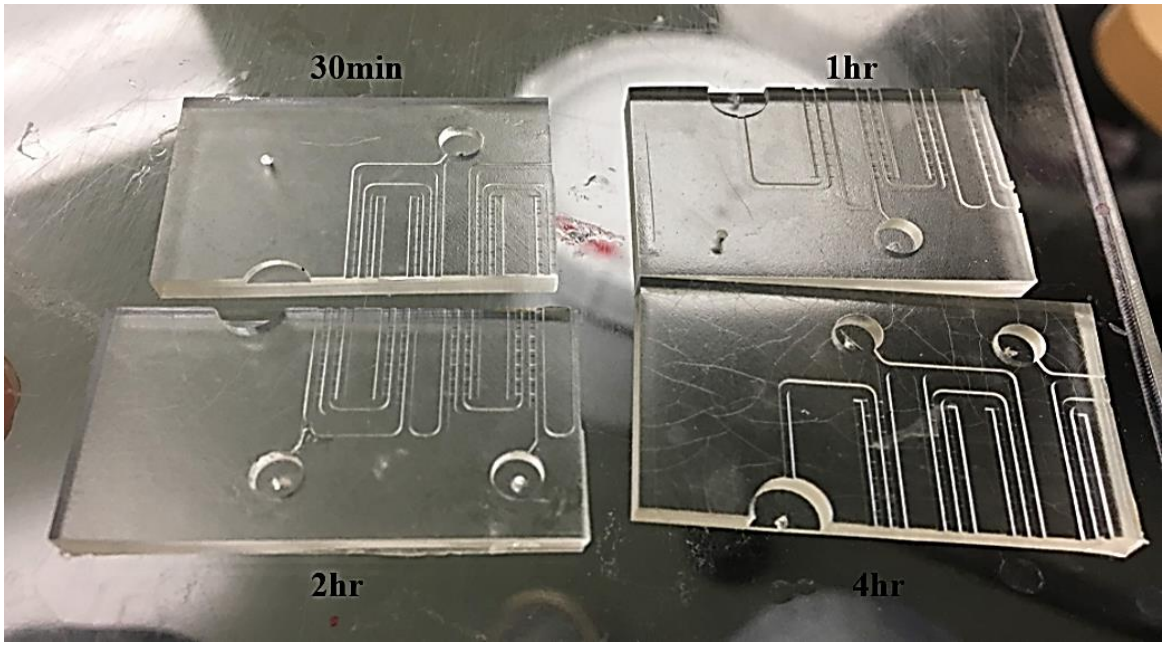

Figure 32. Cracks can be seen as the UVO treatment time on the PDMS surface increases.

Fluid flow with degassed PDMS device

The cell separation with sedimentation technique was attempted using the device by infusing fresh blood using a syringe pump at a flow rate of 1µl/min. We observed clear plasma being collected at the outlet of the device (Figure 33a). However, there was a problem with infusing homogenized blood into the device. Blood cells were sedimented in the tube and syringe while the blood was infusing into the device because the blood flow was too slow (Figure 33b and Figure 33c). Tuning the blood flow rate or blood infusing system is required to separate plasma from blood in the microfluidic channel. To solve the issue, we replaced the blood infusing system from the syringe pump with the PDMS gas absorption on our device [89]–[91]. This replacement prevented blood cell sedimentation on the bottom of the tube and the complicated tubing system on the device. Moreover, we did not need an external force to infuse blood into the device. This technique is promising for use in future portable devices.

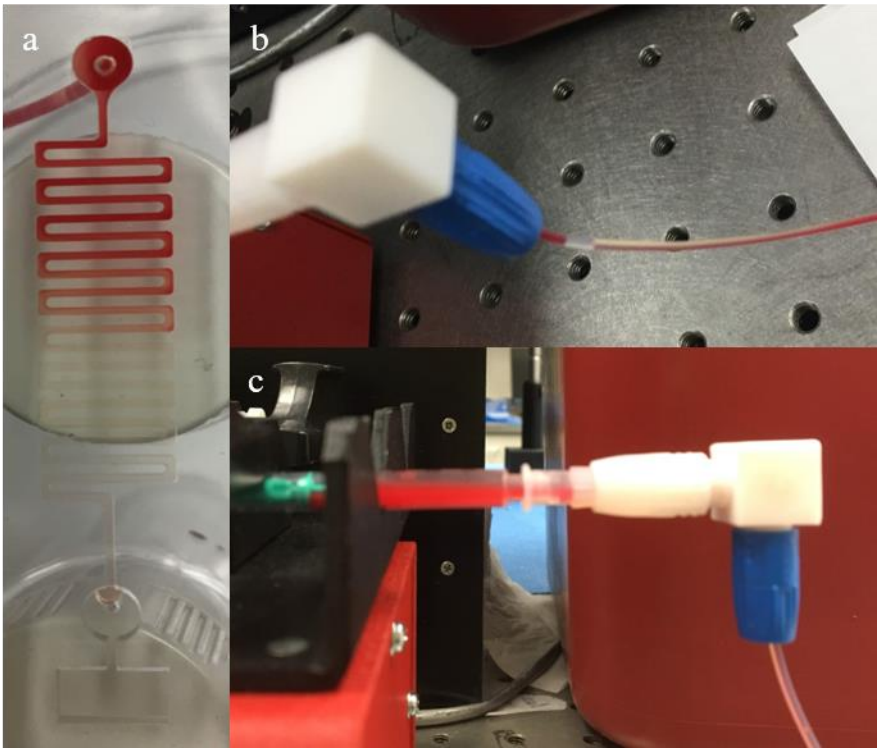

Figure 33. A plasma separation experiment using a syringe pump. (a) Successfully separated plasma in device. The dimensions of the device are 19mm × 61mm × 3m, channel width: 0.6mm, channel height: 0.5mm, channel length: 171mm, inlet and outlet diameter: 4mm, vacuum void size: 7.5mm × 4mm × 1.5mm. (b) and (c) Issues of blood cell sedimentation in the syringe pump and the tube while the device is in operation.

The PDMS fabricated device was placed in a vacuum chamber for the degassing process and air molecules escaped from the PDMS. Then we removed the device from the vacuum chamber and dropped blood onto the inlet of the microfluidic channel. The blood flowed without any external forces applied. We collected clear plasma from both outlet and side channels of the device (Figure 34).

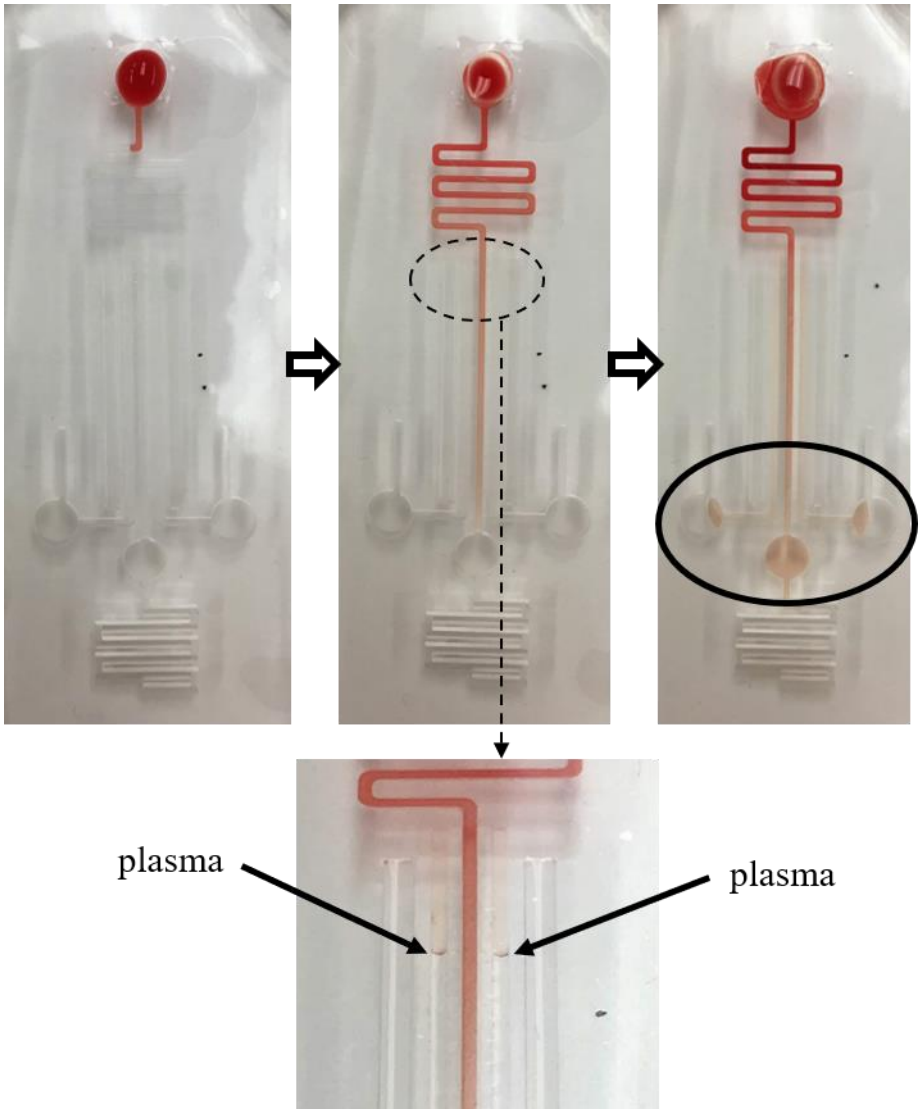

Figure 34. Plasma separation using PDMS absorption. Plasma was observed in the microfluidic channel after approximately two hours. The device dimensions are 73mm × 30mm × 3mm, channel width: 0.6mm, channel height: 0.5mm, channel length: 70mm, inlet and outlet diameter: 4mm.

Degassed vacuum pocket assisted plasma separation

Plasma separation with only PDMS gas absorption requires approximately two hours. We applied both PDMS gas absorption and permeability by adding a separated vacuum void inside the device to shorten the blood flow time. Several interdigitated microchannels were created, one set of channels was connected to an outlet, and another was connected to the vacuum void. As a result, air molecules were able to pass through the PDMS membrane (lung pairs). The following

parameters of the device were varied for optimization: lung pairs, the volume of vacuum void, and degassing pressure. (Figure 35).

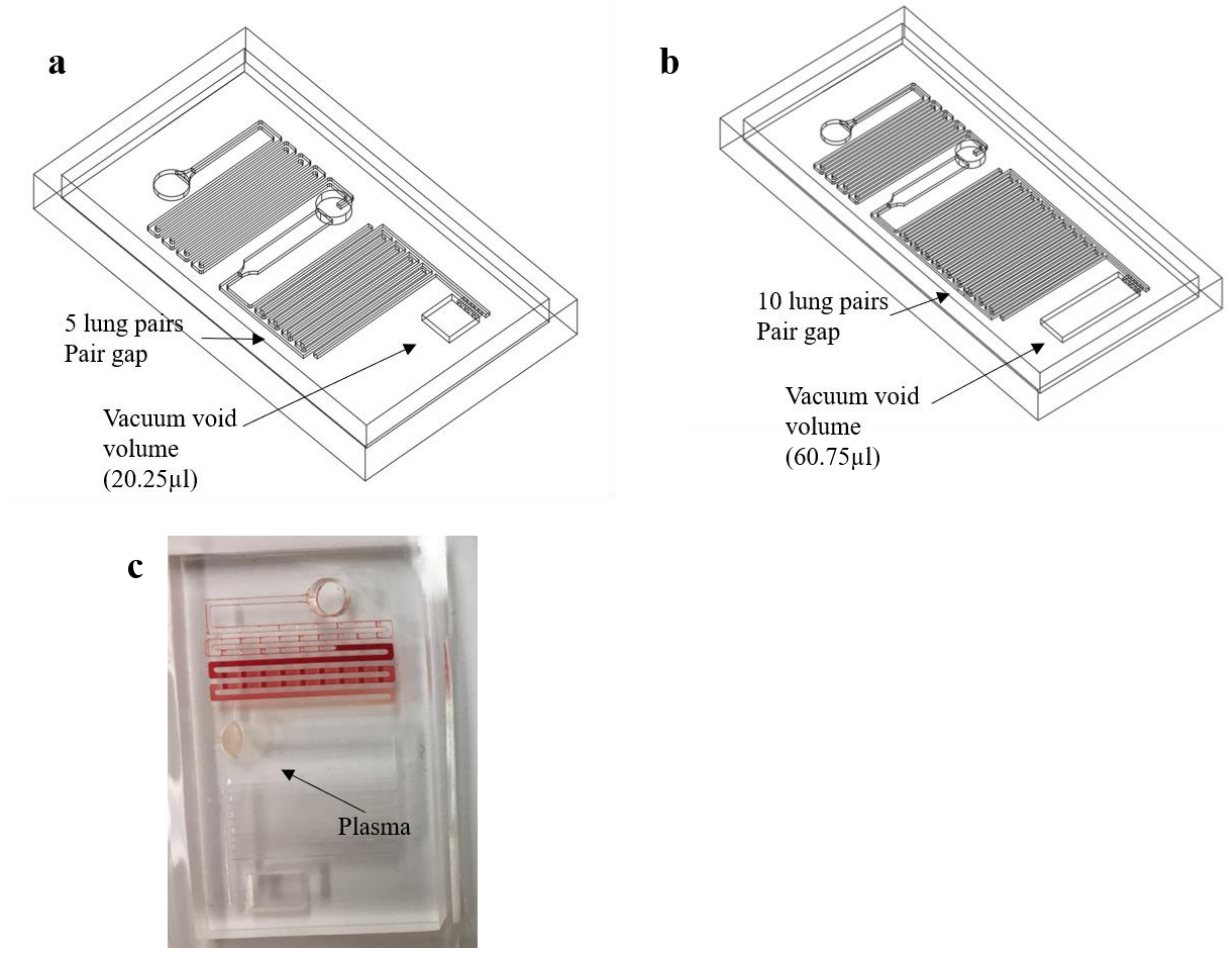

Figure 35. A device using both PDMS gas absorption and permeability. (a) AutoCAD design for 5 lung pairs and 20.25µl vacuum void volume. (b) AutoCAD design for 10 lung pairs and 60.75µl vacuum void volume. (c) Experiment result of plasma collection. Device dimension, 50mm × 30mm × 3mm; channel width: 0.6mm; channel height: 0.5mm; channel length 177mm; inlet and outlet diameter: 4mm; lung pair channel width: 0.6mm, lung pair channel height: 0.5mm, lung pair channel length: 85mm.

Figure 36 shows the experimental flow rate results obtained by varying specific parameters. The number of lung pairs, degassing pressure in a vacuum chamber, and volume of vacuum void were changed to see how they affect the flow rate. As the number of lung pairs increased, the flow rate increased since the gas-permeable surface area of PDMS increased. For the same number of lung pairs, the flow rate was increased as degassing pressure in the vacuum

chamber was increased. This result was due to more air molecules in both the PDMS and vacuum void leaving while devices were in the vacuum chamber. The flow rate increased as the volume of the vacuum void increased, but as both PDMS gas absorption and permeability were exploited for this device, it is difficult to say which characteristic of PDMS affected the flow rate. Further experimentation is recommended to test only the effects of PDMS gas permeability. We replaced the top PDMS layer with an acrylic plate and compared the non-vacuum void and existing vacuum void devices. Detailed device fabrication, experimental method and results will be discussed.

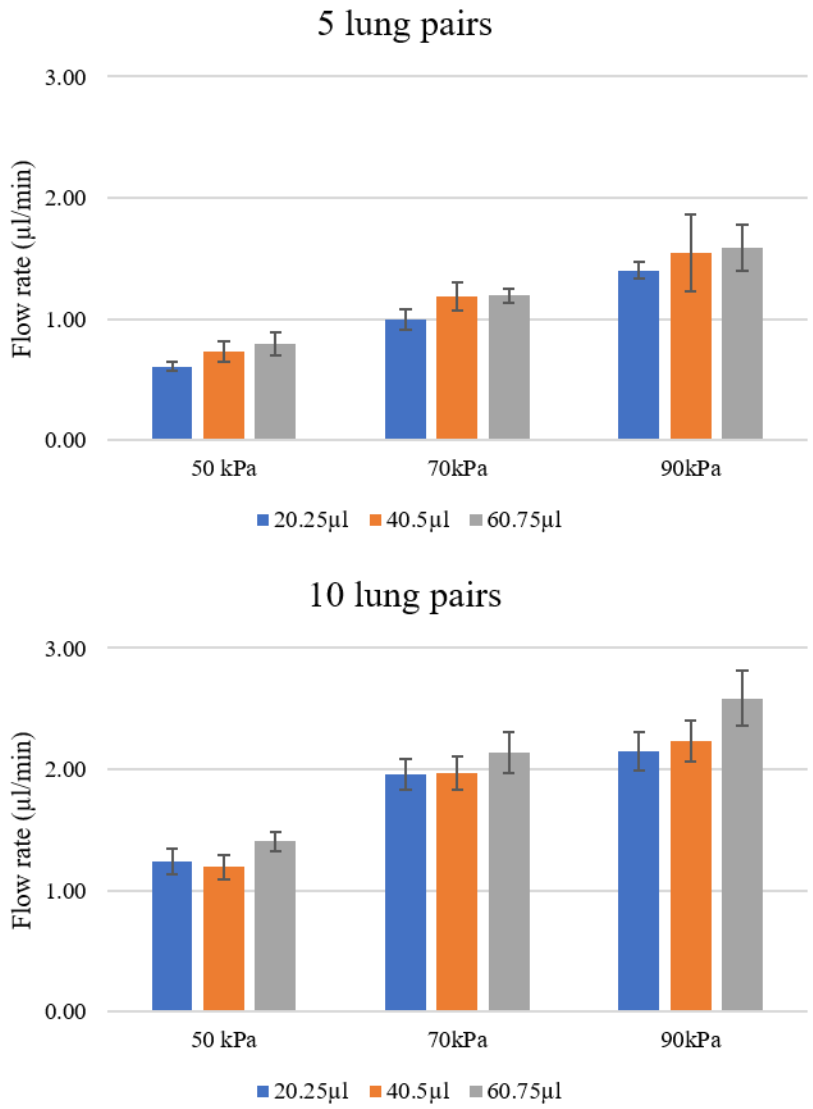

Figure 36. Experimental result after changing several parameters: number of lung pairs (5 lung pairs and 10 lung pairs), the volume of vacuum void (20.25µl, 40.5µl, and 60.75µl), and degassing pressure (50kPa, 70kPa, and 90kPa) in vacuum chamber. The flow rate increased as the number of lung pairs increased and degassing pressure increased.

Final Device Fabrication

PDMS covered by plastic device

The self-powered microfluidic PDMS devices were fabricated via the standard soft lithography technique using PDMS (Sylgard 184, Dow Corning, USA). A mixture of PDMS and a curing agent with a ratio of 10:1 was degassed in a vacuum chamber (Fisher Scientific, USA)

at 20 kPa for 0.5 h. Then, the mixture was poured into a 3D printed mold (Formlabs Inc., USA), and further degassed in the vacuum chamber at 20 kPa for 0.5 h. After such degassing processes at room temperature, the temperature was elevated to 85°C to cure the mixture in the chamber for 1 hr, followed by cooling down to room temperature and careful peeling off the PDMS device from the mold [79], [92]. The PDMS device cover was air-tight, using either a transparent acrylic plate with a housing assembly (Figure 37) or a thin PDMS layer (Figure 38). Finally, the covered PDMS devices were placed in the vacuum chamber at 20 kPa for 1.5 h to degas the air molecules trapped in a vacuum pocket. The minimum thickness δ of 500 µm between the microchannel and vacuum pocket was used in the device to prevent the PDMS partition from collapse during the degassing process under the low vacuum condition. As soon as the PDMS devices were taken out of the chamber, the test fluids were dropped into the inlet and the fluid traces were recorded by a video camera.

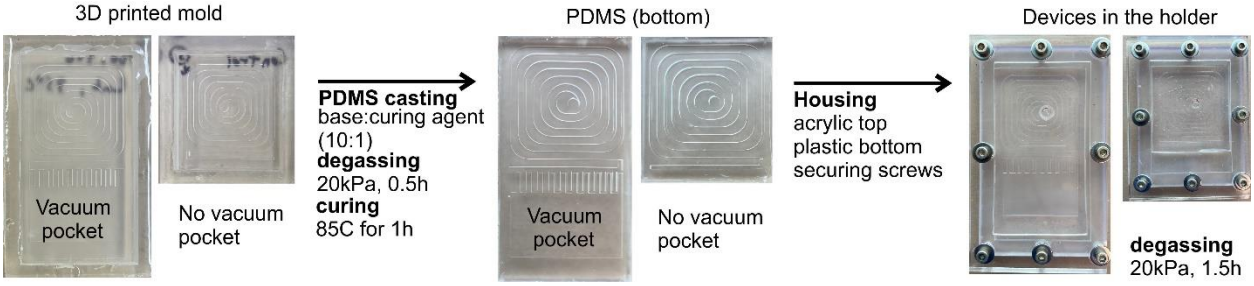

Figure 37. The device fabrication process of the self-powered, PDMS microfluidic devices with a device holder. Two identical devices except a vacuum pocket were prepared by the same method. The final PDMS devices were securely sealed with a top acrylic plate using a screw mechanism.

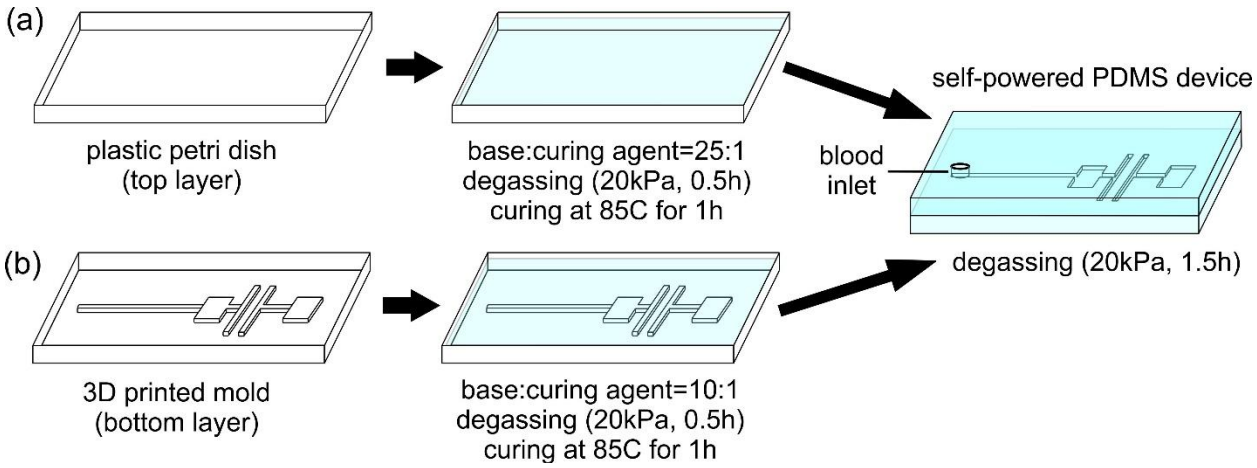

Figure 38. The device fabrication process of the self-powered, PDMS microfluidic devices without the device holder. (a) A plastic petri dish used as a mold for the top PDMS piece. (b) A 3D printed mold including microchannel and the vacuum pocket for the bottom PDMS piece. After curing each piece, the final device was fabricated by attaching two pieces carefully and degassing it in the vacuum chamber.

Results and Discussion

Fluid Dynamics and Molecular Diffusion Model of the Self-powered Microfluidic Devices

Figure 39a illustrates the self-powered PDMS microfluidic device consisting of fluid inlet, microchannel, and vacuum pocket, where the interfacial area *A* between the microchannel and the vacuum pocket, and volume of vacuum pocket *V* are two geometrical parameters. When a drop of fluid such as whole blood is placed into the inlet, the fluid seals the inlet and lowers internal pressure in the microchannel, which pulls blood from the inlet to the vacuum pocket. Figure 39b and 39c demonstrate typical trajectories of the fluid in the microchannel recorded as a function of time using various devices with different vacuum pocket parameters. The distance of fluid traveled in the microchannel from the inlet increased with time and fit well to an exponential form $d \sim d_0(1 - e^{-t/\tau})$ (black curves), where t and τ are total traveling time and characteristic time, respectively. The flow rate became faster when either *A* increased at fixed *V* (Figure 39b) or *V* decreased at fixed *A* (Figure 39c). Compared to *V*, the effect on the flow rate by changing in *A* was significant. In any case, the changes in two parameters of the built-in

vacuum pocket enabled control of the overall fluid flow in the devices. This observation indicates that fluid flow is governed by a simple diffusion mechanism of air molecules in the PDMS device[57], [91].

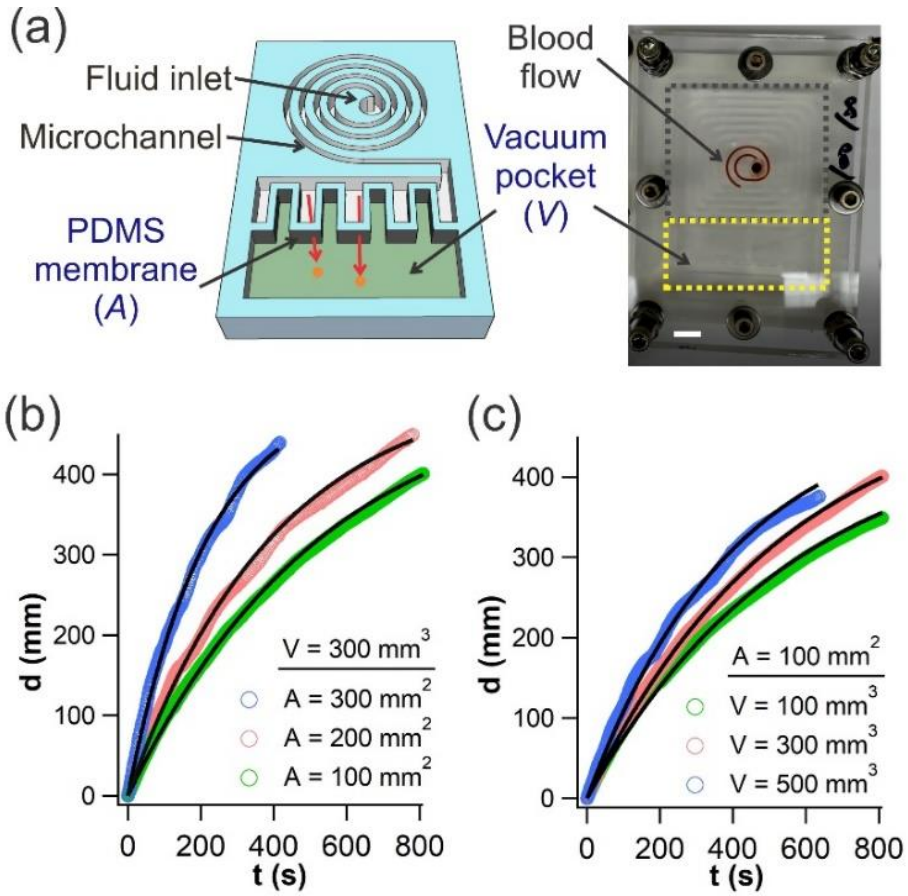

Figure 39. The self-powered, PDMS microfluidic device. (a) The schematic depicts two geometrical parameters, *A* and *V*, of the vacuum pocket, and the diffusion of air molecules from the microchannel to the vacuum pocket through the PDMS membrane. The scale bar is 5 mm. Fluid trajectories of the devices with (b) different *A* at fixed *V* and (c) different *V* at fixed *A* and their exponential fit to $d \sim d_0(1 - e^{-t/\tau})$.

To precisely determine the effects of *V* and *A* on the fluid dynamics of our PDMs devices, we derived an analytic expression of the fluid trajectory, based on a molecular diffusion model. In the model, the fluid is driven by the pressure difference ($\Delta P = P_{atmosphere} - P_1$) between the atmosphere and microchannel (Figure 40), where P_1 is the pressure in the microchannel enclosed by fluid and PDMS. The vacuum pocket keeps P_1 less than $P_{atmosphere}$ by diffusing air molecules

from the microchannel to the pocket. Therefore, the operational principle of the device with the built-in vacuum pocket is pressure-induced molecular diffusion through the PDMS membrane.

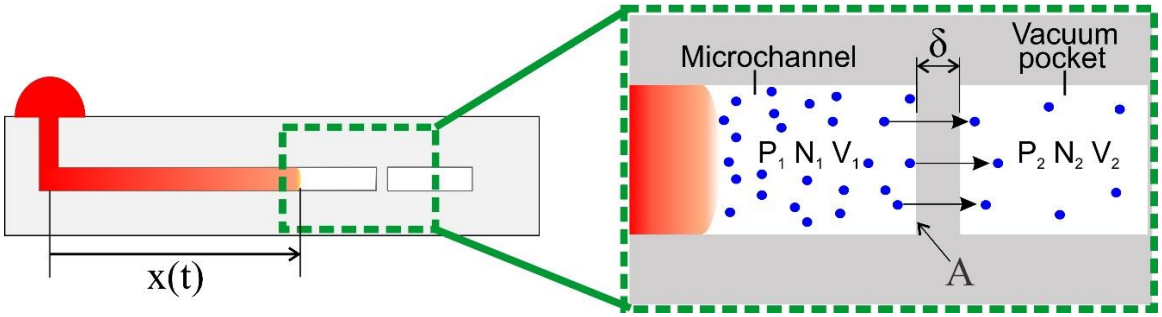

Figure 40. The molecular diffusion model of the fluid flow in the microchannel. *P*, *V*, *N*, *δ*, *A*, and *x*(*t*) represent pressure, volume, total number of molecules, thickness, surface area of thin PDMS partition, and the distance of the fluid advanced from the inlet as a function of time, respectively. Subscription 1 and 2 denote the microchannel and the vacuum pocket, respectively.

We start from Fick's law to derive the trajectory of the fluid driven by the vacuum pocket [93]. In this model, we consider air molecules that diffuse through the PDMS membrane between the microchannel and the vacuum pocket and ignore the finite diffusion through the bulk PDMS surrounding the microchannel. The rate of change in the number of molecules in the vacuum pocket is given by

$$\frac{\Delta N_2}{\Delta t} = AJ, \tag{1}$$

where $J = -D\frac{\partial \varphi}{\partial x}$ is the flux of air molecules through the PDMS membrane. Plugging Eq. (1) with $\frac{\partial \varphi}{\partial x} = \frac{\varphi_2 - \varphi_1}{\delta}$ and $\varphi = \frac{N}{V} = \frac{P}{k_B T}$, the time dependent pressure in the vacuum pocket is described by

$$\frac{dP_2}{dt} = \tau^{-1}(P_1 - P_2). \tag{2}$$

Here, D and φ indicate the diffusion constant of PDMS and air molecular concentration, respectively. Then, τ can be expressed by the geometric parameters of the vacuum pocket,

$$\tau^{-1} = \frac{A \cdot D}{\delta \cdot V_2}. \quad (3)$$

By applying a boundary condition, P2 (t = 0) = P2,0, Eq. (2) can be rewritten,

$$P_2(t) = P_1 + \left(P_{2,0} - P_1\right)e^{-t/\tau}, \quad (4)$$

where P2,0 is the pressure of the vacuum pocket when the fluid is placed in the inlet.

The rate of change in the number of air molecules in the microchannel and the vacuum pocket is given by $\frac{dN_1}{dt} = -\frac{dN_2}{dt}$, and the total number of air molecules in each volume is defined by the ideal gas law, $N = \frac{PV}{k_B T}$, where k_B and T are the Boltzmann constant and temperature, respectively[93]. By combining these two relations and assuming a slow diffusion process, the rate of volume change in the microchannel can be written as

$$\frac{dV_1}{dt} = -\frac{V_2}{P_1}\frac{dP_2}{dt}. \quad (5)$$

Substituting Eq. (4) into Eq. (5) yields $\frac{dV_1}{dt} = \frac{V_2}{\tau}\left(\frac{P_{2,0}}{P_1} - 1\right)e^{-t/\tau}$. Since V1 decreases as the fluid advances in the microchannel, the velocity of fluid $\frac{dx}{dt} = -\frac{1}{A_{ch}}\frac{dV_1}{dt}$ becomes

$$v(t) = v_0 e^{-t/\tau}, \quad (6)$$

where $v_0 = \frac{V_2}{\tau A_{ch}}\left(1 - \frac{P_{2,0}}{P_1}\right)$ is the initial velocity of fluid, and Ach is the cross sectional area of the microchannel. Integrating on both sides of Eq. (6) gives

$$x(t) = x_0\left(1 - e^{-t/\tau}\right), \quad (7)$$

where $x_0 = \tau v_0$ is a terminal distance which is determined by the geometry of the PDMS devices.

Validation of the Molecular Diffusion Model

To evaluate whether our model agrees with experimental observation, all fluid trajectories of the devices (Figure 39) were initially converted to velocity, which is inappropriate to compare with the model and Eq. (6) because it includes the non-negligible bulk PDMS

contributions. However, careful subtraction of velocity data sets with and without the vacuum pocket in the devices allowed us to eliminate the finite contributions of the bulk PDMS and determine the correlation between the fluid dynamics and vacuum pocket parameters. This subtraction was carried out by fitting raw data obtained from two identical devices except the vacuum pocket (Figure 37). The resultant velocity $v(t)$ displayed in Figure 41 corresponds to the pure contribution of the vacuum pocket to the fluid flow driven by the diffusion of air molecules through the PDMS membrane described in the molecular diffusion model. When either A increased at fixed V or V decreased at fixed A, the initial $v(t=0)$ increased, but $v(t)$ decreased rapidly with increasing time. However, all $v(t)$ curves fit well with Eq. (6), indicating excellent agreement between the model and experimental results.

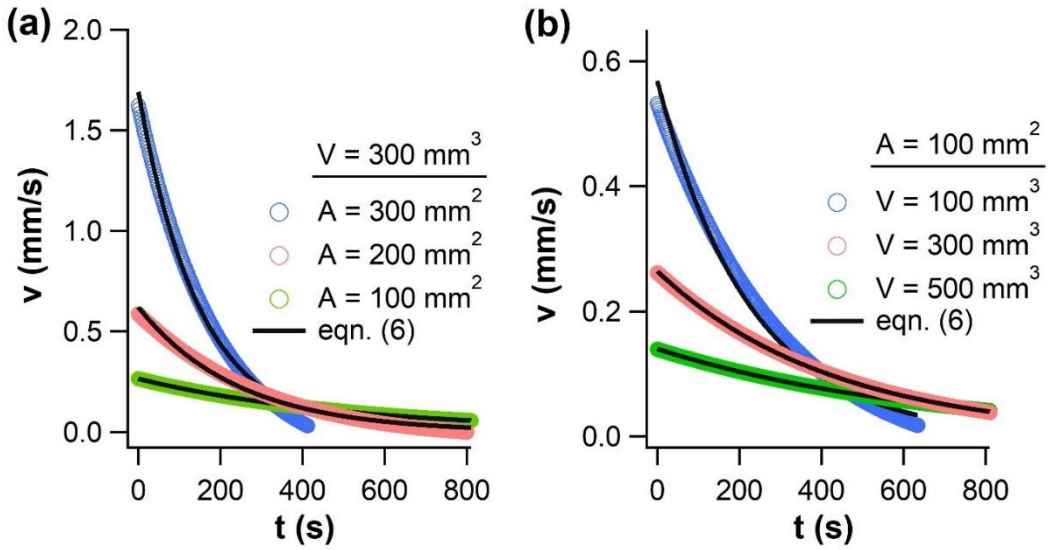

Figure 41. The fluid velocity acquired from various vacuum pocket geometry at either fixed (a) V or (b) A, plotted versus time. The black curves indicate fits to the molecular diffusion model described in the text.

Thus, two important physical parameters associated with fluid trajectory including τ and $P_{2,0}$ and their relationship with V and A could be calculated from the fit and Eq. (6). Figure 42a displays τ dependence on A at a V_2 = 300 mm^3 obtained from the fit of data to Eq. (6). As

predicted by Eq. (3), τ was inversely proportional to A, indicating that the total flux of air molecules diffusing from the microchannel to vacuum pocket increases with large diffusion cross-sectional area of the PDMS membrane. During the degassing process of the PDMS devices, the reversed direction of diffusion occurs: air molecules diffuse from the vacuum pocket into the atmosphere through the microchannel, lowering the initial pressure $P_{2,0}$ in the vacuum pocket. Like τ, the total diffusion of air molecules through A determines $P_{2,0}$ and leads to a significant decrease of $P_{2,0}$ with increasing A (Figure 42a inset). Therefore, the increased pressure difference between $P_{atmosphere}$ and $P_{2,0}$ further accelerates the fluid flow in the microchannel, resulting in the decrease of τ.

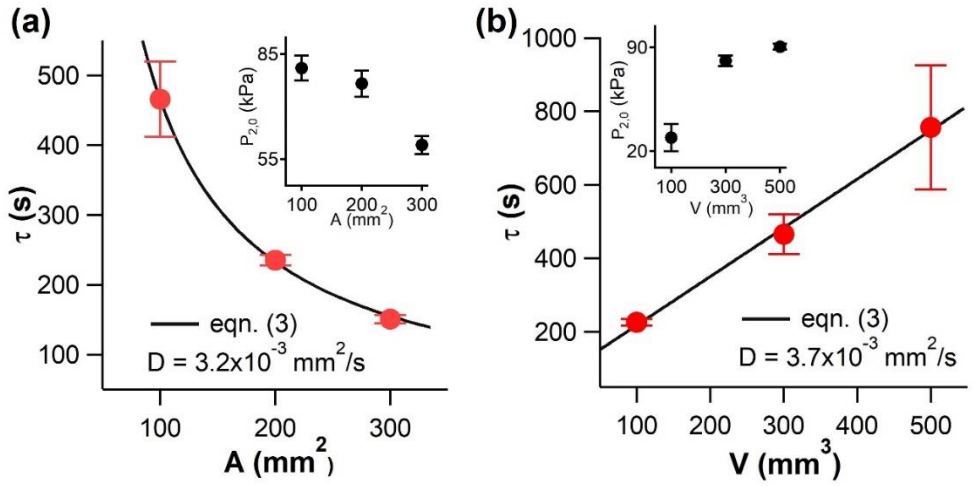

Figure 42. Characteristic time τ determined from the fit of the fluid velocity, plotted versus either (a) A or (b) V. The black curves indicate fits to the molecular diffusion model described in the text. Insets are the initial pressure of the vacuum pocket corresponding to the each device. All error bars denote ± 1σ.

In addition to A, V_2 is another parameter in designing the vacuum pocket. Figure 42b shows a linear relationship between τ and V_2 at a A = 100 mm^2, which agrees with Eq. (3). When the volume of the vacuum pocket increases, the fluid flow becomes slow in the device. This result indicates that the diffusion of air molecules in the device is limited by a cross-section area

of PDMS *A*. During the degassing process of PDMS devices, $P_{2,0}$ is determined by the number of molecules diffused out of the vacuum pocket ($P_{2,0} = P_{atmosphere} - (N_0/V_2)k_BT$). Consequently, the pressure difference between atmosphere and the vacuum pocket is proportional to (N_0/V_2). Thus, when V_2 increases, $P_{atmosphere} - P_{2,0}$ decreases, resulting in a slow flow rate (Figure 42b inset).

The diffusion model and our data set also enable analysis of the diffusion coefficient *D* value. Air diffusion through the PDMS membrane was extracted by fitting Eq. (3) to Figures 42a and 42b, which resulted in *D* of 3.2×10^{-3} mm^2/s and 3.7×10^{-3} mm^2/s, respectively. These values were in excellent agreement with well-known *D* values of PDMS ($2.2 \sim 5.1 \times 10^{-3}$ mm^2/s) [94]. Therefore, the molecular diffusion model providing the relationship between τ and the vacuum pocket parameters allows us to estimate and control fluid dynamics of the self-powered PDMS devices by varying two simple geometrical parameters, *A* and V_2 of the built-in vacuum pocket.

Plasma Separation From Whole Blood Using Self-powered PDMS Devices

We demonstrate the feasibility of a simple, on-chip plasma separation using the pressure-driven, self-powered PDMS devices consisting of a microchannel and vacuum pocket-patterned PDMS bottom layer and either PDMS or acrylic top covering layers (Figures 37, 38, and 43). When a 10 μl drop of the whole blood sample was placed at the inlet, reduced P_1 induced the diffusion of air molecules from the microchannel to the vacuum pocket, pulling whole blood from the inlet to the plasma collection reservoir. While traveling in the microchannel, the cell-free plasma could be separated by sedimentation. Considering a laminar flow, blood cells' sedimentation length $l_s = 27\bar{v}h\mu(4r^2g\Delta\rho)^{-1}$ was estimated to be 103 mm for a spiral and 71 mm for a linear channel device[95], where $\bar{v}$, h, μ, r, g, and $\Delta\rho$ are the average velocity (0.18mm/s

for a spiral and 0.13mm/s for linear channel), the microchannel height (500μm), the viscosity of plasma (3.5cP), the radius of blood cells (4μm), gravitational acceleration (9.81m/s^2), and the density difference between blood cells and cell-free plasma (97kg/m^3), respectively. After passing l_s marked by the blue arrow in Figure 43a and 43b, the clear plasma began to flow in the microchannel and reached the collection reservoir.

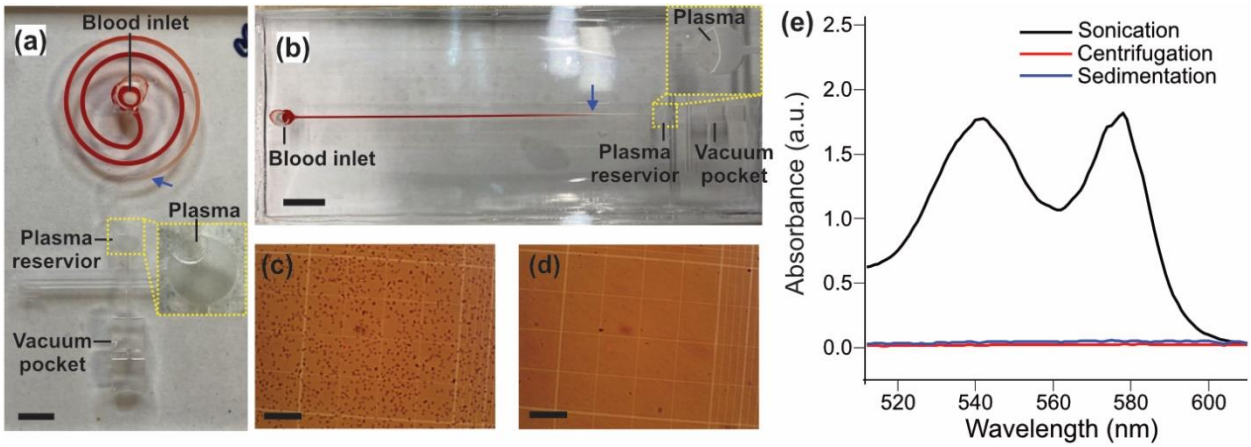

Figure 43. Plasma separation by sedimentation. The operation of the self-powered PDMS device in (a) spiral and (b) linear microchannel design. The scale bars are 5 μm (a) and 10 μm (b). Blue arrow represents the theoretical blood cell sedimentation length. Hemocytometer grid images of (c) whole blood and (d) plasma obtained from the device. The scale bars are 0.25 mm. (e) Absorbance spectrum of lysed blood and plasma characterizing the concentration of free hemoglobin.

To assess the separation efficiency of plasma isolated from the on-chip, self-powered PDMS devices, the percentage of cells removed from the inlet blood sample were measured using the hemocytometer. The optical images of whole blood from the inlet (Figure 43c) and plasma reservoir (Figure 43d) on the hemocytometer grid revealed no cells in the plasma, yielding the separation efficiency $e = (1 - N_P/N_B) \times 100\% = 99.93$ %, where N_p (32.5×10^4 cells/ml) and N_B (48.4×10^7 cells/ml) are the number of cells in plasma and blood, respectively[82], [96]. The plasma quality was also determined by UV-Vis spectrum analysis. The concentration of free hemoglobin in the plasma significantly increases when blood cells are

damaged or ruptured by strong searing force during any separation process in the device[97]. Figure 43e displays absorbance spectra of three samples: lysed blood sample prepared by sonication (black curve); plasma obtained from the conventional centrifugation method (red curve); and plasma obtained by sedimentation from the self-powered PDMS devices (blue curve). Two strong absorption peaks around 540 and 580 nm, signatures of hemoglobin, were observed with the sonicated blood sample, demonstrating high concentration of free hemoglobin in the lysed blood sample[78]. In contrast, no peak on the spectra was observed with both plasma obtained from centrifugation and the PDMS devices, indicating that no blood cell was lysed or damaged during the separation process in the devices. Taken together, the self-powered PDMS device exploiting sedimentation provides an alternative, on-chip, droplet separation of plasma with high separation efficiency and high quality, eliminating complicated microchannel structures, tubing, and external pumps.

Conclusions

In summary, we prepared microfluidic device by using PDMS and successfully separated plasma from blood. The blood was infused by either syringe pump or degassed-PDMS pump. With a problem of blood cell sedimentation on the bottom of tube and syringe, we used power-free device using characteristic of PDMS absorption and permeability. Simple experimental results show that the relation of blood flow rate between number of lung pairs, volume size of vacuum void, and degassing pressure. We also demonstrated that the molecular diffusion model agreed well with the experimentally observed blood flow in the self-powered PDMS devices. By adjusting two geometrical parameters of the vacuum pocket, one can easily achieve a controlled, on-chip fluid pumping system for microfluidic devices, for example, droplet separation of

plasma from whole blood using the sedimentation process presented here without any external power or complex accessories.

CHAPTER 4. PARTICLE SEPARATION USING DETERMINISTIC LATERAL DISPLACEMENT ON PHOTOLITHOGRAPHY PROCESSED DEVICE[3]

Introduction

Laminar Flow in Microfluidic Channel

Microfluidic is a process or manipulation of a small amount of fluid in a channel with small dimensions [98]. Many studies have examined particle separation from a complex medium in microfluidic systems [99], [100]. In laminar flow, fluids flow in parallel in the channel. They do not mix convectively; only molecular diffusion occurs at the interface between fluids [101]. This phenomenon allows many processes to occur in the microfluidic channel, including particle separation and sample preparation.

In this chapter, the relationship between flow rate and width of streamline will be discussed at the point where multiple streams from inlets merge to a single channel in microfluidic devices. We assumed that the fluid is fully developed and the same height as the channel.

Two inlets

Flow rate is calculated by fluid velocity times the cross-sectional surface area of the channel [102]:

$$Q_1 = W_1 \cdot h \cdot v_1 \tag{8}$$

$$Q_2 = W_2 \cdot h \cdot v_2 \tag{9}$$

$$Q_3 = Q_1 + Q_2 = d \cdot h \cdot v_3 \tag{10}$$

[3] The material in this chapter was co-authored by Myungkeun Oh, Sung Oh Woo, and Yongki Choi. Myungkeun Oh had primary responsibility to perform experiments. Myungkeun Oh collected and analyzed experimental data.

where Q is flow rate, W is the width stream, h is the channel height, v is the fluid velocity, and d is channel width.

The equation form can be changed to solve for fluid velocity from the flow rate equation:

$$v_1 = \frac{Q_1}{W_1 \cdot h} \tag{11}$$

$$v_2 = \frac{Q_2}{W_2 \cdot h} \tag{12}$$

$$v_3 = \frac{Q_1 + Q_2}{d \cdot h} \tag{13}$$

Since v_1, v_2, and v_3 are the same in a single channel, it is possible to combine the equations as shown below to estimate the width of each stream:

$$W_1 = d\frac{Q_1}{Q_1 + Q_2} \tag{14}$$

$$W_2 = d\frac{Q_2}{Q_1 + Q_2} \tag{15}$$

Three inlets

As with two inlets, we can induce the width of stream with three inlets:

$$W_1 = d\frac{Q_1}{Q_1 + Q_2 + Q_3} \tag{16}$$

$$W_2 = d\frac{Q_2}{Q_1 + Q_2 + Q_3} \tag{17}$$

$$W_3 = d\frac{Q_3}{Q_1 + Q_2 + Q_3} \tag{18}$$

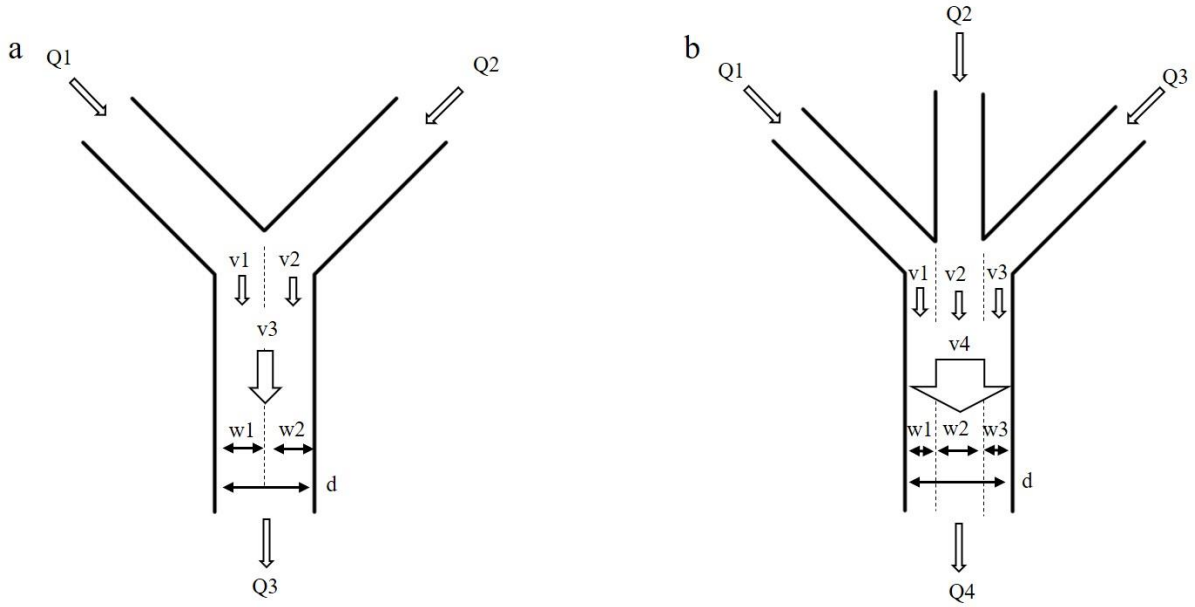

Figure 44. Schematic images of fluid flow on stream width when multiple streams merge to one channel. Fluid velocity in the channel is the same. (a) Streams from two inlets. (b) Streams from three inlets.

Deterministic Lateral Displacement (DLD)

DLD is a relatively recent research area compared to other passive techniques [103] for particle separation in microfluidic systems. Several studies successfully separated micro- and nano-sized particles, such as DNA [104], exosomes [105], red blood cells [106], and circulating tumor cells [107], [108] from complex media, including blood. Particles suspended in solution infused from one inlet and either DI water or buffer infused from one or two microfluidic channel inlets (sheath flow) with multiple inlets. Then, the particles separate while the solutions pass through the hydrodynamic DLD array.

The basic concept of the DLD is very similar to pinched flow [68]. The flow direction of particles in suspension in the microchannel is determined by hydrodynamic forces around the particle in single or multiple streams. For example, if a particle diameter is smaller than the stream width, the particle is forced only from the stream. Then, the flow direction of the particle in suspension follows only the stream. If a particle diameter is larger than the width of a single

stream, the particle gets forced from multiple streams. So, the flow direction of the particle in suspension in a microchannel is determined over one stream. Considering this concept, DLD is a technique to intentionally create multiple streams by placing the same post size consistently with the same pattern in the channel. The single stream divides into several streams while passing the DLD structure. Particles smaller than the width of the single stream flow by following the single stream (zigzag mode). The particle flow direction of particles, which is at least twice larger than the width of the single stream, is determined by the multiple streams (displacement mode).

Theoretically, the critical particle diameter of D_c is at least twice the width of a single stream, but the equation representing D_c is determined by many experiments. The width of several streams between posts is not consistent because of the non-slip boundary condition (velocity profile in channel is a parabolic shape) [109]–[111].

$$D_c = 1.4G\epsilon^{0.48} \tag{19}$$

where, G is the gap between posts, ε is σ/λ, σ is a lateral distance, and λ is the distance between post centers (Figure 45). After determining D_c based on the particles will be tested, one can determine the gap size of G, which should be larger than D_c to prevent particle clogging between posts. Other parameters will be determined by instrumental limits and adjusting each parameter.

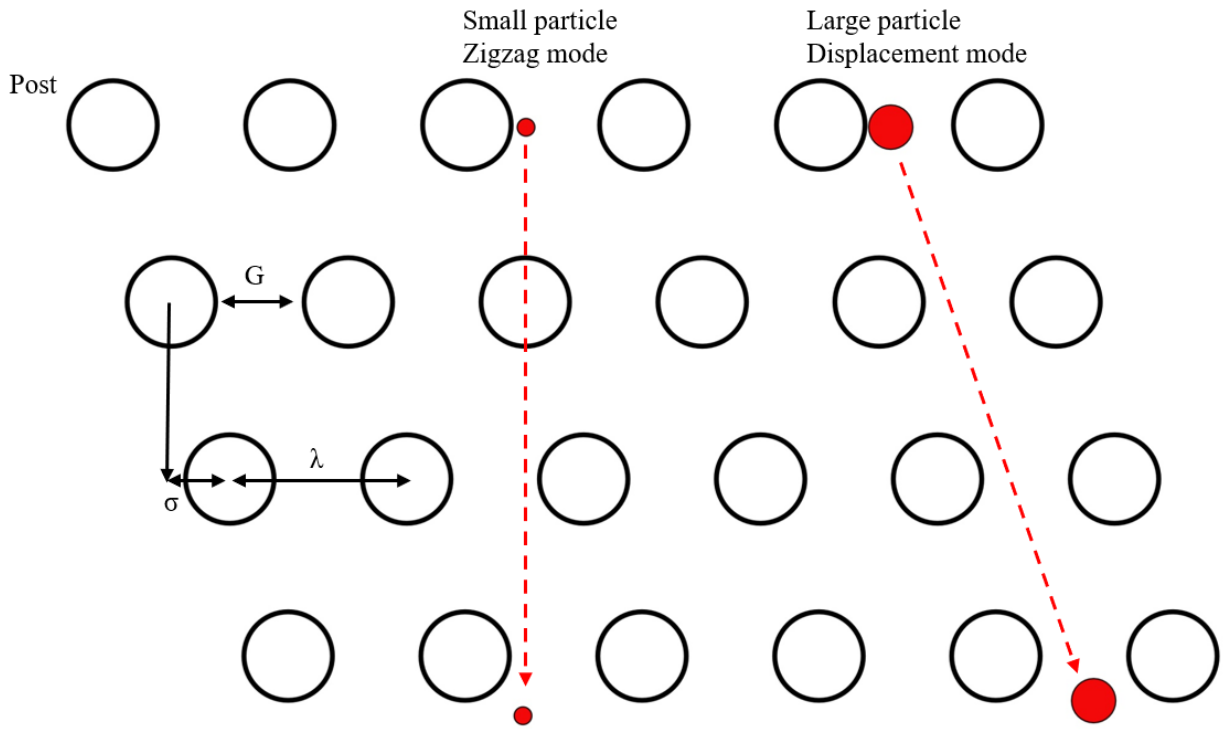

Figure 45. Principle of deterministic lateral displacement (DLD). The trajectory of particles smaller than D_c is straight, and that of particles larger than D_c is diagonal. G is a distance between posts, σ is a lateral distance, and λ is a distance between post centers.

Microfabrication

Microfabrication is the process of manufacturing a micrometer scale structure on materials including silicon wafer and glass. The technique of microfabrication was developed as an advance in the semiconductor industry. Today many other fields, including pharmaceuticals and medicine, apply microfabrication techniques to develop devices. The micrometer-scale structure can minimize the size of the entire device, allowing it to be portable by integration with particle separation and sensing techniques. The design allows people to maximize the use of biological samples, operational time, and more.

Several consecutive steps are required, including photolithography, soft lithography, thin film deposition, etching, and bonding to create microfluidic devices in the microfabrication

process. In this study, we engraved microchannel on silicon wafers using photolithography, aluminum film deposition, and dry and wet etching. We then bonded microfabricated silicon chips with PDMS using oxygen plasma. The oxygen plasma procedure will be discussed in detail later.

Materials and Method

Materials

Polystyrene particles and dye solution

Different sizes of fluorescent-labeled polystyrene particles (mean diameter, 0.042μm, 0.196μm, 0.989μm and 2.19μm) were purchased from Bang Laboratories Inc. Four sizes of polystyrene particles (mean diameters 2.60μm, 3.43μm, 4.16μm, and 5.12μm) were also purchased from Spherotech. The polystyrene particles were used for particle separation in the deterministic lateral displacement study. Diluted food coloring solutions were used to study laminar flow in microfluidic channels.

Microfabrication instruments and materials

We designed microfluidic devices with free software, KLayout and Photomask (Figure 46a) fabricated at the University of Minnesota Nanofabrication center. The Photomask design is chrome on soda lime glass for positive photoresist (UV light exposed photoresist become soluble). Device fabrication on a silicon wafer was performed in a cleanroom (class 100) at the Center of Nanoscale Science and Engineering at North Dakota State University, using a 4” (100) with a 475 – 575μm thick silicon wafer (Nova Electronic Materials) for microfluidic devices. SUSS MicroTec RC8 MS3 spin coater, SUSS MA 8 mask aligner, Kurt Lesker CMS-18 sputter for aluminum deposition, and Trion RIE plasma etcher were used for the microfabrication process. OPD 262 and aluminum etchant were used to photoresist development and aluminum

etching, respectively. Microfabricated wafers were cut using an ADT wafer dicing saw. A KLA Tencor P-15 Long Scan Profiler (Figure 46d) was used to measure the depth of the etched silicon wafer. After finishing etching the silicon wafer, the final silicon-based microfluidic devices (Figure 46c) were bonded by oxygen plasma with PDMS using a Trion RIE plasma etcher.

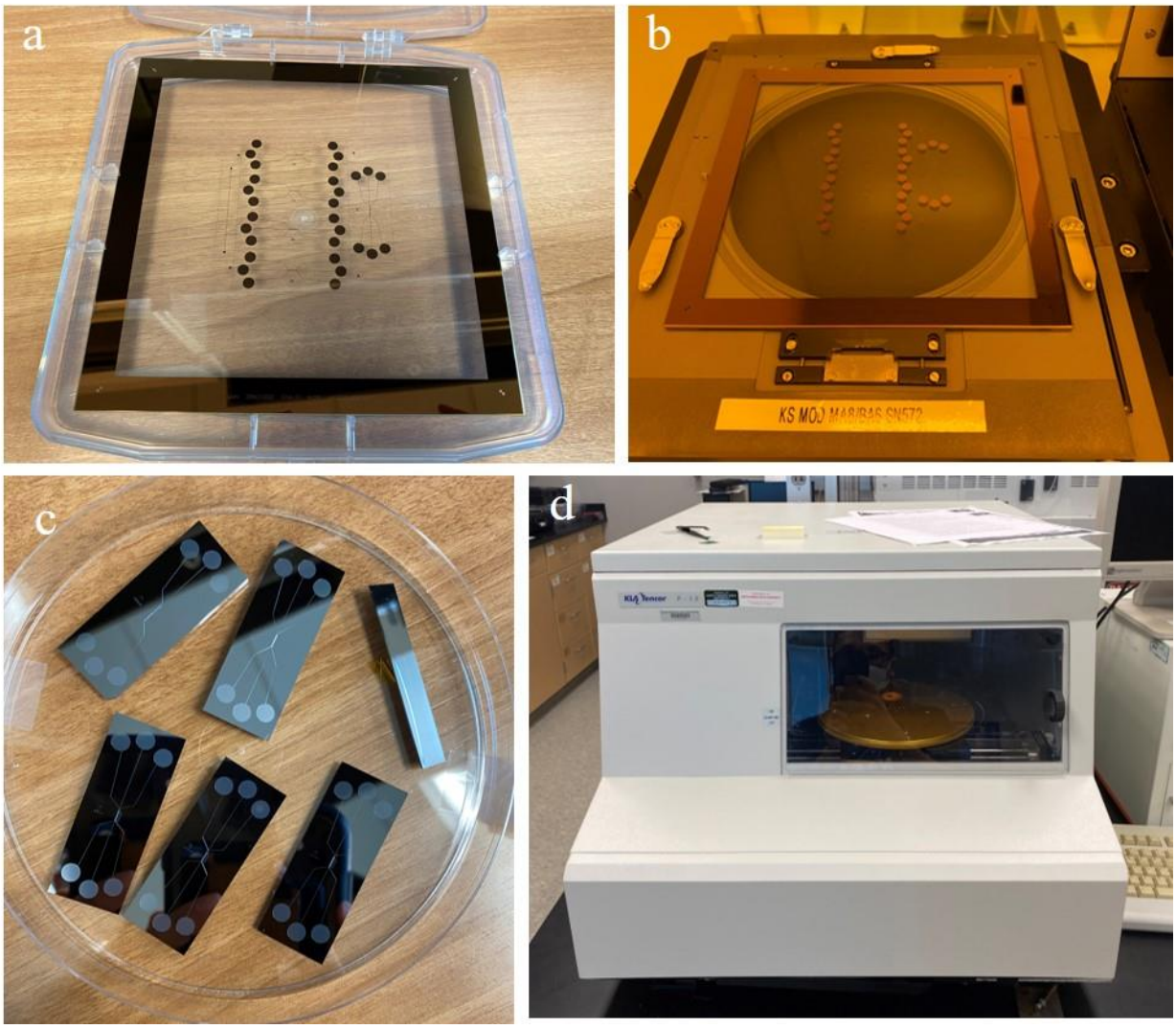

Figure 46. (a) Photomask design. (177mm × 177mm × 5mm, chrome photomask) (b) Photomask on SUSS MA 8 mask aligner for UV exposure. (c) Completed microfluidic devices, cut with an ADT dicing saw. The chip dimensions: 19.9mm x 51.9mm (d) KLA Tencor P-15 Long Scan Profiler.

Experimental materials for microfluidic

Two different syringe pumps were used to infuse a suspended particle solution and sheath fluid: an NE 4000 two channel syringe pump (New Era Pump System) and KDS 100 single syringe pump (KD Scientific). Either a 1ml syringe (Norm-ject) with adapters (Kinesis) or 50µl gas-tight syringe (Hamilton, 1700 series) with 22-gauge needle were connected to either Tygon tube (outer diameter, 1.5875mm and inner diameter, 0.508mm) or Polytetrafluoroethylene (PTFE) tube (outer diameter, 1.4224mm and inner diameter, 0.8128mm). The Tygon tube is flexible and PTFE tube is stiff. An OMFL600 inverted fluorescence microscope and microscope on a Signatone S-1160A-5 probe station were used to observe particle separation and DLD structure. Images or video were captured by Summit SK2-51MP (OptixCam).

Microfabrication on Silicon Wafer

Instruments in cleanroom work

The following is the microfabrication process for microfluidic chips (Figure 47).

- Cleaning the silicon wafer with acetone and isopropyl alcohol (IPA): Dispense both acetone and IPA on the silicon wafer and run the spin coater with 750 rpm for 5 s and 3000 rpm for 10 s. (changed the spin speed 3000 rpm from program 5) with SUSS MicroTec RC8 MS3 spin coater. (If residual, blow with nitrogen). (Figure 48a).
- Bake in an HMDS oven for 30 min. Put the silicon wafer into the oven and press run button on the oven. (Figure 48b).
- Photoresist application: Apply photoresist by dispensing on silicon wafer and spin at 1000 rpm for 23 s (changed the spin speed 1000 rpm from program 2) in SUSS MicroTec RC8 MS3 spin coater. (Figure 48a).
- Bake it in an oven at 90 °C for 1 min. (Figure 48c).

- Expose UV light for 15s with SUSS MA 8 mask aligner and the photomask operating in proximity mode. (Figure 48d).
- Photoresist development: Remove the UV exposed photoresist by immersing it in development solution (OPD 262, Fujifilm) for 1 minute, in solvent cleaning and development hood. (Figure 48e).
- Aluminum deposition with Sputtering: The silicon wafer was placed in the chamber and we waited until it evacuated approximately 5×10^{-6} torr, and then deposited aluminum for 286 s with 210 Å /min deposition rate. Aluminum was deposited on the silicon wafer at about 1000 Å with 650w Kurt Lesker CMS-18 sputter. (Figure 49a)
- Photoresist removal: Strip photoresist by immersing the silicon wafer in acetone and sonicating, then rinse with IPA in solvent cleaning and development hood. (Figure 48e).
- Silicon etching: Etch silicon by putting the silicon wafer in a chamber of a Trion RIE plasma etcher (100W, Sf6 27sccm). The etching depth of silicon is deeper as the etching time increased. (Figure 49c).
- Deposited aluminum removal: Wet etch aluminum by immersing the aluminum deposited silicon wafer in the Aluminum Etchant Type A (Transene) with an etch rate of 100 Å /s for 15sec at less than 50 ºC on utility bench. (Figure 49b).

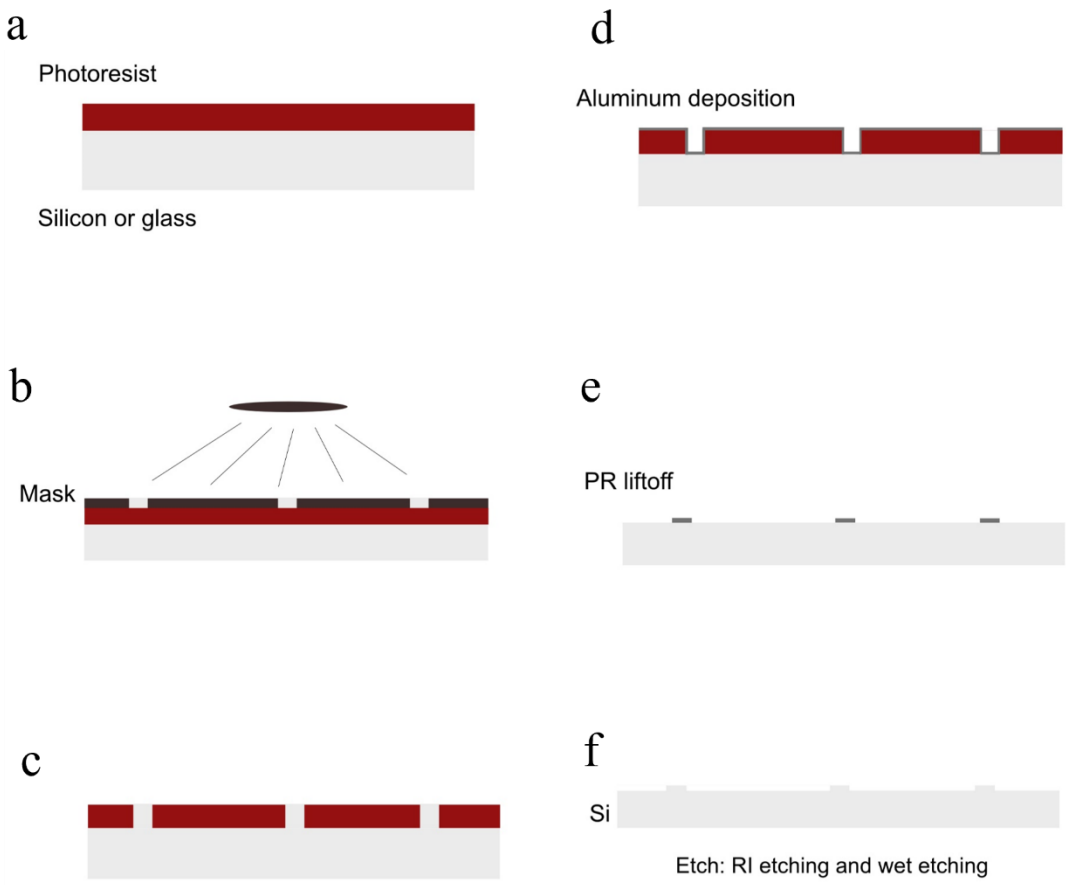

Figure 47. Microfabrication of DLD structure on a silicon wafer. (a) Application of photoresist with spin coater (1000 rpm). (b) 15s of UV exposed photoresist with photomask. (c) Development of photoresist with OPD 262 solution. (d) Aluminum deposition (1000 Å height) on the surface. (e) Eliminated of photoresist with isopropyl alcohol. (f) Etched silicon wafer with wet and dry etching.

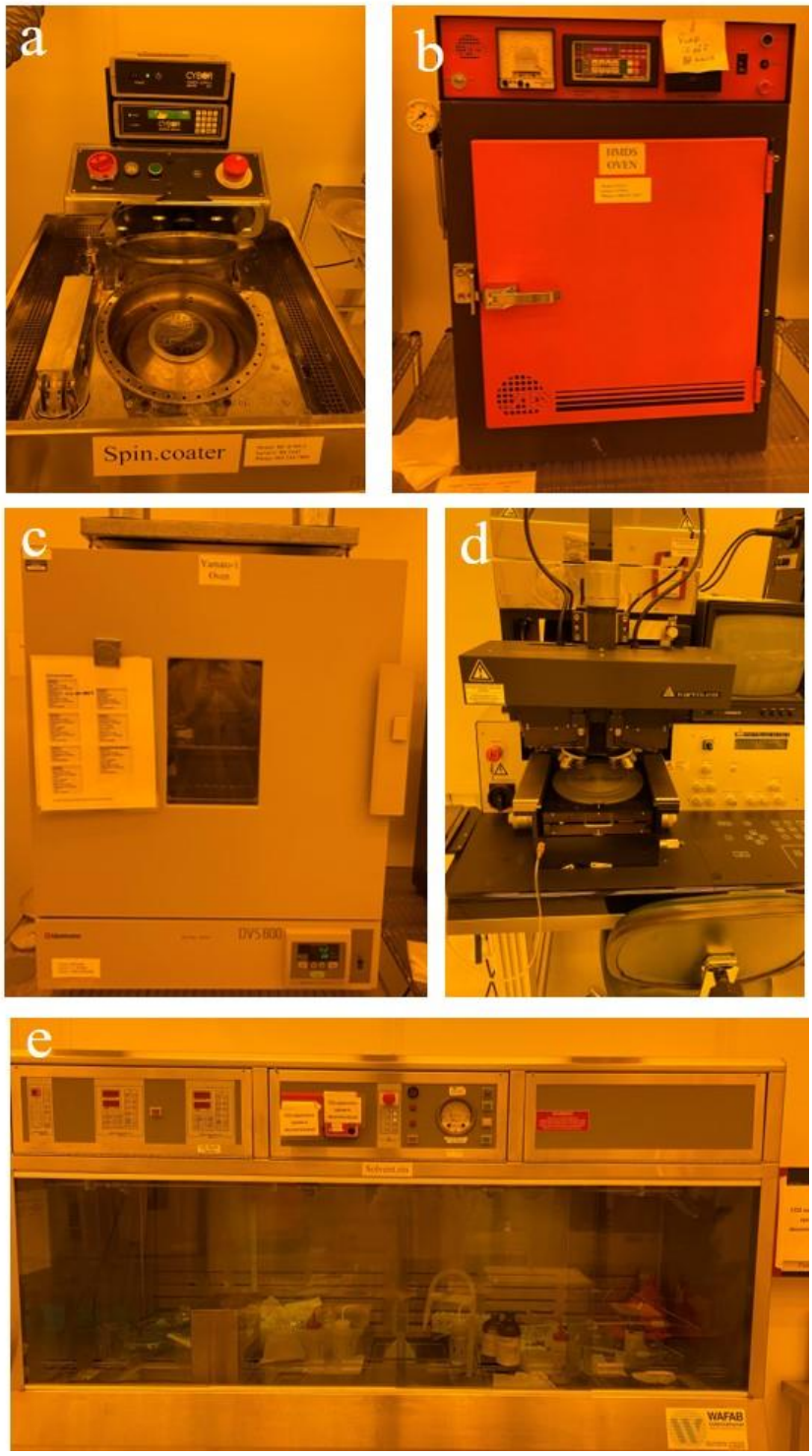

Figure 48. Instruments for microfabrication in a cleanroom (class 100). (a) SUSS MicroTec RC8 MS3 spin coater. (b) HMDS oven. (c)Yamamoto oven. (d) SUSS MA 8 mask aligner. (e) Solvent cleaning and Development hood.

Figure 49. Instruments for microfabrication in a cleanroom. (a) Kurt Lesker CMS-18 sputter for aluminum deposition. (b) Utility bench. (c) Trion RIE plasma etcher.

Instruments manufactured in the laboratory

We also performed a microfabrication process is our laboratory with instruments made in-house. The following is the procedure using the in-house instruments:

- Clean silicon chips/wafers using nitrogen, sonicate for 5 min in acetone, wash acetone/IPA, then blow with nitrogen gas.
- Dehydrate on a hot plate at 115°C for 5 min.
- Apply photoresist at 500 rpm for 5 s and 5000 rpm for 50 s. (Figure 50a).
- Bake the photoresist at 115°C for 90 s on a hot plate.
- UV exposure (1A power supply, 0.9mW/cm^2 of UV power at the center, 85 s UV exposed time). (Figure 50b).

- Develop the silicon chips/wafers with MF-319 about 60 s, then wash with DI water and blow with nitrogen gas.

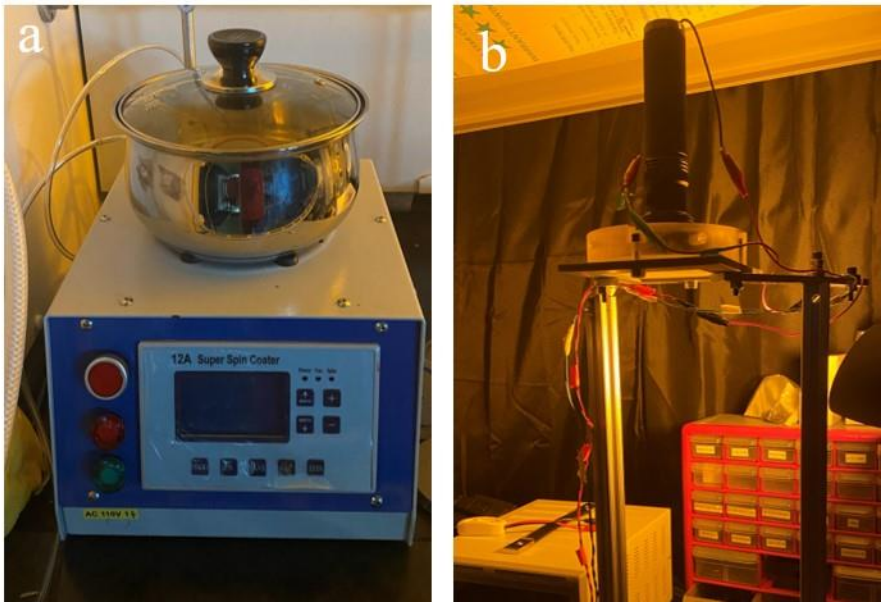

Figure 50. In-house instruments for microfabrication in the laboratory. (a) Ultraviolet light for patterning photomask on a silicon wafer. (b) Spin coater.

Device Inspection

Scanning electron microscopy (SEM)

Performing an intermediate inspection while in the microfabrication process an important because it allows for the detection of unexpected issues, such as silicon wafer contamination and irregular photoresist application. Any issues can then be immediately corrected and future problems prevented. First, we inspected the silicon wafer with SEM. Figure 51 shows the photoresist development process, and Figure 52 is a stripped photoresist wafer at different points on the wafer. No major issues were found during the comparison of two silicon wafers according to SEM images.

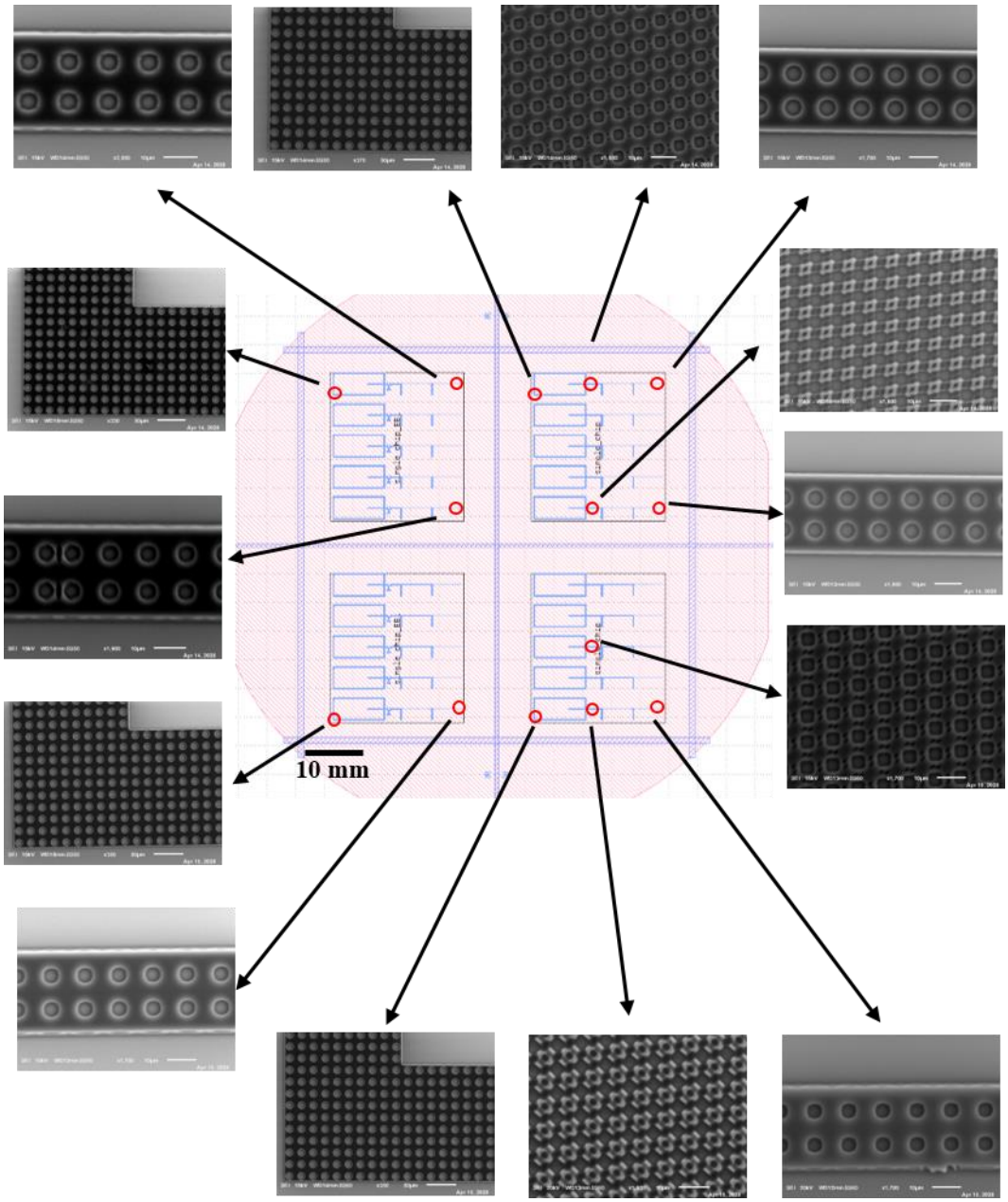

Figure 51. SEM inspection of photoresist development processed 4in silicon wafer (Figure 47, Step 3). The scale bar in SEM images is 10µm.

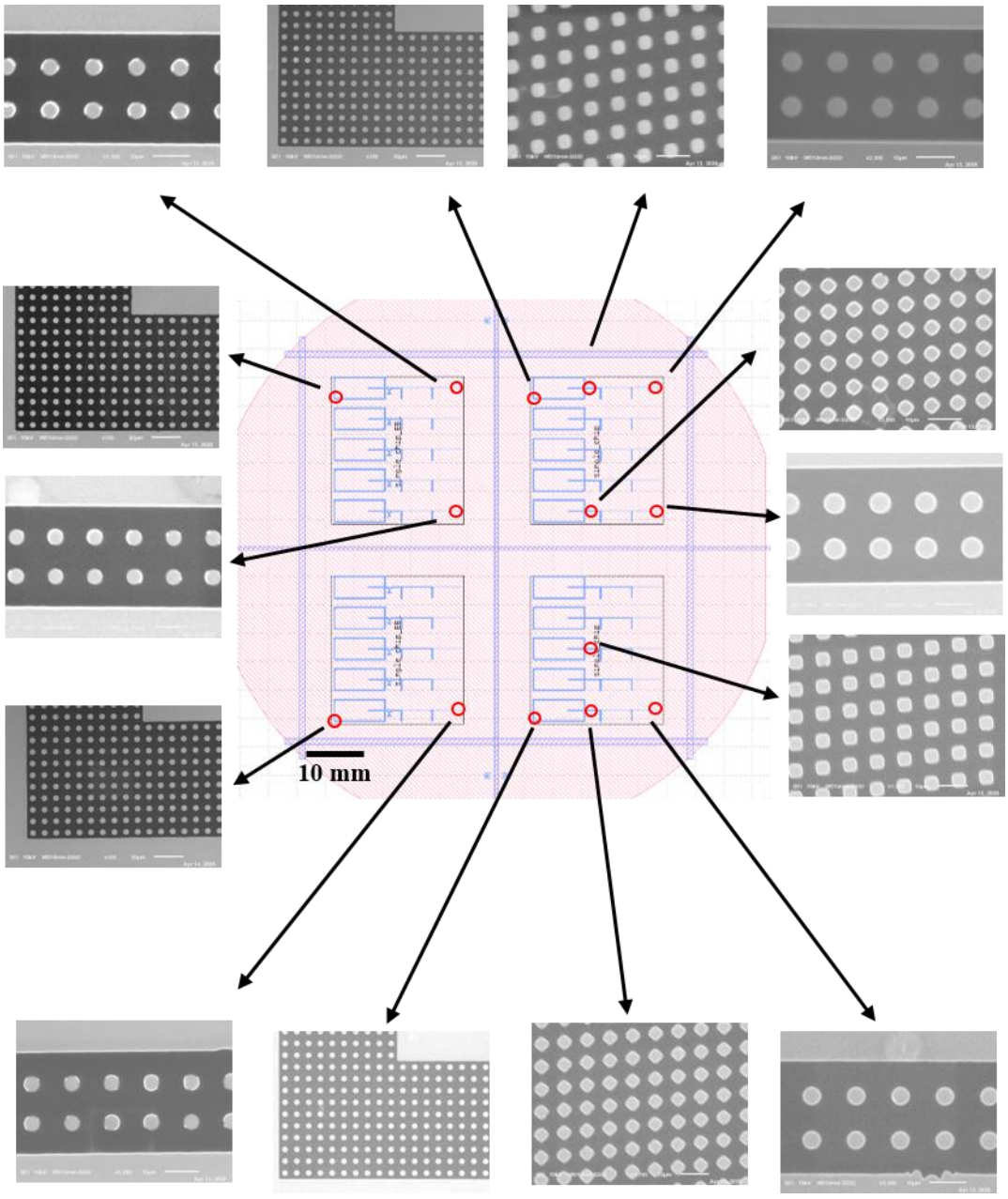

Figure 52. SEM inspection of stripped photoresist in 4in silicon wafer (Figure 47, Step 5). The scale bar in SEM image is 10μm.

Surface profiler

After finishing the microfabrication process, we measured the etching depth with the KLA Tencor Long Scan Profiler, and the depth depended on the etching time. The resolution of the profiler was 0.025μm, calculated by scan speed divided by the sampling rate. We used a

5µm/s scan speed and 200Hz sampling rate. Figure 53a is a measured depth of the etched silicon wafer after processing it with the RIE plasma etcher at 100W and SF6 26 sccm, and 240 seconds. We found that the etching depth on the silicon wafer was approximately 4.5µm.

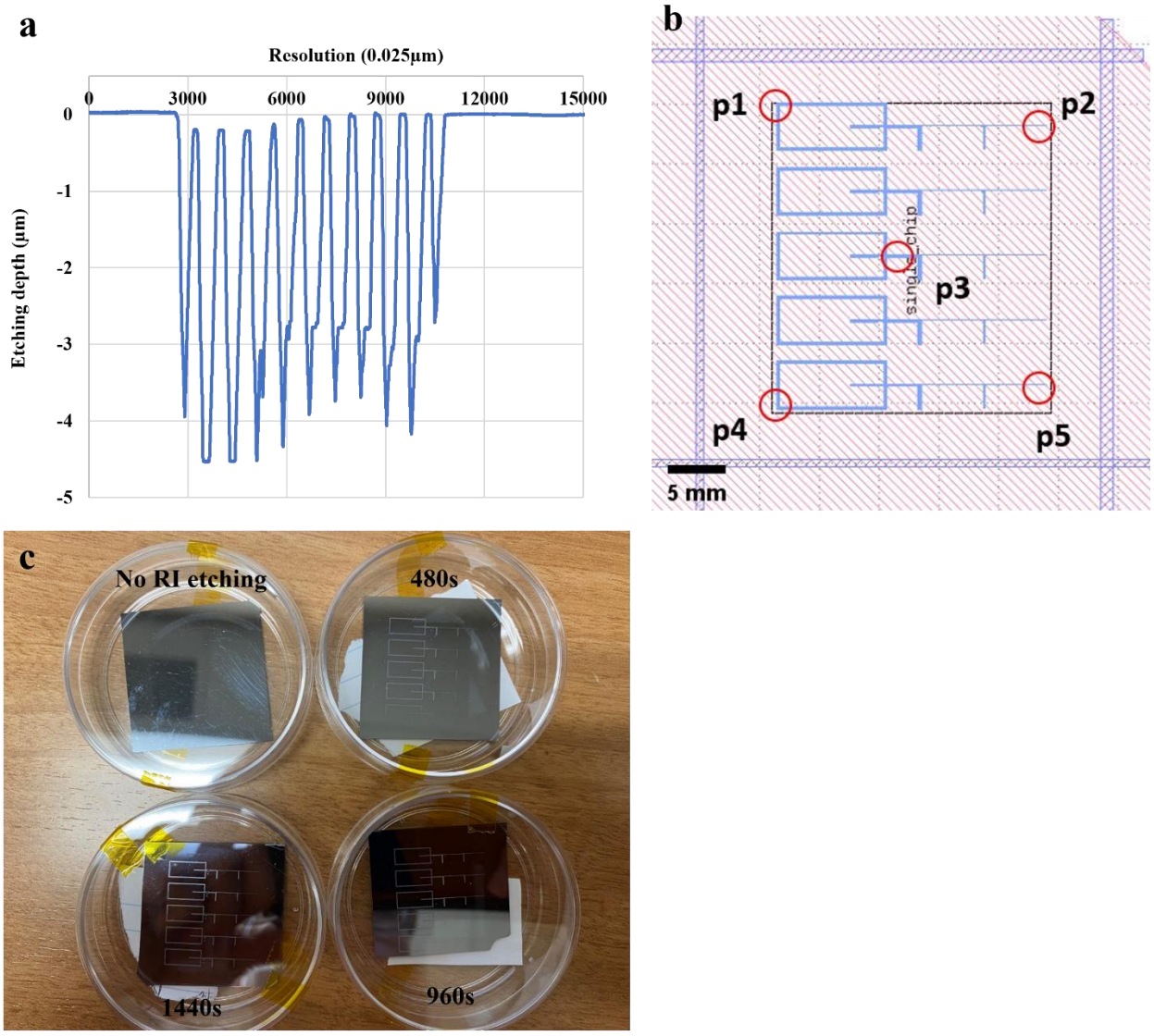

Figures 53. (a) Profile of 240s etched silicon chip measured using the KLA Tencor P-15 Long Scan Profiler. The resolution of the profiler is 0.025µm. (b) Five different points were measured. The chip dimensions: 33mm × 33mm; channel width: 0.2mm; DLD channel length: 0.477mm. (c) 4 silicon chips, one with no RI etching and three with varying time of RI etching (480s, 960s, and 1440s). Microfluidic channel can be seen clearly as etching time increased.

The silicon wafer was etched in the chamber of Trion RIE plasma etcher; the silicon wafer must be fixed on the bottom of the chamber for consistent etching depth during RI etching. However, unfortunately there was an anchor limit for the wafer on the bottom of the chamber in our instrument. The silicon wafer was moving in the chamber during RI etching, which leads to a slightly different etching depth on the wafer. We measured the etching depth at multiple points (Figure 53b). As the etching time of the silicon wafer was increased (480s, 960s and 1440s), an increase in etching depth was observed (Table 1).

Table 1. Change in etching depth based on different etching times.

Etching time	P1	P2	P3	P4	P5	Average
480s	10μm	14μm	13μm	9μm	13μm	9.8μm
960s	17μm	22μm	25μm	15μm	20μm	19.8μm
1440s	30μm	31μm	35μm	32μm	35μm	32.6μm

Bonding Between PDMS and Silicon Chip/Glass

In this study, we bonded PDMS and microfluidic silicon devices using oxygen plasma. In principle, oxygen plasma removes organic materials and changes to the silanol (SiOH) groups on the surface of PDMS, leading to instantaneous hydrophilicity. The silanol group of an oxygen plasma processed surface of PDMS, glass, or silicon wafer forms a Si-O-Si bond upon attachment. This bonding is irreversible and eliminates water leaking between the two attached surfaces so that bonding with oxygen plasma for a silicon chip and PDMS is an excellent method for a microfluidic device. The following is the detailed oxygen plasma process:

- The silicon wafer or glass surface was cleaned with acetone, IPA, and DI water; to prevent contamination, the PDMS was not peeled from the Petri dish before the oxygen plasma process.
- The oxygen plasma operating conditions were 700m Torr, 20W, 30s, 100 sccm O2.

- After the oxygen plasma operation, the PDMS was placed on a silicon wafer or glass, and light pressure was applied for 30 s; the PDMS and silicon wafer were not moved or adjusted.
- The silicon and attached PDMS were heated in the oven (90°C) for 1min, as a high temperature helps form strong bonds.

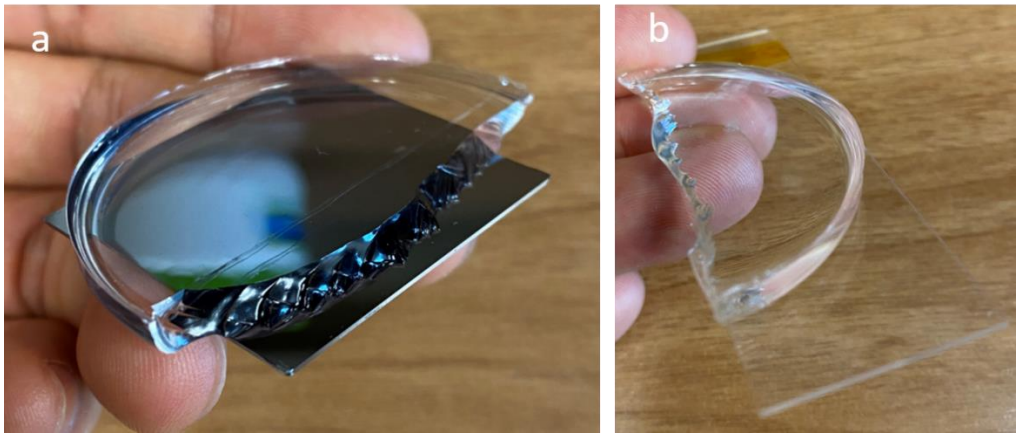

Figure 54. Specimens of oxygen plasma processed bonding. The bonding is irreversible. (a) PDMS and silicon wafer bonding. (b) PDMS and glass bonding.

Microfluidic Design and Tubing System

A minor issue of previous microfluidic designs was the short distance between inlets and small inlet size, making it difficult to align PDMS and the microfluidic device inlet. We modified the design slightly, making the inlet larger and providing adequate distance between inlets. Before bonding, the PDMS had pre-punched inlet and outlet holes. The microfluidic chip and PDMS are bonded with oxygen plasma. The holes for inlets and outlets (1mm diameter) were punched with a Miltex biopsy punch on PDMS, smaller than the outer diameter of the Tygon (1.5875mm) and PTFE (1.4224mm) tubes. So, the Tygon or PTFE tube were directly plugged into the PDMS hole without any assistant adapter (Figure 55). The elasticity of PDMS helps to hold the tubes while the fluids are infusing.

Figure 56 is a modified design of a microfluidic chip. We designed the inlet and outlet diameter to be about 5mm, which is bigger than the tube diameter (about 1.5mm). Since the tube diameter is smaller than the inlet and outlet, it is easy to align PDMS and the chip when we punch holes on PDMS. We constructed pillars on the fluidic channel, which connects between the inlet/outlet and the DLD to prevent top PDMS collapse. Detailed information of the critical diameter of the particle, diameter of the post, the gap between posts, and other data is in the Table 2.

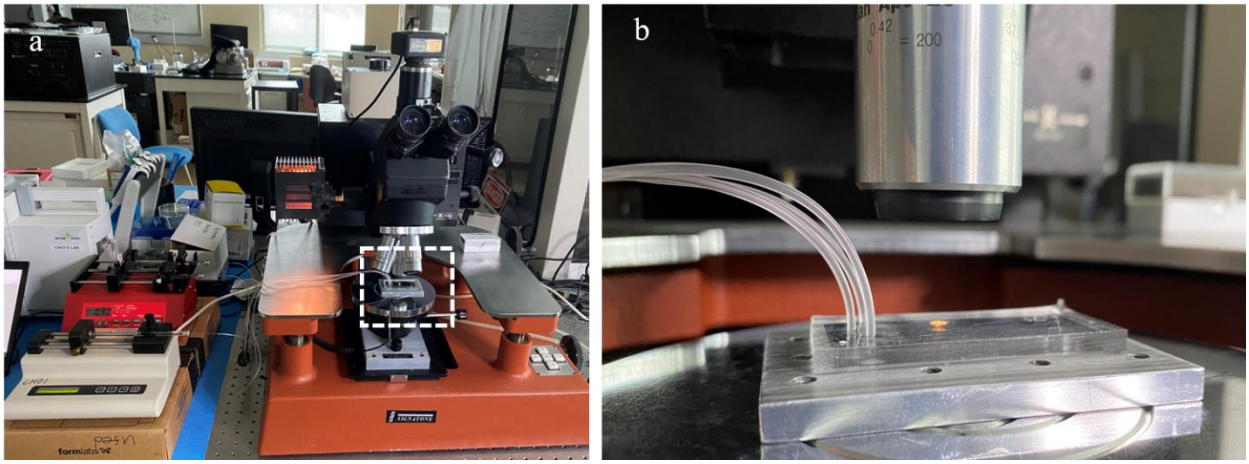

Figure 55. Experimental setup. (a) Syringe pumps and microfluidic chip are connected with tubes. (b) The tubes are directly plugged into the microfluidic chip without any adapters.

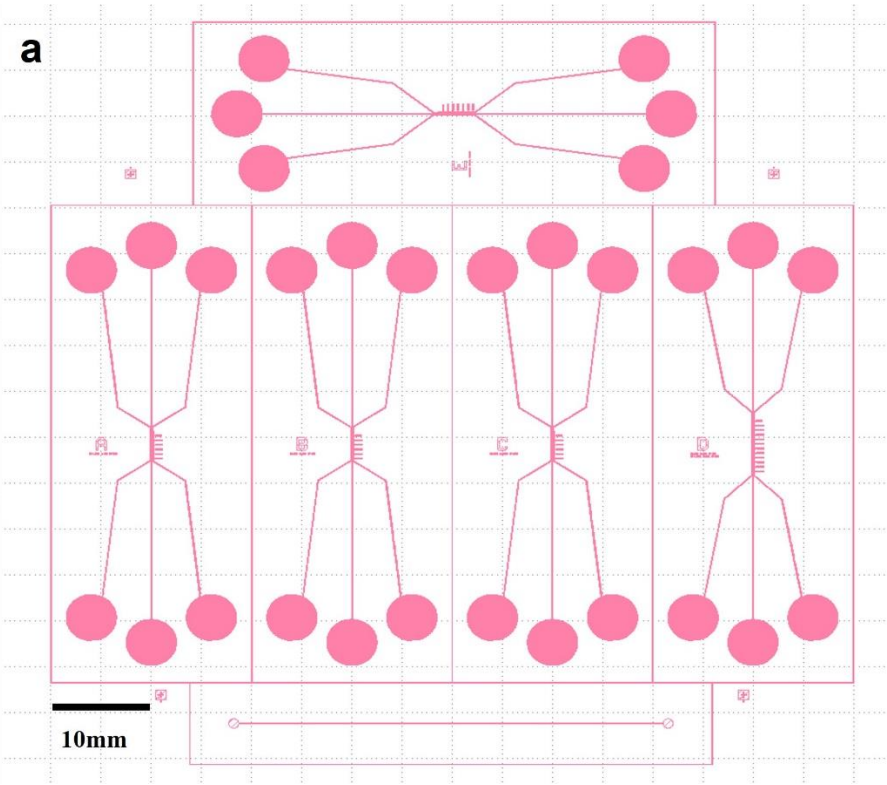

Figure 56. We modified DLD microfluidic chip design to resolve minor issues from the previous design of short distance between inlets and small diameter of the inlet. The issues made it difficult to align PDMS and microfluidic device inlet. (a) DLD microfluidic chip design in 4-inch (101.6mm) wafer. The DLD channel length: 3.2mm (Chip A, B, C, E) and 6.5mm (Chip D). (b) The chip dimensions: 19.9mm × 51.9mm; inlet and outlet diameter: 5mm. (c) Supporting post in inlet and outlet. The post diameter is 12.5μm. (d) The supporting post in fluid channel. The post diameter is 12.5 μm. The width of fluid channel: 0.1mm; (e) DLD design for single silicon chip. The channel width is 0.3mm, the diameter of post in DLD is 9μm.

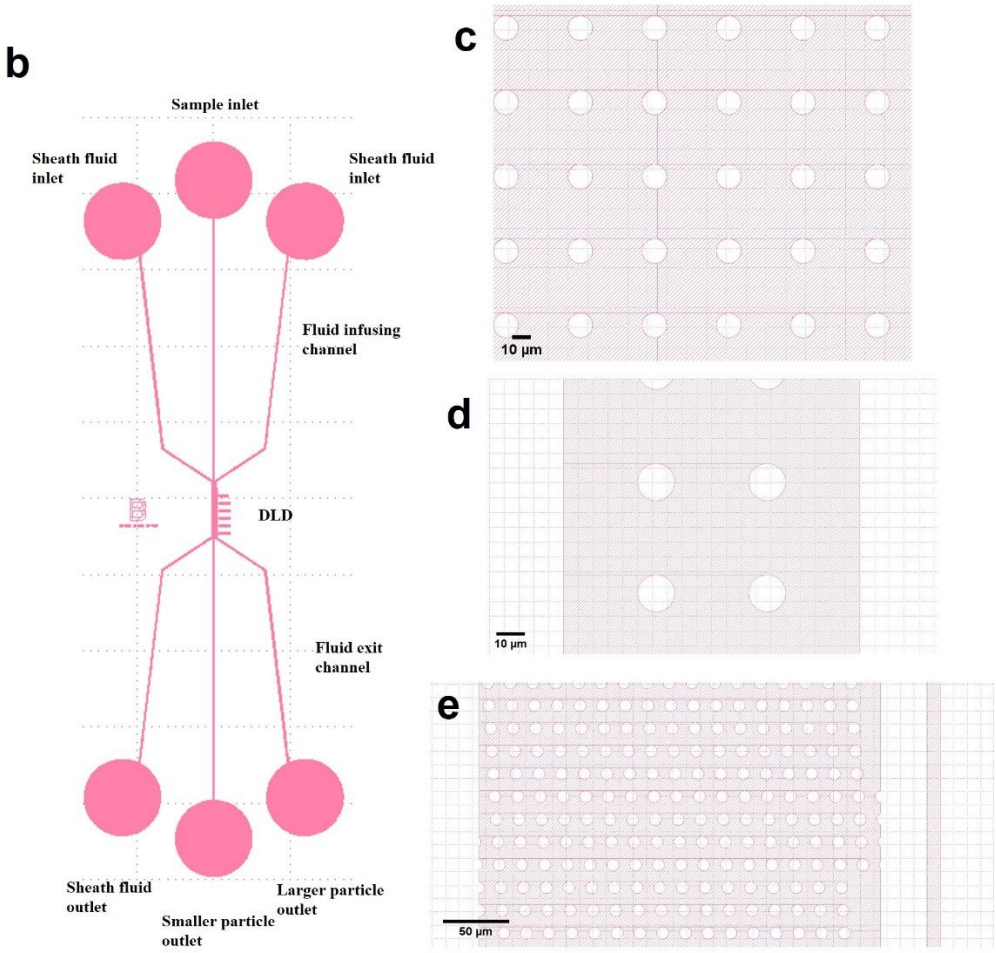

Figure 56. We modified DLD microfluidic chip design to resolve minor issues from the previous design of short distance between inlets and small diameter of the inlet (continued). The issues made it difficult to align PDMS and microfluidic device inlet. (a) DLD microfluidic chip design in 4-inch (101.6mm) wafer. The DLD channel length: 3.2mm (Chip A, B, C, E) and 6.5mm (Chip D). (b) The chip dimensions: 19.9mm × 51.9mm; inlet and outlet diameter: 5mm. (c) Supporting post in inlet and outlet. The post diameter is 12.5μm. (d) The supporting post in fluid channel. The post diameter is 12.5 μm. The width of fluid channel: 0.1mm; (e) DLD design for single silicon chip. The channel width is 0.3mm, the diameter of post in DLD is 9μm.

Table 2. Parameters for the microfluidic device.

Chip name	Dc (m)	G (m)	Post diameter (m)	ε	δ (m)	λ (m)
A	1.5e-6	4e-6	5e-6	0.0643	5.8e-7	9e-6
B	3e-6	8e-6	9e-6	0.0643	1.1e-6	1.7e-5
C	5e-6	1.1e-5	1.2e-5	0.0959	2.2e-6	2.3e-5
D	3e-6	8e-6	8e-6	0.0643	1.5e-6	1.6e-5
	1.5e-6	4e-6	8e-6	0.0643	7.7e-7	1.2e-5
E	7e-7	2e-6	3e-6	0.0557	2.8e-7	5e-6

Results

Laminar Flow in Microfluidic Channel

Fluids flow parallel in the channel by laminar flow. We infused three fluids to three different inlets at different flow rates and measured the width of each stream from the channel. Then, the theoretically calculated width of the stream was compared to measure the stream width using the equations (16), (17), and (18).

PDMS device (millimeter scale)

Figure 57 is an AutoCAD design for laminar flow in microfluidic channels. Three inlets and one outlet are in the device. Three different dye solutions with different flow rates were infused into three inlets using syringe pumps, and they merged at the cross in the red box and flowed parallel to the outlet.

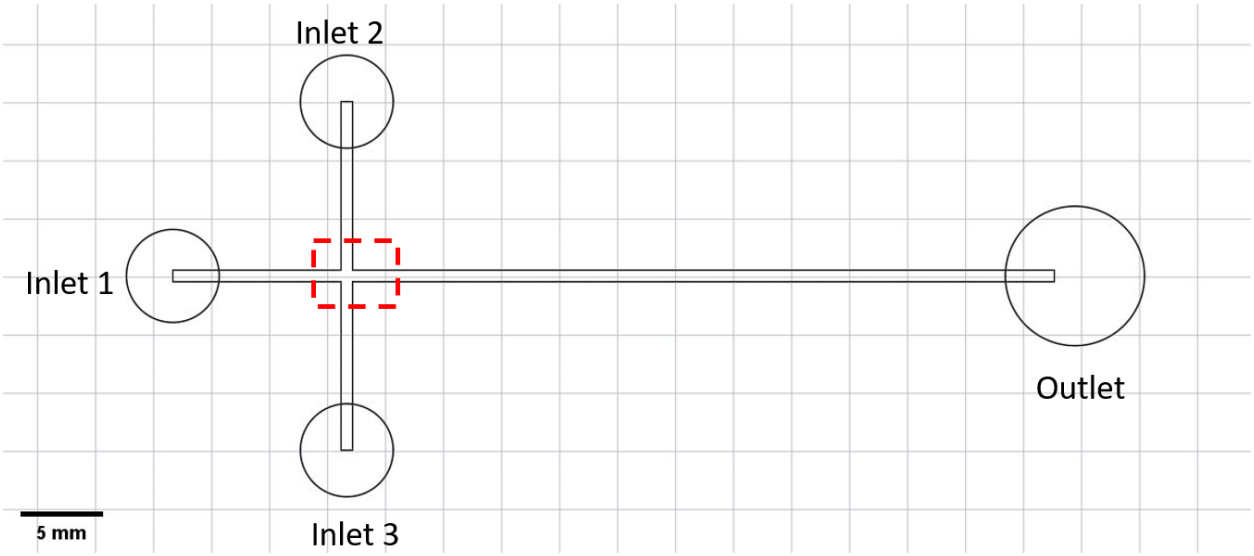

Figure 57. AutoCAD design for the microfluidic device (millimeter scale) laminar flow study. Three dye solutions were infused into three inlets, and they merged at the red box. Three dye solutions exited through the outlet. The device dimensions: 24.5mm × 55.5mm × 5mm, inlet diameter: 4mm, outlet diameter: 6mm, channel width: 0.5mm, channel height: 0.5mm.

Parallel streams were captured with a microscope, and the width of each stream was measured with ImageJ. Figure 58a shows the same flow rate (1ml/h) for all three inlets, Figure

58b is 1ml/h for inlet 1 and 2ml/h for inlet 2 and 3, and Figure 58c is 1ml/h for inlet1 and 3ml/h for inlet 2 and 3. The streams flow parallel by laminar flow, and the stream width from inlet 1 shrunk as the flow rate of inlets 2 and 3 grew.

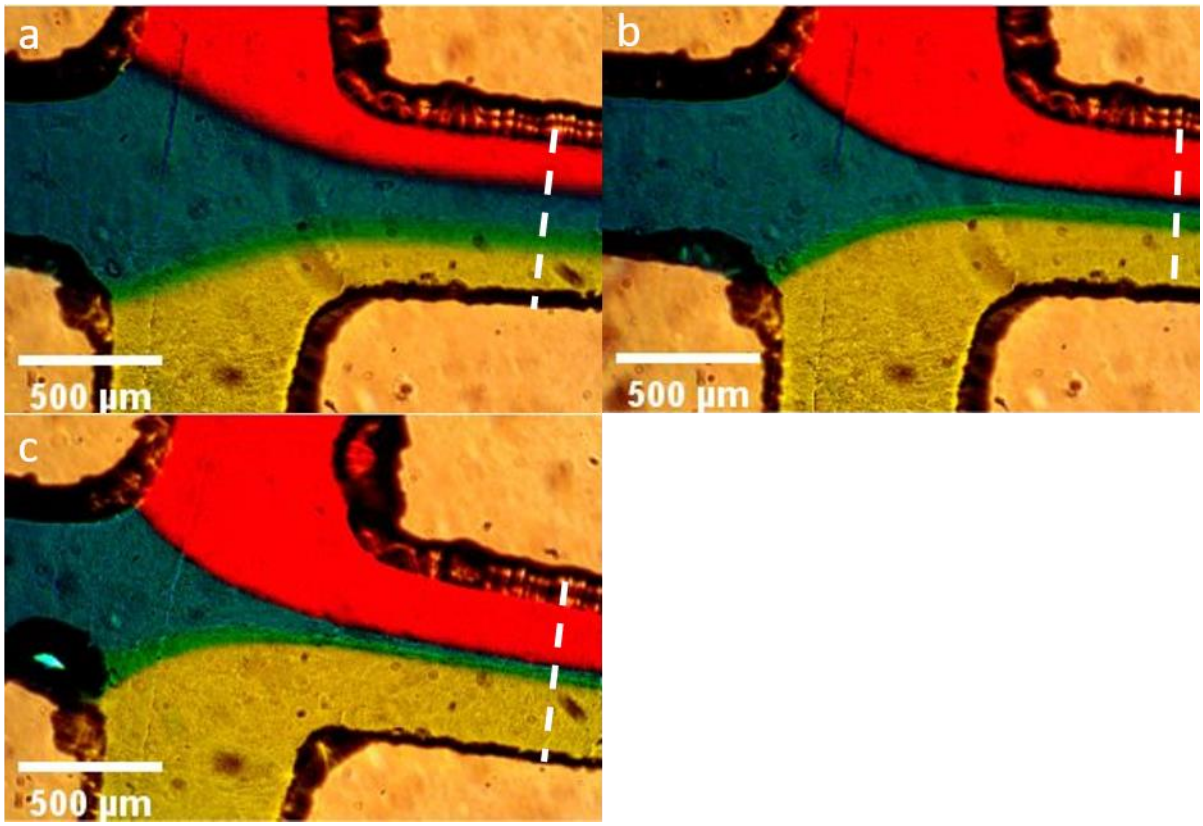

Figure 58. Three dye solutions infused at different flow rates. They merged at the cross and flow parallel. The width of three streams was measured at the white dashed line. The channel width: 0.5mm and height: 0.5mm (a) Inlet 1,1ml/h and inlet 2 and 3, 1ml/h. (b) Inlet 1, 1ml/h and inlet 2 and 3, 2ml/h. (c) Inlet 1, 1ml/h and inlet 2 and 3, 3ml/h.

Table 3 shows the measured width of streams, calculated fluid velocity, and the theoretical width of the streams and velocity of each stream. We measured the width of each stream at the white dashed line (Figure 58) using ImageJ, the depth of the channel is 500um. The fluid rate is determined using a syringe pump, and we could calculate the velocity of each stream from the flow rate equation, $Q = w \cdot h \cdot v = A \cdot v$, where Q is the flow rate, w is the width of stream, v is the fluid velocity, and A is the cross-sectional area of channel. By using eq. (16), (17), and

(18), we were able to estimate the theoretical width of stream since the fluid velocity in the channel is the same.

The experimental values of laminar flow are well fitted to theoretical value considering errors, including friction between the fluid and surface of the wall (no-slip boundary condition).

Table 3. Experimental and theoretical values of width of each stream and fluid velocity.

Flow rate (ml/h)	Measured width (m)	Calculated velocity (m/s)	Theoretical width (m)	Theoretical velocity (m/s)
1 (inlet 1)	1.45E-04	3.83E-03	1.67E-04	3.33E-03
1 (inlet 2)	1.80E-04	3.09E-03	1.67E-04	3.33E-03
1 (inlet 3)	1.62E-04	3.43E-03	1.67E-04	3.33E-03
1 (inlet 1)	7.00E-05	7.94E-03	1.00E-04	5.56E-03
2 (inlet 2)	2.10E-04	5.29E-03	2.00E-04	5.56E-03
2 (inlet 3)	2.20E-04	5.05E-03	2.00E-04	5.56E-03
1 (inlet 1)	6.00E-05	9.26E-03	7.14E-05	7.78E-03
3 (inlet 2)	2.40E-04	6.94E-03	2.14E-04	7.78E-03
3 (inlet 3)	1.90E-04	8.77E-03	2.14E-04	7.78E-03

Silicon wafer (micron scale)

Before we infuse a suspended particle solution into the microfluidic device, microfabricated on silicon chips, dye solutions were infused into the final device for the laminar flow study. Three different solutions wee infused into three inlets; they flowed parallel in the microfluidic devices DLD (Figure 59a). Three different solutions flowed into three different outlets (Figure 59b).

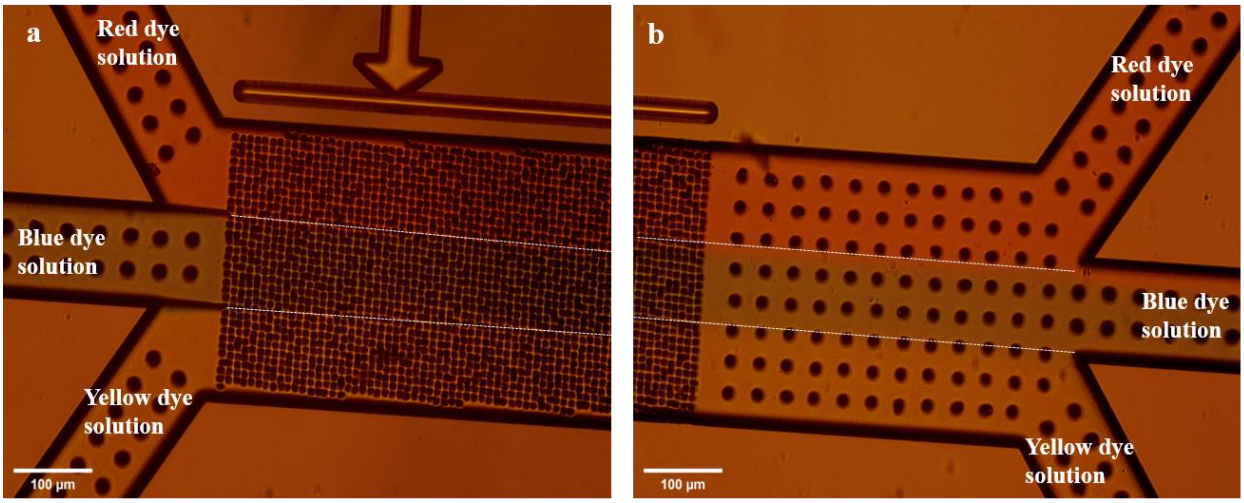

Figure 59. Laminar flow in silicon chips with three different dye solutions. The chip dimension: 19.9mm × 51.9mm, DLD channel width: 0.3mm, DLD channel length: 3.2mm, inlet channel width: 0.1mm. (a) Three dye solutions infused into the DLD structure's left side. (b) Three dye solutions flowed parallel and exited the three outlets. The scale bar is 100µm.

Particle Separation

The particle separation device was prepared by attaching PDMS to the silicon etched chip using oxygen plasma, providing a strong and irreversible bond. There was no water leakage during the use of the microfluidic device. However, if particles became stuck in the channel, there was no way to release them. So, caution is required to prevent particles obstructing the channel, filling sheath fluids in the channel first and then infusing particle suspension into the middle inlet.

Figures 60 and 61 show the particles' trajectory while passing through the DLD structure in the microfluidic device. A single particle is shown in the circle (infused from the top), and it moves straight (zigzag mode) to the bottom since the diameter of the particle (2.6µm) is smaller than the critical particle diameter (D_c =3µm) (Figure 60). While the sample was infused into the microfluidic channel, sheath fluid flow (DI water) assisted particle suspension to provide parallel flow so that particles smaller than Dc flowed straight and particles larger than D_c flowed diagonally. Figure 61 shows the fluorescent particles' trajectory in the DLD. There were

upstream, midstream, and downstream areas. In the particle suspension infused into the middle of the DLD, which is assisted by sheath fluids (upstream), the particles flow straight, both midstream and downstream since the blue fluorescently labeled particles (mean diameter is 0.989μm) are smaller than the critical diameter of design (D_c = 3μm). The particles were collected in the middle outlet.

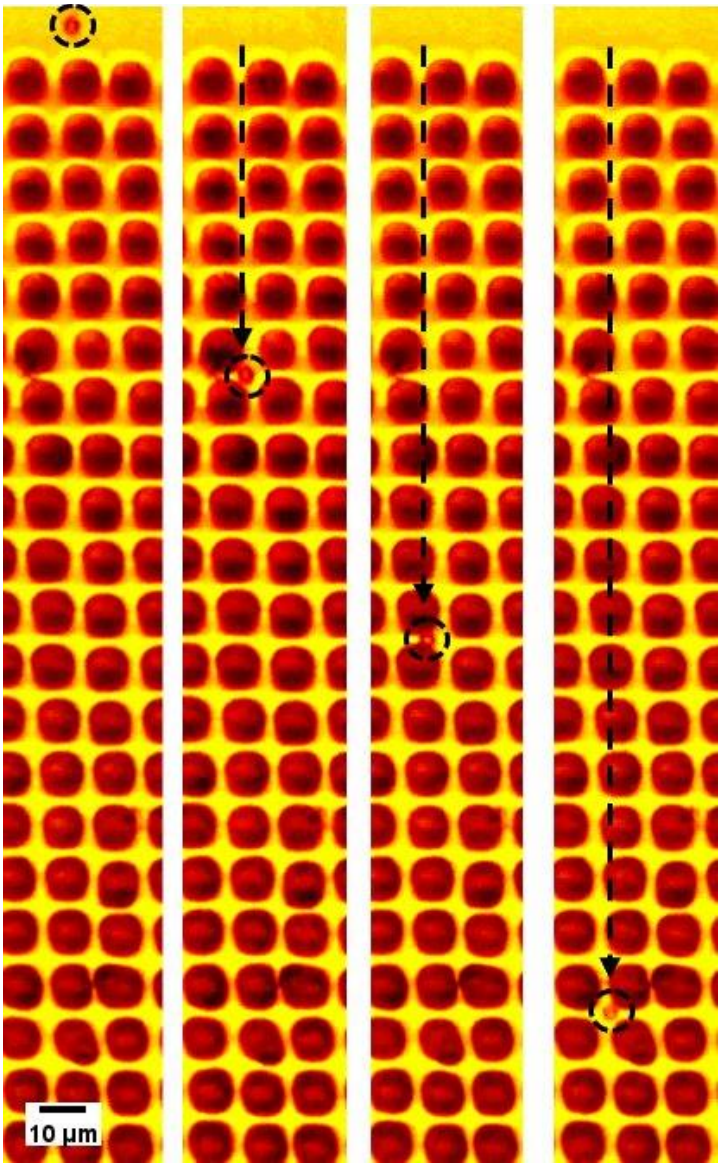

Figure 60. Single-particle flow in DLD. The particle (diameter 2.6μm) is smaller than D_c (3μm), so it flows straight for 45μm. The pillar diameter is 9μm.

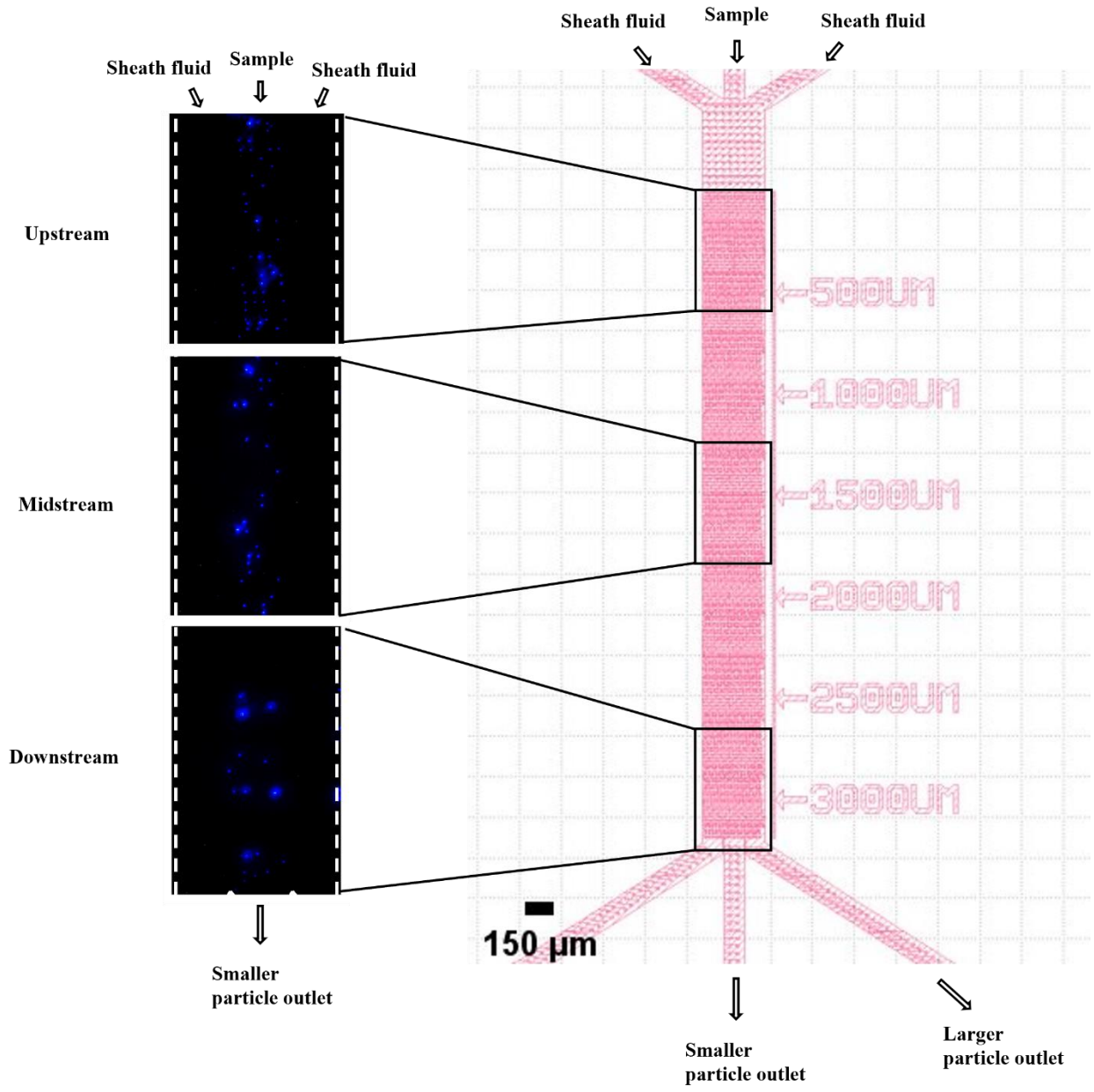

Figure 61. Blue fluorescently labeled particles (mean diameter, 0.989µm) flowed from upstream to downstream. Particle suspension infused middle inlet assisted by two sheath fluids. The critical diameter (D_c) of the design of the device is 3µm (chip B). The channel width is 0.3mm and channel height is 0.01mm.

Figure 62 demonstrates particle separation in the DLD structure from microscope images of a collection of the outlets of smaller and bigger particles. Smaller particles (mean diameter, 2.6µm) were collected in the middle (smaller particle) outlet in Figure 62a, and larger particles

(mean diameter, 4.1µm) were collected in the side (larger particle) outlet in Figure 62b. Since the design's critical diameter (D_c) was 3µm, smaller particles than D_c were collected in the middle outlet, and larger particles than D_c were collected in the side outlet.

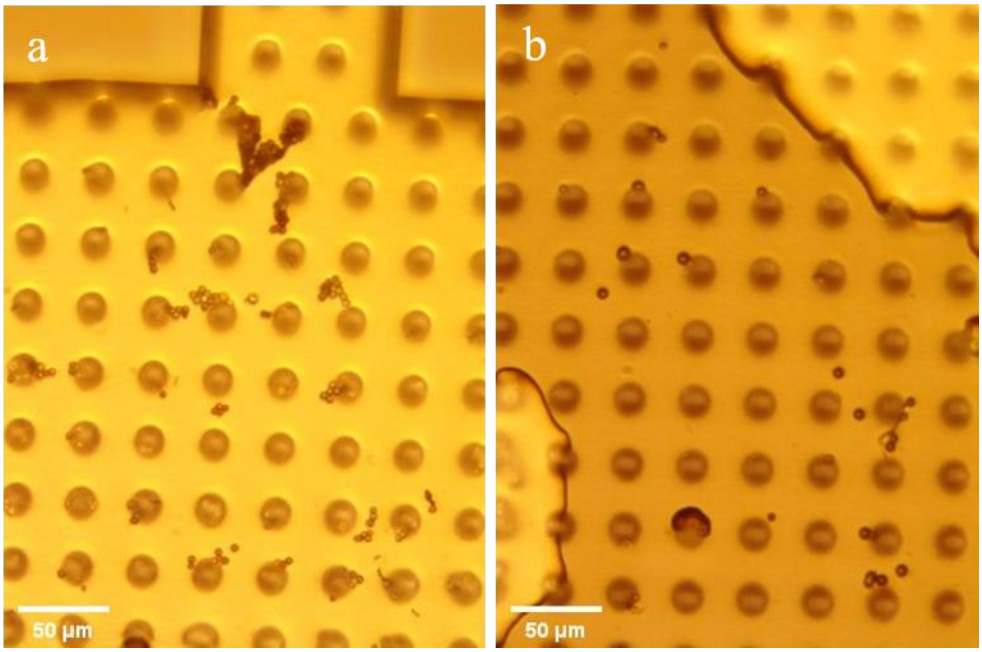

Figure 62. Proof of particle separation. The post diameter is12.5µm. (a) Smaller particles (mean diameter, 2.6µm) than Dc (3µm) in the middle outlet. (b) Larger particles (mean diameter, 4.1µm) than Dc (3µm) in the side outlet.

Summary and Future Work

We successfully fabricated microfluidic devices and intermediately inspected them in the microfabrication process. We performed experiments to study laminar flow with the PDMS bonded microfluidic silicon chip, and then polystyrene particles were infused using syringe pumps. We separated particles with DLD in a microfluidic channel by providing microscope images of different sizes of particles collected at different outlets. However, there was an observational limit of the trajectory of particles that flowed separately in the DLD: particles smaller than D_c flowed straight and particles larger than D_c flowed diagonally. This movement is

likely due to too-fast fluid velocity in the DLD; we theoretically calculated the fluid velocity as approximately 4000 – 5000 μm/s.

There are three possible approaches to observe separate particle trajectories in the DLD. First, the infusion flow rate should be lower using a syringe pump control or low syringe volume. Flow rate from the syringe pump is related to syringe volume. Second, a high-speed camera could help record particle trajectory in the DLD, but the camera is not easily accessible. Finally, the width of the DLD and depth of microfluidic silicon etching should be wider and deeper, respectively. That would make it possible to increase the cross-sectional area of the channel, which helps to lower the fluid velocity in the DLD with the syringe pump available to us.

Once completing particle separation using the DLD with polystyrene particles, separating biological particles would not be difficult, including cells, exosomes, DNA, and more. This technique will be very promising by incorporating within a lab on a chip to be used for many purposes, including early detection of disease through portable diagnostic devices.

CHAPTER 5. OVERALL CONCLUSION

In this dissertation, we have discussed three particle isolation and separation methods, which allows simple and effective control and manipulation of a wide range of particles and biopolymers in a fluid environment without any issue associated with conventional techniques. Our extensive experimental results, theoretical models, and preliminary data presented here offer other researchers and engineers to tune operating parameters to successfully perform particle separation experiments, as well as determine design parameters to fabricate microscale and nanoscale devices.

REFERENCES

[1] J. Voldman, “Electrical Forces for Microscale Cell Manipulation,” *Annual Review of Biomedical Engineering*, vol. 8, no. 1, pp. 425–454, 2006, doi: 10.1146/annurev.bioeng.8.061505.095739.

[2] G. Zheng, F. Patolsky, Y. Cui, W. U. Wang, and C. M. Lieber, “Multiplexed electrical detection of cancer markers with nanowire sensor arrays,” *Nature Biotechnology*, vol. 23, no. 10, pp. 1294–1301, 2005, doi: 10.1038/nbt1138.

[3] C. Joo, H. Balci, Y. Ishitsuka, C. Buranachai, and T. Ha, “Advances in single-molecule fluorescence methods for molecular biology,” *Annual Review of Biochemistry*, vol. 77, pp. 51–76, 2008, doi: 10.1146/annurev.biochem.77.070606.101543.

[4] M. Singh-Zocchi, S. Dixit, V. Ivanov, and G. Zocchi, “Single-molecule detection of DNA hybridization,” *Proceedings of the National Academy of Sciences of the United States of America*, vol. 100, no. 13, pp. 7605–7610, 2003, doi: 10.1073/pnas.1337215100.

[5] F. F. Becker, X. B. Wang, Y. Huang, R. Pethig, J. Vykoukal, and P. R. C. Gascoyne, “Separation of human breast cancer cells from blood by differential dielectric affinity,” *Proceedings of the National Academy of Sciences of the United States of America*, vol. 92, no. 3, pp. 860–864, 1995, doi: 10.1073/pnas.92.3.860.

[6] L. Zheng, J. P. Brody, and P. J. Burke, “Electronic manipulation of DNA, proteins, and nanoparticles for potential circuit assembly,” *Biosensors and Bioelectronics*, vol. 20, no. 3, pp. 606–619, 2004, doi: 10.1016/j.bios.2004.03.029.

[7] H. Shafiee, J. L. Caldwell, M. B. Sano, and R. V. Davalos, “Contactless dielectrophoresis: A new technique for cell manipulation,” *Biomedical Microdevices*, vol. 11, no. 5, pp. 997–1006, 2009, doi: 10.1007/s10544-009-9317-5.

[8] T. B. Jones, *Eletromechanics of Particles*. 1995.

[9] H. A. Pohl, *Dielectrophoresis: The Behavior of Neutral Matter in Nonuniform Electric Fields (Cambridge Monographs on Physics)*. 1978.

[10] K. J. Freedman, L. M. Otto, A. P. Ivanov, A. Barik, S. H. Oh, and J. B. Edel, “Nanopore sensing at ultra-low concentrations using single-molecule dielectrophoretic trapping,” *Nature Communications*, vol. 7, pp. 1–9, 2016, doi: 10.1038/ncomms10217.

[11] A. Barik *et al.*, “Graphene-edge dielectrophoretic tweezers for trapping of biomolecules,” *Nature Communications*, vol. 8, no. 1, p. 1867, 2017, doi: 10.1038/s41467-017-01635-9.

[12] K. Khoshmanesh *et al.*, “On-chip separation of Lactobacillus bacteria from yeasts using dielectrophoresis,” *Microfluidics and Nanofluidics*, vol. 12, no. 1–4, pp. 597–606, 2012, doi: 10.1007/s10404-011-0900-8.

[13] G. H. Markx, P. A. Dyda, and R. Pethig, “Dielectrophoretic separation of bacteria using a conductivity gradient,” *Journal of Biotechnology*, vol. 51, no. 2, pp. 175–180, 1996, doi: 10.1016/0168-1656(96)01617-3.

[14] C.-F. Chou *et al.*, “Electrodeless Dielectrophoresis of Single- and Double-Stranded DNA,” *Biophysical Journal*, vol. 83, no. 4, pp. 2170–2179, 2002, doi: 10.1016/S0006-3495(02)73977-5.

[15] S. Bhattacharya, T. C. Chao, and A. Ros, “Insulator-based dielectrophoretic single particle and single cancer cell trapping,” *Electrophoresis*, vol. 32, no. 18, pp. 2550–2558, 2011, doi: 10.1002/elps.201100066.

[16] P. V. Jones, G. L. Salmon, and A. Ros, “Continuous Separation of DNA Molecules by Size Using Insulator-Based Dielectrophoresis,” *Analytical Chemistry*, vol. 89, no. 3, pp. 1531–1539, 2017, doi: 10.1021/acs.analchem.6b03369.

[17] D. R. Gossett *et al.*, “Label-free cell separation and sorting in microfluidic systems,” *Analytical and Bioanalytical Chemistry*, vol. 397, no. 8, pp. 3249–3267, 2010, doi: 10.1007/s00216-010-3721-9.

[18] B. Essevaz-Roulet, U. Bockelmann, and F. Heslot, “Mechanical separation of the complementary strands of DNA,” *Proceedings of the National Academy of Sciences of the United States of America*, vol. 94, no. 22, pp. 11935–11940, 1997, doi: 10.1073/pnas.94.22.11935.

[19] T. T. Perkins, R. V. Dalal, P. G. Mitsis, and S. M. Block, “Sequence-dependent pausing of single lambda exonuclease molecules,” *Science*, vol. 301, no. 5641, pp. 1914–1918, 2003, doi: 10.1126/science.1088047.

[20] K. C. Neuman, T. Lionnet, and J. F. Allemand, “Single-molecule micromanipulation techniques,” *Annual Review of Materials Research*, vol. 37, pp. 33–67, 2007, doi: 10.1146/annurev.matsci.37.052506.084336.

[21] F. Ritort, “Single-molecule experiments in biological physics: Methods and applications,” *Journal of Physics Condensed Matter*, vol. 18, no. 32, 2006, doi: 10.1088/0953-8984/18/32/R01.

[22] K. C. Neuman and A. Nagy, “Single-molecule force spectroscopy: optical tweezers, magnetic tweezers and atomic force microscopy,” *Nature methods*, vol. 5, no. 6, pp. 491–505, 2008, doi: 10.1038/nmeth.1218.Single-molecule.

[23] K. A. Brown, J. A. Aguilar, and R. M. Westervelt, “Coaxial atomic force microscope tweezers,” *Applied Physics Letters*, vol. 96, no. 12, pp. 1–4, 2010, doi: 10.1063/1.3372621.

[24] K. A. Brown and R. M. Westervelt, “Triaxial AFM probes for noncontact trapping and manipulation,” *Nano Letters*, vol. 11, no. 8, pp. 3197–3201, 2011, doi: 10.1021/nl201434t.

[25] Y. Tao and H. Kumar Wickramasinghe, “Coaxial atomic force microscope probes for dielectrophoresis of DNA under different buffer conditions,” *Applied Physics Letters*, vol. 110, no. 7, pp. 1–6, 2017, doi: 10.1063/1.4974939.

[26] P. Zhou *et al.*, “Spatial Manipulation and Assembly of Nanoparticles by Atomic Force Microscopy Tip-Induced Dielectrophoresis,” *ACS Applied Materials and Interfaces*, vol. 9, no. 19, pp. 16715–16724, 2017, doi: 10.1021/acsami.7b03565.

[27] R. W. Clarke, S. S. White, D. Zhou, L. Ying, and D. Klenerman, “Trapping of proteins under physiological conditions in a nanopipette,” *Angewandte Chemie - International Edition*, vol. 44, no. 24, pp. 3747–3750, 2005, doi: 10.1002/anie.200500196.

[28] L. Ying, S. S. White, A. Bruckbauer, L. Meadows, Y. E. Korchev, and D. Klenerman, “Frequency and Voltage Dependence of the Dielectrophoretic Trapping of Short Lengths of DNA and dCTP in a Nanopipette,” *Biophysical Journal*, vol. 86, no. 2, pp. 1018–1027, 2004, doi: 10.1016/S0006-3495(04)74177-6.

[29] V. Namasivayam, R. G. Larson, D. T. Burke, and M. A. Burns, “Electrostretching DNA molecules using polymer-enhanced media within microfabricated devices,” *Analytical Chemistry*, vol. 74, no. 14, pp. 3378–3385, 2002, doi: 10.1021/ac025551h.

[30] B. Kundukad, J. Yan, and P. S. Doyle, “Effect of YOYO-1 on the mechanical properties of DNA,” *Soft Matter*, vol. 10, no. 48, pp. 9721–9728, 2014, doi: 10.1039/C4SM02025A.

[31] D. J. Bakewell, N. Vergara-Irigaray, and D. Holmes, “Dielectrophoresis of Biomolecules,” *JSM Nanotechnol Nanomed*, vol. 1, no. 1, pp. 1–14, 2013.

[32] D. J. Bakewell, I. Ermolina, H. Morgan, J. Milner, and Y. Feldman, “Dielectric relaxation measurements of 12 kbp plasmid DNA,” *Biochimica et Biophysica Acta - Gene Structure and Expression*, vol. 1493, no. 1–2, pp. 151–158, 2000, doi: 10.1016/S0167-4781(00)00176-7.

[33] S. Bone and C. A. Small, “Dielectric studies of ion fluctuation and chain bending in native DNA,” *BBA - Gene Structure and Expression*, vol. 1260, no. 1, pp. 85–93, 1995, doi: 10.1016/0167-4781(94)00181-2.

[34] I. Teraoka, *Polymer Solutions: An Introduction to Physical Properties*. 2002.

[35] F. M. White, *Fluid Mechanics*. 2011.

[36] C. Collinson and T. Roper, *Particle Mechanics*. 1995.

[37] A. Ramos, H. Morgan, N. G. Green, and A. Castellanos, “Ac electrokinetics: a review of forces in microelectrode structures,” *Journal of Physics D: Applied Physics*, vol. 31, pp. 2338–2353, 1998.

[38] J. Froberg, V. Jayasooriya, S. You, D. Nawarathna, and Y. Choi, “Quantitative measurements of dielectrophoresis in a nanoscale electrode array with an atomic force microscopy,” *Applied Physics Letters*, vol. 110, no. 20, 2017, doi: 10.1063/1.4983785.

[39] M. Hywel, I. Alberto García, B. David, G. G. Nicolas, and R. Antonio, “The dielectrophoretic and travelling wave forces generated by interdigitated electrode arrays: analytical solution using Fourier series,” *Journal of Physics D: Applied Physics*, vol. 34, no. 10, p. 1553, 2001.

[40] V. Jayasooriya and D. Nawarathna, “Design of Micro-interdigitated Electrodes and Detailed Impedance Data Analysis for Label-free Biomarker Quantification,” *Electroanalysis*, vol. 29, no. 2, pp. 330–338, 2017, doi: 10.1002/elan.201600364.

[41] L. Velmanickam, D. Laudenbach, and D. Nawarathna, “Dielectrophoretic label-free immunoassay for rare-analyte quantification in biological samples,” *Physical Review E*, vol. 94, no. 4, pp. 1–6, 2016, doi: 10.1103/PhysRevE.94.042408.

[42] J. Regtmeier, T. D. Thanh, R. Eichhorn, D. Anselmetti, and A. Ros, “Dielectrophoretic manipulation of DNA: Separation and polarizability,” *Analytical Chemistry*, vol. 79, no. 10, pp. 3925–3932, 2007, doi: 10.1021/ac062431r.

[43] D. J. Bakewell and H. Morgan, “Dielectrophoresis of DNA: Time- And frequency-dependent collections on microelectrodes,” *IEEE Transactions on Nanobioscience*, vol. 5, no. 1, pp. 1–8, 2006, doi: 10.1109/TNB.2005.864012.

[44] J. Regtmeier, R. Eichhorn, L. Bogunovic, A. Ros, and D. Anselmetti, “Dielectrophoretic trapping and polarizability of DNA: The role of spatial conformation,” *Analytical Chemistry*, vol. 82, no. 17, pp. 7141–7149, 2010, doi: 10.1021/ac1005475.

[45] S. Tuukkanen *et al.*, “Carbon nanotubes as electrodes for dielectrophoresis of DNA,” *Nano Letters*, vol. 6, no. 7, pp. 1339–1343, 2006, doi: 10.1021/nl060771m.

[46] K. E. Sung and M. A. Burns, “Optimization of dielectrophoretic DNA stretching in microfabricated devices,” *Analytical Chemistry*, vol. 78, no. 9, pp. 2939–2947, 2006, doi: 10.1021/ac051662f.

[47] C. H. Chiou, L. J. Chien, and J. N. Kuo, “Nanoconstriction-based electrodeless dielectrophoresis chip for nanoparticle and protein preconcentration,” *Applied Physics Express*, vol. 8, no. 8, 2015, doi: 10.7567/APEX.8.085201.

[48] N. G. Green and T. B. Jones, “Numerical determination of the effective moments of non-spherical particles,” *Journal of Physics D: Applied Physics*, vol. 40, no. 1, pp. 78–85, 2007, doi: 10.1088/0022-3727/40/1/S12.

[49] L. Gan, F. Camacho-Alanis, and A. Ros, “Polarizability of Six-Helix Bundle and Triangle DNA Origami and Their Escape Characteristics from a Dielectrophoretic Trap,” *Analytical Chemistry*, vol. 87, no. 24, pp. 12059–12064, 2015, doi: 10.1021/acs.analchem.5b02524.

[50] S. Tuukkanen *et al.*, “Trapping of 27 bp-8 kbp DNA and immobilization of thiol-modified DNA using dielectrophoresis,” *Nanotechnology*, vol. 18, no. 29, 2007, doi: 10.1088/0957-4484/18/29/295204.

[51] R. Martinez-Duarte, F. Camacho-Alanis, P. Renaud, and A. Ros, “Dielectrophoresis of lambda-DNA using 3D carbon electrodes,” *Electrophoresis*, vol. 34, no. 7, pp. 1113–1122, 2013, doi: 10.1002/elps.201200447.

[52] P. Yager *et al.*, “Microfluidic diagnostic technologies for global public health,” *Nature*, vol. 442, no. 7101, pp. 412–418, 2006, doi: 10.1038/nature05064.

[53] O. Caen *et al.*, “High-throughput multiplexed fluorescence-activated droplet sorting,” *Microsystems and Nanoengineering*, vol. 4, no. 1, 2018, doi: 10.1038/s41378-018-0033-2.

[54] D. Migliozzi, B. Pelz, D. G. Dupouy, A. L. Leblond, A. Soltermann, and M. A. M. Gijs, “Microfluidics-assisted multiplexed biomarker detection for in situ mapping of immune cells in tumor sections,” *Microsystems and Nanoengineering*, vol. 5, no. 1, 2019, doi: 10.1038/s41378-019-0104-z.

[55] M. Sesen, T. Alan, and A. Neild, “Droplet Control Technologies for Microfluidic High Throughput Screening (μHTS),” *Lab on a chip*, pp. 2372–2394, 2017, doi: 10.1039/b000000x.

[56] N. Tottori and T. Nisisako, “Degas-Driven Deterministic Lateral Displacement in Poly(dimethylsiloxane) Microfluidic Devices,” *Analytical Chemistry*, vol. 91, no. 4, pp. 3093–3100, 2019, doi: 10.1021/acs.analchem.8b05587.

[57] E. Yeh, C. Fu, L. Hu, R. Thakur, J. Feng, and L. P. Lee, “Self-powered integrated microfluidic point-of-care low-cost enabling (SIMPLE) chip,” *Science Advances*, pp. 1–12, 2017.

[58] A. Chronopoulos, T. J. Lieberthal, and A. E. del R. Hernandez, “Exosomes as a liquid biopsy for Pancreatic cancer,” *Convergent Science Physical Oncology*, 2017, doi: 10.1016/j.lungcan.2017.12.012.

[59] S. S. Jeffrey and M. Toner, “Liquid biopsy: a perspective for probing blood for cancer,” *Lab on a Chip*, vol. 19, no. 4, pp. 548–549, 2019, doi: 10.1039/C8LC90117A.

[60] R. Vaidyanathan, R. H. Soon, P. Zhang, K. Jiang, and C. T. Lim, “Cancer diagnosis: from tumor to liquid biopsy and beyond,” *Lab on a Chip*, vol. 19, no. 1, pp. 11–34, 2019, doi: 10.1039/c8lc00684a.

[61] A. Lenshof *et al.*, “Acoustic whole blood plasmapheresis chip for PSA microarray diagnostics,” *Proceedings of Conference, MicroTAS 2009 - The 13th International Conference on Miniaturized Systems for Chemistry and Life Sciences*, vol. 81, no. 15, pp. 1330–1332, 2009, doi: 10.1021/pr8007545.(27).

[62] H. Jiang, X. Weng, C. H. Chon, X. Wu, and D. Li, "A microfluidic chip for blood plasma separation using electro-osmotic flow control," *Journal of Micromechanics and Microengineering*, vol. 21, no. 8, 2011, doi: 10.1088/0960-1317/21/8/085019.

[63] C. W. Yung, J. Fiering, A. J. Mueller, and D. E. Ingber, "Micromagnetic-microfluidic blood cleansing device," *Lab on a Chip*, vol. 9, no. 9, pp. 1171–1177, 2009, doi: 10.1039/b816986a.

[64] S. Yan, J. Zhang, D. Yuan, and W. Li, "Hybrid microfluidics combined with active and passive approaches for continuous cell separation," *Electrophoresis*, vol. 38, no. 2, pp. 238–249, 2017, doi: 10.1002/elps.201600386.

[65] C. Li, C. Liu, Z. Xu, and J. Li, "Extraction of plasma from whole blood using a deposited microbead plug (DMBP) in a capillary-driven microfluidic device," *Biomedical Microdevices*, vol. 14, no. 3, pp. 565–572, 2012, doi: 10.1007/s10544-012-9635-x.

[66] C. Liu *et al.*, "Membrane-based, sedimentation-assisted plasma separator for point-of-care applications," *Analytical Chemistry*, vol. 85, no. 21, pp. 10463–10470, 2013, doi: 10.1021/ac402459h.

[67] S. Choi, S. Song, C. Choi, and J. K. Park, "Continuous blood cell separation by hydrophoretic filtration," *Lab on a Chip*, vol. 7, no. 11, pp. 1532–1538, 2007, doi: 10.1039/b705203k.

[68] M. Yamada, M. Nakashima, and M. Seki, "Pinched flow fractionation: Continuous size separation of particles utilizing a laminar flow profile in a pinched microchannel," *Analytical Chemistry*, vol. 76, no. 18, pp. 5465–5471, 2004, doi: 10.1021/ac049863r.

[69] M. Kersaudy-Kerhoas and E. Sollier, "Micro-scale blood plasma separation: From acoustophoresis to egg-beaters," *Lab on a Chip*, vol. 13, no. 17, pp. 3323–3346, 2013, doi: 10.1039/c3lc50432h.

[70] I. K. Dimov, L. Basabe-Desmonts, J. L. Garcia-Cordero, B. M. Ross, A. J. Ricco, and L. P. Lee, "Stand-alone self-powered integrated microfluidic blood analysis system (SIMBAS)," *Lab on a Chip*, vol. 11, no. 5, pp. 845–850, 2011, doi: 10.1039/c0lc00403k.

[71] D. Forchelet *et al.*, "Separation of blood microsamples by exploiting sedimentation at the microscale," *Scientific Reports*, vol. 8, no. 1, pp. 1–9, 2018, doi: 10.1038/s41598-018-32314-4.

[72] M. Sun, Z. S. Khan, and S. A. Vanapalli, "Blood plasma separation in a long two-phase plug flowing through disposable tubing," *Lab on a Chip*, vol. 12, no. 24, pp. 5225–5230, 2012, doi: 10.1039/c2lc40544j.

[73] Y. Xia and G. M. Whitesides, "Soft Lithography," *Annual Review of Materials Science*, vol. 28, no. 1, pp. 153–184, 1998, doi: 10.1146/annurev.matsci.28.1.153.

[74] D. Qin, Y. Xia, and G. M. Whitesides, “Soft lithography for micro- and nanoscale patterning,” *Nature Protocols*, vol. 5, no. 3, pp. 491–502, 2010, doi: 10.1038/nprot.2009.234.

[75] K. Hosokawa, K. Sato, and M. Maeda, “Power-free poly (dimethylsiloxane) microfluidic devices for gold nanoparticle-based DNA analysis,” *Lab on a Chip*, vol. 4, pp. 181–185, 2004, doi: 10.1039/B403930K.

[76] A. Lamberti, S. L. Marasso, and M. Cocuzza, “PDMS membranes with tunable gas permeability for microfluidic applications,” *RSC Advances*, vol. 4, no. 106, pp. 61415–61419, 2014, doi: 10.1039/c4ra12934b.

[77] M. A. Eddings and B. K. Gale, “A PDMS-based gas permeation pump for on-chip fluid handling in microfluidic devices,” *Journal of Micromechanics and Microengineering*, vol. 16, no. 11, pp. 2396–2402, 2006, doi: 10.1088/0960-1317/16/11/021.

[78] J. H. Son *et al.*, “Hemolysis-free blood plasma separation,” *Lab on a Chip*, vol. 14, no. 13, pp. 2287–2292, 2014, doi: 10.1039/c4lc00149d.

[79] K. ichiro Kamei *et al.*, “3D printing of soft lithography mold for rapid production of polydimethylsiloxane-based microfluidic devices for cell stimulation with concentration gradients,” *Biomedical Microdevices*, vol. 17, no. 2, 2015, doi: 10.1007/s10544-015-9928-y.

[80] M. A. Eddings, M. A. Johnson, and B. K. Gale, “Determining the optimal PDMS-PDMS bonding technique for microfluidic devices,” *Journal of Micromechanics and Microengineering*, vol. 18, no. 6, Jun. 2008, doi: 10.1088/0960-1317/18/6/067001.

[81] K. K. Lee and C. H. Ahn, “A new on-chip whole blood/plasma separator driven by asymmetric capillary forces,” *Lab on a Chip*, vol. 13, no. 16, pp. 3261–3267, 2013, doi: 10.1039/c3lc50370d.

[82] M. S. Maria, P. E. Rakesh, T. S. Chandra, and A. K. Sen, “Capillary flow-driven microfluidic device with wettability gradient and sedimentation effects for blood plasma separation,” *Scientific Reports*, vol. 7, no. January, pp. 1–12, 2017, doi: 10.1038/srep43457.

[83] T. Trantidou, Y. Elani, E. Parsons, and O. Ces, “Hydrophilic surface modification of pdms for droplet microfluidics using a simple, quick, and robust method via pva deposition,” *Microsystems and Nanoengineering*, vol. 3, no. April 2016, 2017, doi: 10.1038/micronano.2016.91.

[84] G. M. Whitesides, “The origins and the future of microfluidics,” *Nature*, vol. 442, no. 7101, pp. 368–373, 2006, doi: 10.1038/nature05058.

[85] A. E. Özçam, K. Efimenko, and J. Genzer, "Effect of ultraviolet/ozone treatment on the surface and bulk properties of poly(dimethyl siloxane) and poly(vinylmethyl siloxane) networks," *Polymer (United Kingdom)*, vol. 55, no. 14, pp. 3107–3119, 2014, doi: 10.1016/j.polymer.2014.05.027.

[86] H. Chen, A. A. Mcclelland, Z. Chen, and J. Lahann, "Solventless Adhesive Bonding Using Reactive Polymer Coatings," *Analytical Chemistry*, vol. 80, no. 11, pp. 4119–4124, 2008.

[87] A. R. Abate, D. Lee, T. Do, C. Holtze, and D. A. Weitz, "Glass coating for PDMS microfluidic channels by sol – gel methods †," *Lab on a Chip*, vol. 8, pp. 516–518, 2008, doi: 10.1039/b800001h.

[88] W. C. Bauer, M. Fischlechner, and W. T. S. Huck, "Hydrophilic PDMS microchannels for high-throughput formation of oil-in-water microdroplets and water-in-oil-in-water double emulsions," *Lab on a chip*, vol. 10, pp. 1814–1819, 2010, doi: 10.1039/c004046k.

[89] K. Hosokawa, M. Omata, and M. Maeda, "Immunoassay on a power-free microchip with laminar flow-assisted dendritic amplification," *Analytical Chemistry*, vol. 79, no. 15, pp. 6000–6004, 2007, doi: 10.1021/ac070659o.

[90] K. Hosokawa, M. Omata, K. Sato, and M. Maeda, "Power-free sequential injection for microchip immunoassay toward point-of-care testing," *Lab on a Chip*, vol. 6, no. 2, pp. 236–241, 2006, doi: 10.1039/b513424b.

[91] K. Hosokawa, K. Sato, N. Ichikawa, and M. Maeda, "Power-free poly(dimethylsiloxane) microfluidic devices for gold nanoparticle-based DNA analysis," *Lab on a Chip*, vol. 4, no. 3, pp. 181–185, 2004, doi: 10.1039/b403930k.

[92] G. Comina, A. Suska, and D. Filippini, "PDMS lab-on-a-chip fabrication using 3D printed templates," *Lab on a Chip*, vol. 14, no. 2, pp. 424–430, 2014, doi: 10.1039/c3lc50956g.

[93] R. K. Pathria and P. Beale, *Statistical Mechanics*, Third edit. 2011.

[94] A. J. Mäki, M. Peltokangas, J. Kreutzer, S. Auvinen, and P. Kallio, "Modeling carbon dioxide transport in PDMS-based microfluidic cell culture devices," *Chemical Engineering Science*, vol. 137, pp. 515–524, 2015, doi: 10.1016/j.ces.2015.06.065.

[95] D. Huh *et al.*, "Gravity-driven microfluidic particle sorting device with hydrodynamic separation amplification," *Analytical Chemistry*, vol. 79, no. 4, pp. 1369–1376, 2007, doi: 10.1021/ac061542n.

[96] T. A. Shatova, S. Lathwal, M. R. Engle, H. D. Sikes, and K. F. Jensen, "Portable, Constriction-Expansion Blood Plasma Separation and Polymerization-Based Malaria Detection," *Analytical Chemistry*, vol. 88, no. 15, pp. 7627–7632, 2016, doi: 10.1021/acs.analchem.6b01355.

[97] X. B. Zhang *et al.*, “Gravitational sedimentation induced blood delamination for continuous plasma separation on a microfluidics chip,” *Analytical Chemistry*, vol. 84, no. 8, pp. 3780–3786, 2012, doi: 10.1021/ac3003616.

[98] G. M. Whitesides, “The origins and the future of microfluidics,” *Nature*, vol. 442, no. 7101, pp. 368–373, 2006, doi: 10.1016/j.agee.2012.07.026.

[99] X. Ding *et al.*, “Cell separation using tilted-angle standing surface acoustic waves,” *Proceedings of the National Academy of Sciences*, vol. 111, no. 36, pp. 12992–12997, 2014, doi: 10.1073/pnas.1413325111.

[100] M. Wu *et al.*, “High-throughput cell focusing and separation: Via acoustofluidic tweezers,” *Lab on a Chip*, vol. 18, no. 19, pp. 3003–3010, 2018, doi: 10.1039/c8lc00434j.

[101] P. J. A. Kenis, R. F. Ismagilov, and G. M. Whitesides, “Microfabrication inside capillaries using multiphase laminar flow patterning,” *Science*, vol. 285, no. 5424, pp. 83–85, 1999, doi: 10.1126/science.285.5424.83.

[102] B. Kirby, *Micro- and Nanoscale Fluid Mechanics*. Cambridge University Press, 2010. doi: https://doi.org/10.1017/CBO9780511760723.

[103] L. R. Huang, E. C. Cox, R. H. Austin, and J. C. Sturm, “Continuous Particle Separation Through Deterministic Lateral Displacement,” *Science*, vol. 304, no. 5673, pp. 987–990, 2004, doi: 10.1126/science.1094567.

[104] Y. Chen *et al.*, “Concentrating genomic length DNA in a microfabricated array,” *Physical Review Letters*, vol. 114, no. 19, pp. 1–5, 2015, doi: 10.1103/PhysRevLett.114.198303.

[105] J. T. Smith *et al.*, “Integrated nanoscale deterministic lateral displacement arrays for separation of extracellular vesicles from clinically-relevant volumes of biological samples,” *Lab on a Chip*, vol. 18, no. 24, pp. 3913–3925, 2018, doi: 10.1039/c8lc01017j.

[106] K. K. Zeming, T. Salafi, C. H. Chen, and Y. Zhang, “Asymmetrical Deterministic Lateral Displacement Gaps for Dual Functions of Enhanced Separation and Throughput of Red Blood Cells,” *Scientific Reports*, vol. 6, no. November 2015, pp. 1–10, 2016, doi: 10.1038/srep22934.

[107] M. G. Ahmed *et al.*, “Isolation, Detection, and Antigen-Based Profiling of Circulating Tumor Cells Using a Size-Dictated Immunocapture Chip,” *Angewandte Chemie - International Edition*, vol. 56, no. 36, pp. 10681–10685, 2017, doi: 10.1002/anie.201702675.

[108] K. Loutherback, J. D’Silva, L. Liu, A. Wu, R. H. Austin, and J. C. Sturm, “Deterministic separation of cancer cells from blood at 10 mL/min,” *AIP Advances*, vol. 2, no. 4, 2012, doi: 10.1063/1.4758131.

[109] L. R. Huang, E. C. Cox, R. H. Austin, and J. C. Sturm, “Continuous Particle Separation Through Deterministic Lateral Displacement,” *Science*, vol. 304, no. 5673, pp. 987–990, 2004, doi: 10.1126/science.1094567.

[110] D. Inglis, “Microfluidic Devices for Cell Separation,” 2007.

[111] J. A. Davis, “Microfluidic Separation of Blood Components through Deterministic Lateral Displacement,” 2008.